THEORY AND SIMULATION OF OSCILLATIONS ON NEAR-STEADY STATE IN CROSSED-FIELD ELECTRON FLOW AND THE RESULTING TRANSPORT

by

Keith Lewis Cartwright

Memorandum No. UCB/ERL M99/68

17 December 1999

THEORY AND SIMULATION OF OSCILLATIONS ON NEAR-STEADY STATE IN CROSSED-FIELD ELECTRON FLOW AND THE RESULTING TRANSPORT

by

Keith Lewis Cartwright

Memorandum No. UCB/ERL M99/68

17 December 1999

ELECTRONICS RESEARCH LABORATORY

College of Engineering
University of California, Berkeley
94720

Theory and Simulation of Oscillations on Near-Steady State in Crossed-Field Electron Flow and the Resulting Transport

by

Keith Lewis Cartwright

B.S. (University of Illinois) 1991
M.A. (University of California, Berkeley) 1999

A dissertation submitted in partial satisfaction of the

requirements for the degree of

Doctor of Philosophy

in

Physics

in the

GRADUATE DIVISION

of the

UNIVERSITY of CALIFORNIA at BERKELEY

Committee in charge:

Professor Charles K. Birdsall, Co-Chair
Professor Joel Fajans, Co-Chair
Professor Jonathan S. Wurtele
Professor Michael A. Lieberman

Fall, 1999

The dissertation of Keith Lewis Cartwright is approved:

Charles K. Birdsall, Co-Chair — Date

Joel Fajans, Co-Chair — Date

Jonathan S. Wurtele — Date

Michael A. Lieberman — Date

University of California at Berkeley

Fall, 1999

Theory and Simulation of Oscillations on Near-Steady State in Crossed-Field Electron Flow and the Resulting Transport

by

Keith Lewis Cartwright

Abstract

Theory and Simulation of Oscillations on Near-Steady State in Crossed-Field Electron Flow and the Resulting Transport

by

Keith Lewis Cartwright

Doctor of Philosophy in Physics

University of California at Berkeley

Professor Charles K. Birdsall, Co-Chair

Professor Joel Fajans, Co-Chair

The purpose of this study is to understand the oscillatory steady-state behavior of crossed-field electron flow in diodes for magnetic fields greater than the Hull field ($B > B_H$) by the means of theory and self-consistent, electrostatic particle-in-cell (PIC) simulations. Many prior analytic studies of diode-like problems have been time-independent, which leaves the stability and time-dependence of these models unresolved. We investigate fluctuations through the system, including virtual cathode oscillations, and compare results for various cathode injection models. The dominant oscillations in magnetically insulated crossed-field diodes are found to be a series resonance, $Z(\omega_s) = 0$, between the pure electron plasma and vacuum impedance of the diode. The series resonance in crossed-field electron flow is shown to be the $k_y \to 0$ (one-dimensional) limit of the diocotron/magnetron eigenmode equation. The wavenumber, k_y, is perpendicular to the direction across the diode and magnetic field. The series resonance is derived theoretically and verified with self-consistent, electrostatic, PIC simulations.

Electron transport across the magnetic field in a cutoff planar smooth-bore magnetron is described on the basis of surface waves (formed by the shear flow instability) perpendicular to the magnetic field and along the cathode. A self-consistent, 2d3v

(two spatial dimensions and three velocity components), electrostatic PIC simulation of a crossed-field diode produces a near-Brillouin flow which slowly expands across the diode, punctuated by sudden transport across the diode. The theory of slow transport across the diode is explained by the addition of perturbed orbits to the Brillouin shear flow motion of the plasma in the diode. A slow drift compared to the shear flow is described which results from the fields caused by the surface wave inducing an electrostatic ponderomotive-like force in a dc external magnetic field.

In order to perform the above-mentioned simulation, a second-order injection algorithm was devised. It is shown that time-centering of the position and velocity is necessary in order to maintain second-order accuracy. The initial push is shown to be important in calculating the correct electric field at the boundary where particles are injected, in relaxing constraints on the time step, and in providing reliable field fluctuations from finite particle statistics.

Kinetic simulation of plasmas in which equilibrium occurs over ion timescales poses a computational challenge due to disparity with electron timescales. Hybrid electrostatic PIC algorithms are presented in which most of the electrons reach thermodynamic equilibrium (Maxwell-Boltzmann (MB) distribution function) each time step. Conservation of charge enables convergence of the nonlinear Poisson equation. Energy conservation is used to determine the temperature of the Boltzmann species. Full PIC and the PIC-MB hybrid simulations compare well for photo-ionized sustained discharges and current-driven

DC discharges.

Professor Charles K. Birdsall, Co-Chairs Date

Professor Joel Fajans, Co-Chairs Date

To Mom and Dad.

Contents

List of Figures

List of Tables

Acknowledgments

There are many people I wish thank for helping me complete my thesis. I'm sure I have missed some, so my deepest apologies and sincerest gratitude.

I would like to thank my family for their many years of support. Without them this work would not exist.

I would thank my advisor, Professor C. K. (Ned) Birdsall for giving me the opportunity to work with him and his Plasma Theory and Simulation Group. I would like to thank him for his many stimulating discussions. His enthusiasm and knowledge of computer computer simulation has been inspiring. As well as guiding me in my thesis research, he has played a large role in my professional growth and development.

I would also like to thank the readers of my thesis, Professor Joel Fajans, Professor Jonathan S. Wurtele, and Professor Michael A. Lieberman, for their reading of this document and their comments and corrections. I really appreciate their effort, given how busy they are and the short time I allowed for them to read it.

There are many member of PTSG (Plasma Theory and Simulation Group) that have helped me over the years both with technical advise and relaxation (biking, hiking, poker playing, Babylon 5 watching, etc.). These are Emi Kawamura, Peggy Christenson, Morgan Oslake, Venkatesh (PG) Gopinath, Dave Cooperberg, Kevin Bowers, Weiguang Qiu, and Helen Smith. I give special thanks to John Verboncoeur who waded though many drafts and being a 'fifth' reader of my thesis. Also an extra thanks goes to Peter Mardahl for keeping the computers up and running for our group. There have also recent visiting scholars that have also offered valuable insights, namely Yuichi Ikeda, Naoki Matsumoto, Miles Turner, and Hide Usui.

I would like to thank Professor Y. Y. Lau at the University of Michigan for his physical sagacity and Dr. Phil Colella for his intuition in numerical mathematics (and for a great graduation party).

I would like to thank the I-house gang for making the graduate school experience a much more rewarding experience and for all the distraction and diversion that keep me sane all these years. A special thanks goes to Dan (Hair) Martin for proof-reading my thesis.

I would like to thank Peggy Jo Christenson, my fiancee, for her faith, inspiration, and encouragement. I would also like to thank her for her collaboration which has gotten me out of many mental cul-de-sac.

I would also like to thank the financial support of the taxpayers of the United States of America, who generously supported this work through the following grants and programs:

- Office of Naval Research AASERT N100014-94-1-1033
- Air Force Office of Scientific Research–MURI grant F49620-95-1-0253
- Air Force Office of Scientific Research grant F49620-98-C-OO53

Chapter 1

Introduction

Charged particle flow in crossed magnetic and electric fields is important in many devices in common use. This thesis is on flow in crossed-field pure electron plasmas; however, crossed-field flow also occurs in magnetized quasi-neutral plasmas. The purpose of this thesis is to understand the oscillatory steady-state behavior of crossed-field electron flow in diodes for magnetic fields greater than the Hull field ($B > B_H$) by the means of theory and self-consistent, electrostatic particle-in-cell (PIC) simulations. An overview of devices where crossed-field electron flow is important is given next.

1.1 Background

A magnetized quasi-neutral plasma generates electric fields near the boundary of the plasma though charge separation of the species. The underlying mechanism of the charge separation is the different diffusion rates of electron and ions across the magnetic field [2]. This causes a region of crossed-field flow near the boundaries. The nature of magnetized plasma sheaths still remains an important area of research. Magnetized plasma sheaths are important in understanding magnetically confined fusion prototype reactors (like tokamaks [3]) and processing plasmas (like electron cyclotron resonance (ECR) or helicon discharge [2]).

A Penning trap is another device where the electric field perpendicular to the magnetic field is caused by the electron space charge in the device. These devices have remarkable confinement times [4], which can be further lengthened by a "rotating wall"[5] which adds angular momentum back into the system. Penning traps have low density, generally far below the Brillouin limit, the plasma frequency being much lower than the cyclotron frequency ($\omega_p^2 << \Omega^2$). This is in contrast to crossed-field microwave generating devices which are general near the Brillouin limit.

1.1.1 Crossed-Field Microwave Devices

Much of this thesis is focused on devices that intentionally utilize crossed-field geometry by an external applied dc electric field. This configuration is common for the amplification and production of microwaves. Crossed-field microwave devices include the magnetron [6, 7, 8], relativistic magnetron [9, 10, 11], crossed-field amplifier (CFA) [12, 7, 13, 14], and the magnetically insulated line oscillator (MILO) [15, 16, 17, 11, 18, 19, 20, 21].

The MILO is a relatively new type of coaxial crossed-field device designed specifically to generate microwave power at the gigawatt level. Unlike other crossed-field microwave sources, the MILO uses the self-magnetic field produced by the current flow in the central cathode rather than the field from an external magnet to cut off electron flow to the anode. The MILO works by using a slow wave structure in the anode of the magnetically insulated line to generate microwaves by resonantly coupling the wave field to the electron flow. Thus, the operating mechanism is similar to that of the magnetron.

The magnetron oscillator is the microwave source that is used in microwave ovens; as well as in marine and commercial radar systems, reactors for material processing, and in medical linear accelerators. Magnetrons are a well established technology, having been invented by Arthur Hull in 1916 [8]. Shortly after the end of World War II the technological problems of the magnetron were essentially solved and the tubes have now been mass-produced for a number of years. They are robust, efficient and compact. However, the current understanding of its operation is incomplete especially with respect to noise and stability despite a considerable amount of attention over the years and the ubiquitousness of the magnetron. There is a cooker magnetron in almost every home in the United States.

The first relativistic magnetrons were reported in 1975 by Orzehowski and Bekefi [9], and later by Palevsky and Bekefi [10], and by Benford [11] and colleagues. Unlike the non-relativistic magnetron the relativistic magnetron is not efficient (typically 14 percent but as high as 40 percent) [11], but is still robust and compact.

The CFA, first built in 1953 [14], is a microwave amplifier of the same basic geometry as the magnetron. Like the magnetron they are also compact, robust, and efficient. This makes them ideal for radar systems; however, they are, in general, considered to be noisier than linear tubes such as traveling wave tubes (TWT) and klystrons. The basic mechanism for noise generation in crossed-field devices (CFD's) remains obscure; removing some of the obscurity is the motivation for Chapter 2 and 3 of this thesis.

The compactness of these microwave sources is ironically what makes them more difficult to understand than linear devices. In CFA's and magnetrons, the cathode is itself part of the interaction region for the microwave generation. The electrons are emitted by thermionic and/or secondary emission. Thermionic emission is used in this thesis. The numerical emission of electrons requires a high degree of accuracy because of the strong electric fields in the emitting region. Accurate numerical emission is discussed in Chapter 4. The emission process itself depends on the nature of the micro-sheath which depends on the electron flow in the drift region which, in turn, depends on the fields within the interaction

region as well as the self-fields of the electrons emitted from the cathode. This global feedback is the source of the nonlinearities and difficulties in analyzing CFD. Nonlinear feedback makes it difficult to break the system into realistic and analyzable pieces, which is possible with linear devices.

In linear (referring to the beam flow and interaction region) microwave devices such as gyrotrons, free electron lasers (FEL's), TWT's, and klystrons, the electron beam may be well formed and characterized, separate from the interaction region. This separates the cathode physics from the interaction region. Therefore the beam creation and beam optics which guiding the beam into the slow wave structure can be analyzed separate from the flow in the slow wave structure. Then the interaction of the beam and the slow wave structure can be analyzed together.

Some effort to understand the noise mechanisms and to produce "quieter" CFD has been made over the years [14, 22, 23, 24, 25, 26, 27]. However, this effort is insignificant next to the extensive research involving linear devices, with many publications. The lack of research and subsequent publication in the CFD field is maybe a reflection on the perceived difficulty of the problem [28].

Even with the lack of research, some headway has been made in the understanding of CFD's. Much of the theoretical groundwork occurred prior to the 1970's [1, 7, 13, 29, 30]. These studies involved not only characterizing the steady-state behavior in magnetrons [31, 32, 33, 34], but also the stability of the electron beams [1], especially with regard to the diocotron/magnetron modes or slipping stream (velocity shear) instabilities [35, 36] (Buneman p. 367 of [7] and Mourier p. 395 of [7]). This will be further expanded on in Chapter 3. Attempts to describe the noise mechanism were also made [22, 23, 24, 27, 37]. Much of the early work on the noise mechanism was done with the speculation that the noise was related to the existence of an unstable crossed-field potential minimum near the cathode [26]. In Chapter 2 the effect that the micro-sheath and potential minimum has on the spectrum is exposed and an equivalent circuit model is developed which reproduces the spectrum.

With the increasing speed of modern computers, simulations are performed with the hope of understanding CFD. Simulations fall under one of two approaches. The first one involves using a fluid approach to study the low frequency long-time behavior of CFD's [38, 39, 40, 41]. In this approach, the electron motion is general simplified by averaging over the gyro-motion leaving only the guiding center drift ($\mathbf{E} \times \mathbf{B}$) fluid motion of the electrons and a set of self-consistent, nonlinear equations for the fields and currents.

In contrast to the fluid approach, another approach is to use particle codes [42, 43, 44, 45, 46, 47, 48, 49]. This is the approach taken in this thesis. This method is more computationally intensive but, since it has fewer approximations, it is capable of obtaining closer agreement with experiment. Particle approaches are also a good tool to compare with simple theories that may explain the significant physics.

1.1.2 Magnetic Insulation

The emphasis of Chapter 3 is explaining the lack of magnetic insulation in CFD. A fair amount of effort has gone into the analytic and experimental understanding of magnetic insulation. A fundamental aspect of crossed-field flow is that both the single-particle and fluid descriptions of the electron motion in the dc field configuration predict a cutoff condition where there is no electron flux to the anode; that is, the electrons are insulated from the anode. This condition occurs when the magnetic field is greater than the Hull cutoff field [50]. There have been many anode-current experiment measurements showing that the cutoff law is not strictly obeyed [50, 51, 52, 53]. The addition of thermal emission from the cathode to the models was unable to explain the absence of a cutoff [54, 31, 33]. However, the addition of a thermal injection does "smooth" the cutoff and expands the Brillouin hub [55]. [1] Harvey [56] analyzed the effect of emission velocities, tilt of the magnetic field, unequal cathode potential, cathode eccentricity, space charge, and fringe fields and although the cutoff field could be appreciably increased, none of these effects could be found to account for the violation of the cutoff formula. The cutoff theory has been extended to the relativistic regime by [57, 58, 59] and departures from the theoretically cutoff condition for relativistic voltages have been shown in the experiment done by Orzehowski and Bekefi[9]. All of these theories are time independent.

Quasi-linear cold fluid approaches have also been used [60, 61, 62] where the oscillatory part of the solution is used to slowly change the evolving background density. A leakage current has been calculated by Kaup and Thomas [61, 62] using this approach. Another quasi-linear approach to diffusion in crossed-field devices uses the steady-state Fokker-Planck equation with quasi-linear diffusion coefficients to obtain the leakage current across an insulated diode [63].

There have also been attempts to explain the deviation from the cutoff condition using a statistical mechanics treatment [37, 64]. In this theory the diffusion tensor is proportional to the long wavelength growth rate of the shear flow instability described by Buneman [1]. The statistical mechanics approach done by Mouthaan and Susskind [37] agrees with experiments done at Berkeley by Hoag [65] in the 1950's. The validity of this theory was later disputed by Kuznetsov and Berbasov [66], because it did not agree with their experimental observations. A statistical approach was also taken by Hok [67] in which he calculated the space charge distribution in a magnetron. He assumed that the momentum changes were isotropic and that infinitesimal momentum changes have, by far, the largest probability, so that all momentum exchange may be considered to take place between adjacent volumes in phase space. This resulted in a space charge density that decreased linearly from the

[1] Brillouin flow is a time-independent 1d solution to the cold fluid equations, $v_x = 0$ and $v_y = -\Omega x$, where $\Omega = qB/m$ is the signed cyclotron frequency. The Brillouin flow density profile is uniform between $x = 0$ and $x = d_H$ with a density of $n_H = \epsilon_0 B^2/m$. This is the density at which the plasma frequency equals the cyclotron frequency ($\omega_p^2 = \Omega^2$). The hub height (extent of the electron sheath) is $d_H = L_x(1 - \sqrt{1-(B_H/B)^2})$.

potential minimum to zero at the anode.

1.2 Boltzmann electron PIC hybrid

In Chapter 5 a hybrid electrostatic PIC algorithm is developed to investigate ion acoustic waves and other long time-scale, low frequency phenomenon, as well as to provide acceleration schemes which decrease the computer time needed for a simulation to reach steady state. The ions are treated as finite–sized particles, as in standard PIC codes[46]. There are two models for the electrons. First, all electrons are modeled with a Boltzmann relation, in which the electrons are inertia-less and come to equilibrium with the ions at each time step. This is different than previous work in this area which did not allow the Boltzmann electrons to evolve in time with the ions[68, 69, 70, 71, 72, 73, 74]. The second model uses the Boltzmann relation for the low energy, less collisional electrons (up to the first excitation threshold), and kinetic PIC electrons for the remaining high energy, more collisional electrons.

Many different Boltzmann–PIC hybrid schemes have been proposed [68, 69, 70, 71, 72, 73, 74, 75, 76, 77, 78, 79, 80]. Some of these are full electromagnetic (Maxwell's curl equations) [76] or Darwin (magneto-inductive)[75, 77, 78, 79, 80]. There have also been electrostatic models [68, 69, 70, 71, 72, 73, 74] similar to the one presented here; however, those schemes have assumed that the plasma is either globally charge-neutral [71], the Boltzmann flux matches the ion flux [70] (note: this is different than the globally charge-neutral case because the simulation could have been started with a net charge), the flux of Boltzmann electrons from the boundary is zero [68, 69], or the density of the Boltzmann electrons is fixed (along with the potential) at a point in the simulation [72, 73, 74].

Our method is constructed to be suitable for bounded systems in which the density is dynamic and ambipolar diffusion is important, i.e., the plasma might develop a net positive charge, which slows the loss of electrons. The dynamics of the density are governed by enforcing charge and energy conservation. Also, to the author's knowledge, this is the first time ionization has been used with Boltzmann electrons in a PIC-Boltzmann hybrid code. The collisions are implemented using a modified MCC package based on work by Vahedi and Surendra[81]. (Note that Coulomb collisions were modeled between the Boltzmann electrons and ions by M. E. Jones et. al.,[75].)

1.3 Thesis Outline

Chapter 2 presents the theory and simulation of a 1d magnetically insulated crossed-field diode. The important features shown through theory and simulation are that electrons are hotter in the hub than the cathode temperature, and the dominant oscillations in the diode are found to be a series resonance, $Z(\omega_s) = 0$, between the pure electron plasma and vacuum impedance of the diode. The 1d series resonance in crossed-field electron flow

is shown to be the $k_y \to 0$ (one-dimensional) limit of the 2d diocotron/magnetron eigenmode equation [82]. The wavenumber, k_y, is the wavenumber perpendicular to the direction across the diode and magnetic field. Chapter 3 expands the 1d simulation in Chapter 2 to a periodic 2d simulation. The emphasis is now on the transport of electrons across the gap by the wave caused by the shear flow instability. Chapter 4 derives a new, more accurate numerical method used in injecting the electrons from the cathode essential for Chapters 2 and 3. The importance of accuracy in injecting the electrons from the crossed-field geometry is shown. Chapter 5 is on a new PIC Boltzmann electron hybrid useful in unmagnetized quasi-neutral plasmas. Two examples are shown depicting the effectiveness of this method.

Chapter 2

Characteristics of One-Dimensional Magnetically Insulated Crossed Field Electron Flow with Space-Charge Limited Emission

Submitted to Physics of Plasmas

2.1 Introduction

2.1.1 Motivation

Electron flows in crossed electric and magnetic fields occur in many devices such as magnetrons[7], crossed-field amplifiers[7], magnetically insulated diodes[50], and Penning traps[83]. The objective of this work is to study the effects of current injection on the steady state Brillouin hub and noise generation in a crossed-field diode. We examine the efficacy of modification of the cathode emission as a means of reducing unwanted signals. This study focuses on the response of the system to changes in the distribution of the electron flux emitted from the cathode.

We find that the dominant oscillations in the system are the one-dimensional (1d) limit ($k_y \rightarrow 0$) of the eigenmode equation in Davidson [82] Eq. 8.12.3 on page 502, from which the magnetron and diocotron modes can be derived. Eigenmodes of such systems were previously thought to require perturbation of electric fields in two directions [82]. Even though the cold fluid equations are used to obtain the eigenmode equation, the physical mechanism for each mode is different.

The mechanism for the diocotron instability is the coupling of two surface waves on two plasma vacuum interfaces with the body wave perturbation within the layer (Davidson page 336 [82]). In contrast, the series resonance may occur with one or two vacuum boundaries.

The magnetron instability occurs when the Doppler-shifted frequency of the mode is equal to the cyclotron frequency, $(\omega_r - k_y v_y)^2 = \Omega^2$ (Davidson page 500 [82]), within the electron hub. The series resonance does not need to satisfy this condition, which is why a $k_y \to 0$ limit exists.

One important aspect of this work is the discovery of the series resonance in crossed-field electron flow, including theory showing that the series resonance is the $k_y = 0$ cutoff of the 2d diocotron/magnetron dispersion. That is, the series resonance in crossed-field electron flow can be viewed as the 1d limit of the diocotron/magnetron mode.

Another important aspect of this work is the demonstration of the means to tune the circuit behavior of the system using magnetic field, injection current, and injection temperature. The magnetic field, which controls the density, is used to select the frequency of the series resonance; this is in contrast with the 1d unmagnetized case in which the density controls the series resonance [84]. By varying the injection temperature and current, the spectral width (damping) of the mode is changed, but not the peak in frequency.

In this article we first go over the history of the series resonance being the cutoff of a 2d surface wave (Sec. 2.1.2). Some of the historical work referenced is for unmagnetized plasma showing the ubiquitous nature of the series resonance and it's importance to devices other than those (magnetrons[7], crossed-field amplifiers[7], magnetically insulated diodes[50], and Penning traps[83]) which have crossed-field flow. In Sec. 2.2 we describe the simulation model and the 1d time-independent theory that is used to compare to the simulation. In Sec. 2.3 we describe the simulation results; in Sec. 2.4 the effect of current injection on the steady-state hub is described and discussed. We find that the thermal velocity in the hub is much hotter than the cathode, which is also found in experiment [85, 86, 87]. The component of injection velocity parallel to the cathode and perpendicular to the magnetic field is mostly responsible for this effect. In Sec. 2.5 the spectral content of the simulations are shown and analyzed, The series resonance is proposed to explain the spectra. The series resonance frequency has also be observed in experiment [88]. At the end of Sec. 2.5 we will show the connection between the 2d diocotron/magnetron eigenmode equation and the series resonance.

2.1.2 History

The cutoff frequency of surface waves, $k_y \to 0$, is found in many plasma configurations. D. J. Cooperberg's thesis [89] gives an up to date and detailed background for surface waves in quasi-neutral plasmas with much of his thesis material reflected in four articles [84, 90, 91, 92]. The coupling to the boundaries is the strongest at the series resonance frequency; therefore, at the series resonance the plasma is easily driven from the boundaries. Applications of driven surface waves include density-tunable quasi-neutral plasma sources [91], radial compression of non-neutral plasmas in Penning traps [5], and a density and temperature diagnostic [93].

In unmagnetized plasmas, the series resonance in a plasma column was first ob-

served and identified in 1931 by Tonks [94, 95]. This work was re-derived by Herlofson [96] in 1951 in a study of resonant scattering from the ionized meteor tails. Both of these theoretical studies used fluid theory with a uniform plasma to explain the main resonances. The main resonance is the same resonance that Swegle and Douglass found through simulation and theory in 1986 [97]. Secondary resonances observed in the experiments were not explained until temperature was added to the theory [98]. While a secondary spectrum was predicted, the spacing and location of the resonances were in poor agreement with experimental observation. The addition of a radial density profile was needed to obtain good agreement with experiment [93, 99, 100, 101].

Surface plasma waves were theoretically described by Trivelpiece and Gould [102] for a cold plasma cylinder bounded by dielectric and metal, with and without an applied steady axial magnetic field. Fig. 2 of Trivelpiece and Gould's paper shows as $k_y \to 0$ the surface wave approaches the series resonance; however, they did not include the v_y velocity shear in their cold dielectric constant, which is important in insulated crossed-field diodes.

The WKB (Wentzel-Kramers-Brillouin) method to obtain an approximate solution to the eigenmode equation (Davidson [82] Eq. 8.12.3 on page 502) was done by Kaup and Thomas [61]. The WKB approach taken to solve the eigenmode equation by Kaup and Thomas is different than the approach taken here; however, the solution at $k = 0$ is the same series resonance that will be derived in this paper. In both approximations the dispersions relation loses accuracy for larger k, but at different rates. Our solution reproduces the effect of the magnetron instability occurring at $(\omega_r - k_y v_y)^2 = \Omega^2$ which is absent from Kaup and Thomas's Fig. 3.

2.2 Model

A diagram of the 1d crossed-field gap model is shown in Fig. 2.1. An external magnetic field, B, is imposed parallel to the cathode surface. The Hull cutoff field, B_H, is defined as the minimum magnetic field for insulation [50], such that a single electron leaving the cathode with velocity v_{x0} perpendicular to the cathode and velocity v_{y0} parallel to the cathode would just make it to the anode: $B_H = \sqrt{2mV_0/eL_x^2 + (mv_{x0}/eL_x)^2} - mv_{y0}/eL_x$, where V_0 is the voltage across the diode, L_x is the diode gap separation, e is the absolute value of the charge of an electron, and m is the mass of an electron.

Thermal emission from the cathode is used in many of the cases explored in this study. In order to ensure insulation for thermal emission of the electrons to one part in $\sim 10^5$, we take $v_x = 3v_{tx}$ and $v_y = -3v_{ty}$ in the calculation of B_H, with $kT = mv_{tx}^2 = mv_{ty}^2$. The finite energy injection is a correction to the Hull cutoff field, and is important for calculating the series resonance for weaker magnetic fields slightly above the Hull field; this will be discussed later. This study is 1d and $B > B_H$, so no electron current is transmitted across the gap; however, there is a displacement current.

For magnetic fields larger than the Hull cutoff field the critical injection current

density, J_c [103], is defined as the largest current density for which a steady cycloidal flow solution exists. Cycloidal flow is defined as a steady state in which each electron executes a simple, cycloidal orbit and returns to the cathode with the same energy with which it was emitted. For injection currents above the critical current, electron flow is disrupted and a turbulent steady state is formed that is close to, but not exactly, Brillouin flow [55]. The injection current in the simulations in this paper is above the critical current; therefore, the flow is turbulent. For currents below the critical current, the cycloidal flow may be disrupted by a small rf voltage [104], by a small resistor added to an external circuit [105], or by a small misalignment of magnetic fields [106], resulting in an almost identical near-Brillouin flow in which the same frequency spectra occur as for turbulent flow above the critical current density.

In this paper we compare and contrast our results with ideal planar Brillouin flow. Ideal Brillouin flow is a time-independent 1d solution to the cold fluid equations, $v_x = 0$ and v_y = -Ωx, where $\Omega = qB/m$ is the signed cyclotron frequency. The Brillouin flow density profile is uniform between $x = 0$ and $x = d_H$ with a density of $n_H = \epsilon_0 B^2/m$. This is the density at which the plasma frequency equals the cyclotron frequency ($\omega_p^2 = \Omega^2$). The hub height (extent of the electron sheath) is $d_H = L_x(1 - \sqrt{1 - (B_H/B)^2})$. For ideal Brillouin flow, the electric field within the hub varies linearly with x as $E_x = \Omega B x$, and then becomes uniform ($E_x = \Omega B d_H$) in the vacuum region outside the hub [55]. Ideal Brillouin flow is used to provide a simple analytic model to compare with the simulation of a thermally emitting cathode for which the near-Brillouin hub has finite temperature electrons.

The base physical parameters we have chosen to model are as follows. The magnetic field, B, is 0.271 T ($\Omega = 2\pi 7.59 \times 10^9$ radians/sec). The distance across the diode, L_x, is 2.16 mm and the applied voltage, V_0, is 12 kV. For these parameters, the physical scaling characteristics are as follows. The hub height, d_H, is 0.485 mm, so $d_H/L_x = 0.224$. The Hull cutoff field, B_H, is 0.171T, so $B = 1.58B_H$. The Brillouin density, n_H, is 7.14×10^{17} m^{-3}. The electrons are injected with a current of 3×10^5 A/m^2, so $J = 1.42J_c$. These parameters are summarized in Table 2.1.

The particle emission model is also summarized in Table 2.1. Case 1 is isotropically injected thermal electrons at 1eV. This temperature is hotter than physical thermionic emitters and is used because the physical length scales are longer; therefore, fewer cells are required. Isotropic injection at 1eV is used later in the paper when the magnetic field is varied. Case 2 has no thermal spread in the transverse direction to the cathode (v_{y0}). This case is used to illustrate the large effect that v_{y0} has on the v_x-x phase-space. The emission in the x-direction is warm to reduce the fluctuations in the virtual cathode. Case 3 has a cold, drifting distribution in the normal direction and a thermal distribution in the transverse direction. The 1 eV drift in the x-direction keeps the density at the cathode finite, $\rho = J/v_{x0}$. Cold injection has larger amplitude virtual cathode oscillations than the warm cases. Case 4 has isotropic thermal injection at 0.25 eV. This injection temperature is approaching cathode temperatures used in laboratories.

Before discussing the results, a brief discussion of the numerical challenges encountered during this study is in order. The disparate length scales caused by the presence of a virtual cathode leads to difficulties in resolving a space-charge limited micro-sheath. The virtual cathode causes the formation of a micro-sheath that has a length scale much shorter than the Brillouin hub height. Using Poisson's equation, $\nabla^2\phi = -\rho/\epsilon_0$, and injection current density, $J = \rho\bar{v}$, a simple estimate of an unmagnetized micro-sheath length scale can be obtained by assuming a potential drop on the order of $kT \sim mv_t^2$ within the micro-sheath. The micro-sheath length scale is estimated to be $L_s^2 \equiv m\epsilon_0 v_t^2 \bar{v}/(eJ)$. Here, v_t is the thermal velocity, and $\bar{v}$ is the average speed of the particles normal to the cathode surface. For injection of a thermal distribution, $\bar{v}$ is on the order of v_t. (This formula is similar to the formula for Debye length, since $\bar{v}$ controls the density of the particle moving away from the cathode.) This unmagnetized length scale assumes that $|E| < |v_y B|$.

One consequence of the short space scales (L_s small) is a large gradient of the electric field at the wall, requiring the injected particles to be time-centered correctly [107]. The small grid spacing, Δx, needed to resolve the micro-sheath requires the use of a small time-step, Δt, to assure accurate sampling of the fields. The large density, $\sim 10n_H$, in the micro-sheath also constrains the time-step because of the need to resolve the plasma frequency, $\omega_p \Delta t < 0.2$, where $\omega_p^2 = e^2 n/(\epsilon_0 m)$. To resolve the characteristic scale lengths, the following numerical parameters are used in the simulation. The time-step, Δt, is 8×10^{-13} seconds and the grid size, Δx, is 0.0027 mm; therefore, there are 800 cells across the system. For this problem, the unmagnetized micro-sheath scale (L_s) for the 1 eV injection is 0.0035 mm, which is about 1.3 cells. We have done simulations with as many as 8192 cells (using double precision arithmetic) to as few as 50 cells and have found that the results do not change much for $\Delta x \lesssim L_s$.

One symptom of poor resolution is detachment of the Brillouin hub from the cathode, which is observed as a density depression after the micro-sheath. In Fig. 2.2, Case 3 shows detachment of the Brillouin hub because particles are injected with zero thermal spread in the x-direction (the transverse direction has the same thermal spread as Case 1). A zero thermal spread in the x-direction means that the length scale, L_s, becomes very small making resolution of micro-sheath difficult. In Case 4, there is a slight density depression after the micro-sheath indicating that detachment is beginning to occur. This is because the lower cathode temperature in Case 4, once again, makes resolution of the micro-sheath difficult.

2.3 Simulation Results

Fig. 2.2 shows the time-averaged density profiles for the four injection cases using the particle-in-cell (PIC) simulation code XPDP1[49], as well as the ideal Brillouin flow density profile. The dominant feature in both the ideal Brillouin flow and all of the PIC simulation cases is a sheared electron flow along the cathode (y-direction), Fig. 2.3. However,

All Cases	B $\hat{z}$	=	0.271 T (f_c = 7.587 GHz)
	L_x	=	0.00216 m
	V_0	=	12000 V
	d_H	=	487.7 μ m = 0.2258L_x
	n_H	=	7.106 $\times 10^{17}$ 1/m^3 (f_p = 7.587 GHz)
	B/B_H	=	1.58
Case 1 *isotropic*	J	=	3×10^5 A/m^2
	T_x	=	1.0 eV
	$T_\perp$	=	1.0 eV
Case 2 *v_x thermal only*	J	=	3×10^5 A/m^2
	T_x	=	1.0 eV
	$T_\perp$	=	0.0 eV
Case 3 *v_x cold only*	J	=	3×10^5 A/m^2
	T_x	=	0.0 eV
	$T_\perp$	=	1.0eV
Case 4 *isotropic*	J	=	1.45 $\times 10^5$ A/m^2
	T_x	=	0.25 eV
	$T_\perp$	=	0.25 eV

Table 2.1: A summary of parameters used in the four injection cases.

there are some differences between the two: (1) In ideal Brillouin flow there is no electron motion in the x-direction, whereas for the simulated near-Brillouin flow, there is a spread in the x-component of velocity, v_x, see Fig. 2.3. (2) A virtual cathode or potential minimum forms just in front of the cathode in the near-Brillouin flow. Because a thermal injection current is used in the simulations, the potential minimum is nearly steady with minimal oscillations, similar to warm virtual cathodes in non-magnetized diodes [108] (or Chapter 6 of Birdsall and Bridges [26]). Associated with this virtual cathode is a high electron density next to the cathode. (3) In the near-Brillouin flow there is a gradual decrease, or knee, in the PIC density profile near $x = d_H$. The knee in the density profile is caused by the thermal spread of the emitted current in the y-direction. (4) The final difference between the idealized flow and the near-Brillouin flow is oscillations in the current and potential within the diode, which were previously noted but unexplained in references [103] and [105]. Simulations indicate that the frequency of the peak in the spectrum is insensitive to the spread in the x-component of velocity, the virtual cathode, and the knee in the density profile (points 1-3). Hence, the peak of the frequency spectrum can be successfully explained by a cold theory which neglects these insensitive parameters; with the addition of damping, the shape of the spectrum is explained.

2.4 Effects of Injection on Time-Averaged Brillouin Flow

The time-averaged densities from the simulations are shown in Fig. 2.2 and phase-space in Fig. 2.3. One observation is that the thermal spread in the x-direction, $v_{xt}(x)$, is much larger than expected in the cases that have an initial thermal spread in the transverse direction, v_{yt0}. To illustrate this point, note that in Cases 1, 3, and 4 of Fig. 2.3, the thermal spread in the y-velocity, $v_{yt}(x)$, is about 1.0 eV. Compare this to the thermal spread in the velocity in the x-direction, $v_{xt}(x)$, which is much larger. Hotter than expected temperatures (9 eV) have also been seen in experiments done by Linder [85, 86] and corroborated by E. A. Ash [87] (quoted by G. D. Sims p. 183 [7]). This large thermal spread can be explained by single particle motion in ideal Brillouin flow. Using time-independent conservation of energy (and taking the cathode potential to be zero),

$$\frac{1}{2}m(v_{x0}^2 + v_{y0}^2) = \frac{1}{2}m(v_x(x)^2 + v_y(x)^2) + q\phi(x, \tag{2.1}$$

with the ideal Brillouin flow potential,

$$\phi(x) = -\Omega B x^2/2, \tag{2.2}$$

and momentum conservation in the transverse direction,

$$v_y(x) = -\Omega x + v_{y0}, \tag{2.3}$$

we obtain

$$v_x^2(x) = v_{x0}^2 + 2\Omega x v_{y0}. \tag{2.4}$$

Assuming that the initial thermal velocity in the x-direction, v_{xt0}, can be neglected for $x > L_s$ (the micro-sheath scale length) when compared to the average shear velocity, $\bar{v}_y(x)$, the thermal velocity in the x direction, $v_{xt}(x)$, is approximately:

$$v_{xt}^2(x) = 2\Omega x v_{yt0}. \tag{2.5}$$

In Fig. 2.3, the phase-space plots show that the spread is expanding approximately proportionally to x. This implies that much of the spreading of the velocity in the x-direction is due to a time-independent effect. There is still a time-dependent effect that can be seen in Fig. 2.3, Case 2 (the cold transverse injection case), by observing that, even in this case that the thermal spread in the x-direction is larger than 1.0 eV.

One consequence of the above observation is that a very small transverse velocity at the cathode is greatly magnified in the flow region. This increases the significance of the cathode temperature when compared to the diode voltage. Small changes of velocity in the transverse (y) direction at the cathode result in large changes in the x-velocity away from the cathode. Particle phase-space trajectories with the time-averaged potential from Case 1 are shown in Fig. 2.4; the left graph is a close-up of the cathode. The figure shows four characteristic particle orbits: The first trajectory, (a) $v_{x0} = 3$ and $v_{y0} = -3$, shows a

passing orbit that traverses the hub, returning to the cathode. The second trajectory, (b) $v_{x0} = 3$ and $v_{y0} = 0$, shows a passing particle that stays in the micro-sheath. The initial velocity transverse to the cathode (v_{y0}) is the difference between these two cases. The third case, (c) $v_{x0} = 3$ and $v_{y0} = 3$, also shows a passing particle in the micro-sheath. The last case, (d) $v_{x0} = 0$ and $v_{y0} = -3$, shows a trapped particle in the hub. The particles with $v_{x0} = 0$ and $v_{y0} = 0$ or $v_{y0} = 3$ do not have orbits in the system, nor do particles with $v_{x0} = -3$.

The effect of initial velocity in the y-direction can also be seen by comparing the thermal energy at the cathode,

$$\frac{kT(x=0)}{eV_0} = \frac{m\left(v_{yt0}^2 + v_{xt0}^2\right)}{2eV_0} \sim \frac{1}{12000} \tag{2.6}$$

to the thermal energy at Brillouin hub height,

$$\frac{kT(x=d_H)}{eV_0} \sim \frac{m\Omega d_H v_{yt0}}{eV_0} = \left(1 - \sqrt{1-(B_H/B)^2}\right)\frac{\Omega L_x v_{yt0}}{eV_0} \sim \frac{1}{216}. \tag{2.7}$$

The magnification of initial thermal velocity cannot be obtained from a straightforward application of the fluid equations (continuity, momentum, and energy conservation). This might be of consequence when calculating the energy flux across the diode, due to the gradient in temperature, $3n(x)m\bar{v}_x(x)\overline{v^2}(x)/2$, where $\bar{v}_x(x)$ is the average speed and $m\overline{v^2}(x)/2$ is the average energy of a particle.

2.5 Effects of Injection on Spectral Content of Brillouin Flow

Fig. 2.5 shows the Fourier transform of the potential in the middle of the system for Cases 1-4. All of the cases with thermal emission transverse to the cathode exhibit similar spectra. The peak frequency is insensitive to the injection temperature or the injection current, but is sensitive to the applied magnetic field, the diode length, and the applied diode voltage. This large, sharp response in the potential and current spectra does not occur for non-magnetically insulated diodes ($B < B_H$), where charges fill the diode and there is no vacuum region within the gap. These features will be explained by the circuit model of the diode formulated below.

2.5.1 Series Resonance

For this section we will focus on isothermal injection. The potential at the center of the diode for Case 1 is shown (without the other injection cases) as a function of frequency in Fig. 2.6; the large dc component ($\phi(f = 0)$=6870 V) is off the scale. The potential at the center of the diode shows a large signal at the same frequency, which is just below the cyclotron frequency, Ω.

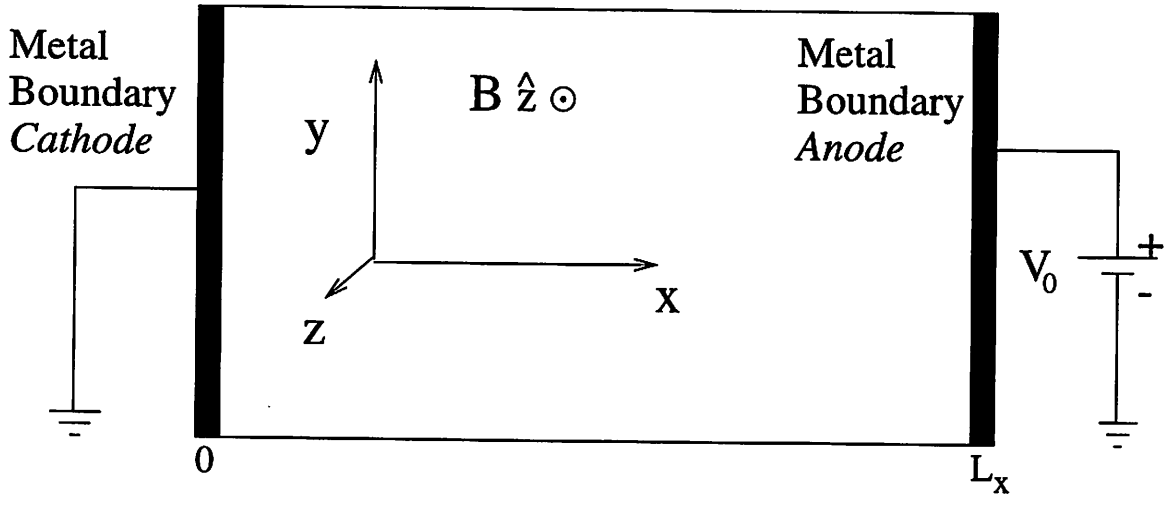

Figure 2.1: Diagram of 1d model

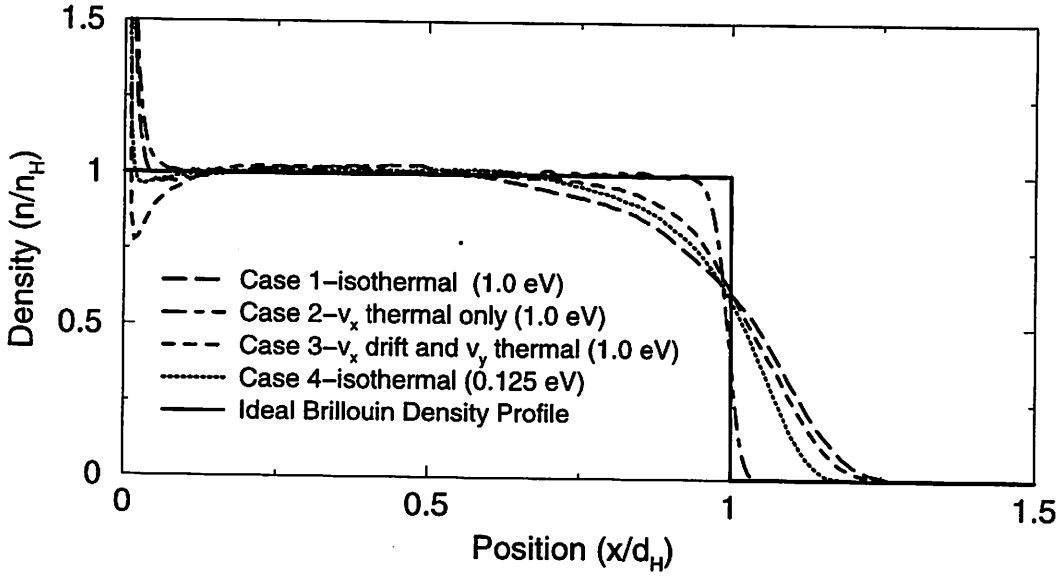

Figure 2.2: The time-averaged electron density for the four cases (note that $L_x = 4.43 d_H$).

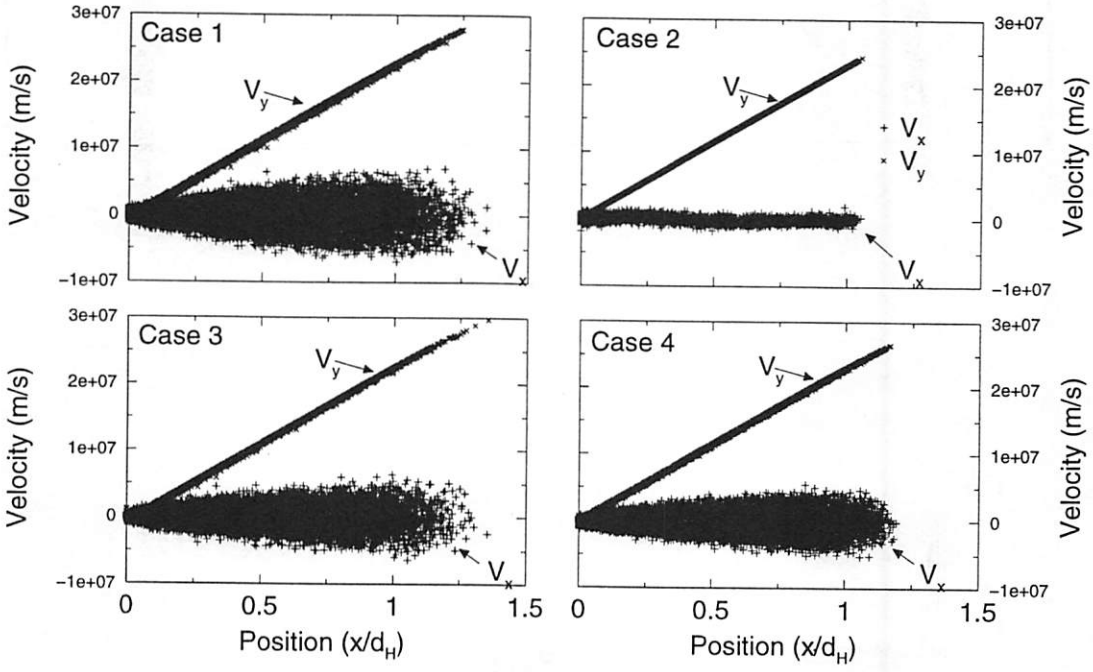

Figure 2.3: Phase space for the four cases. In Case 1, the injection is isotropic. In Case 2, the injection has a thermal velocity in the x-direction only. In Case 3, the injection is a cold beam with a 1.0 eV drift in the x-direction, and 1.0 eV thermal in the y-direction. In Case 4, the injection is isotropic with one fourth the temperature of Case 1.

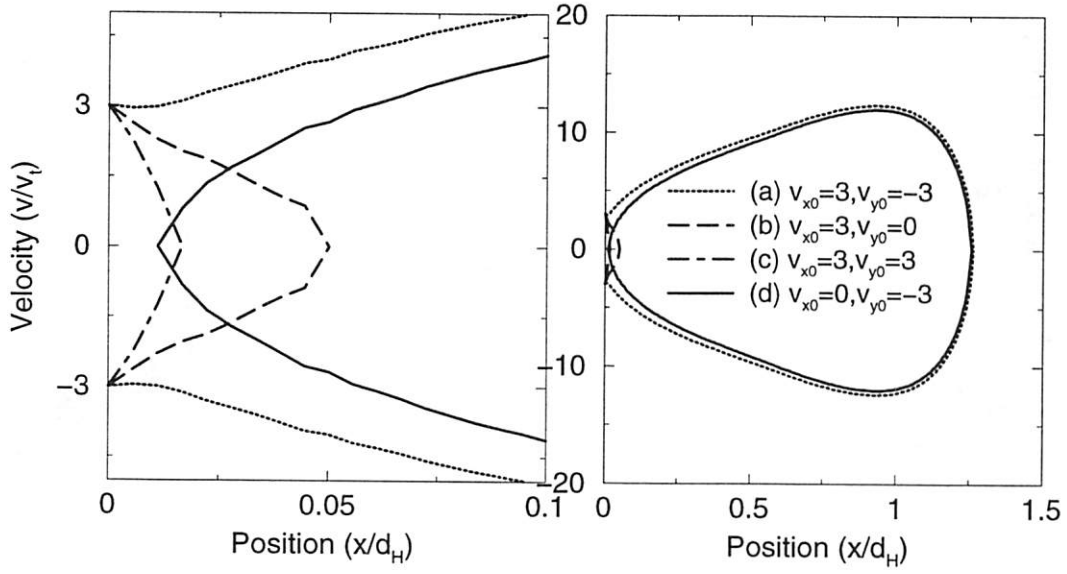

Figure 2.4: Trajectories in phase space for the time-averaged potential from Case 1 (isotropic injection 1 eV). This plot illustrates typical particle orbits contained in the micro-sheath (b and c), a trapped particle in the hub (d), and a passing particle orbiting around the hub (a).

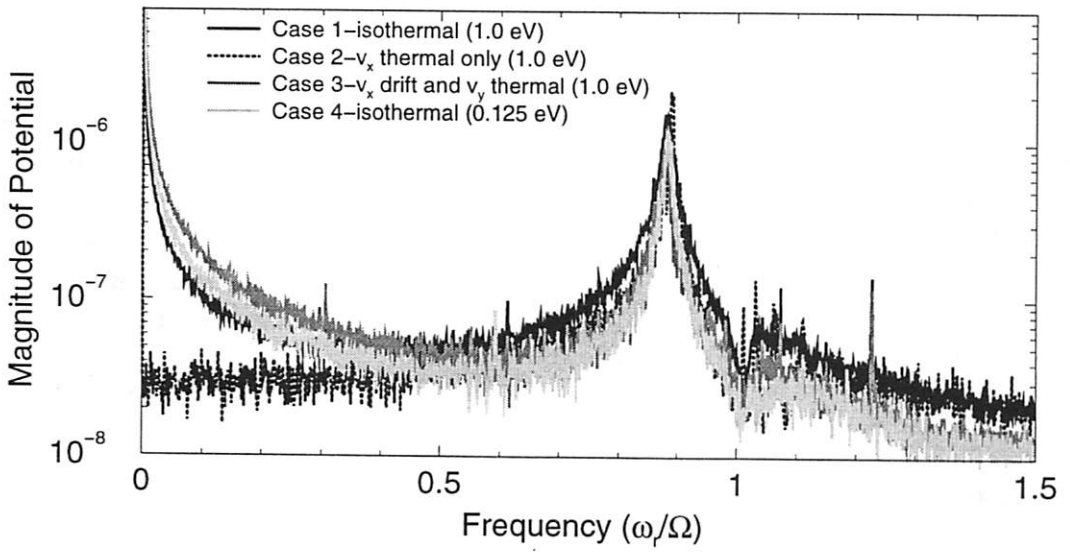

Figure 2.5: Fourier transform of potential versus frequency for the four cases summarized in Table 2.1.

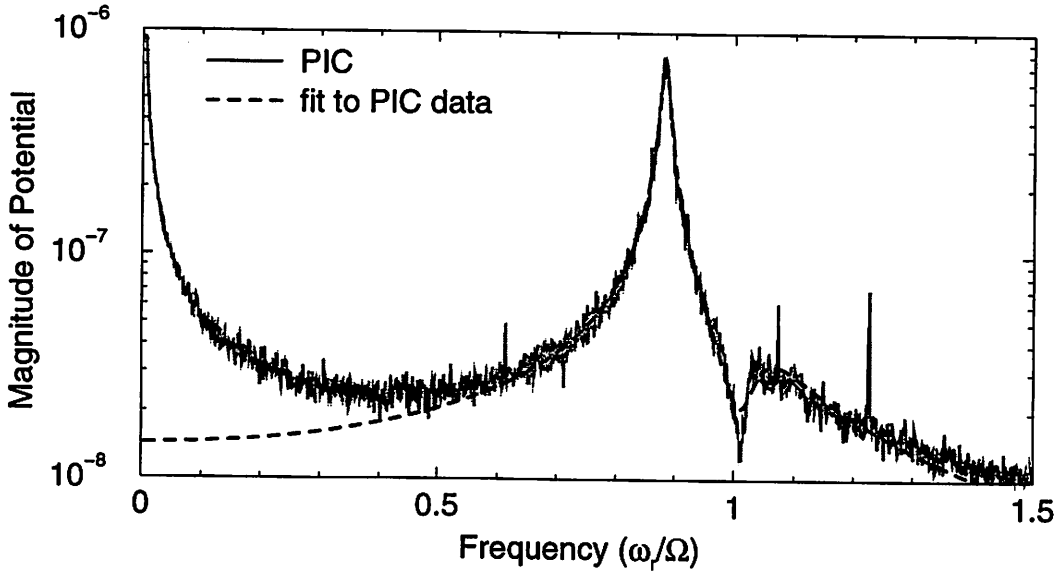

Figure 2.6: Fourier transform of potential (the peak of the DC component has been cut off, $\phi(f = 0) = 6870\ V$) at the center of the vacuum gap versus frequency. The fit is the circuit model described in the text.

The oscillations may be explained in terms of a series resonance between the electron-filled and vacuum portions of the diode. Beginning with the capacitance between parallel plates of area A and separation d,

$$C = \epsilon_0 \epsilon_R \frac{A}{d}, \tag{2.8}$$

the diode is modeled assuming the electron plasma region of the gap ($x < d_H$) is a cold plasma-filled parallel-plate capacitor, and the vacuum region is a vacuum capacitor. The relative and vacuum dielectric constants are ϵ_R and ϵ_0, respectively. It is shown below that the plasma dielectric constant has an inductive component independent of frequency.

In order to obtain the electron plasma dielectric constant in a magnetic field perpendicular to an electric field (same fields as in the diode being simulated), a fluid description is used. We employ the continuity equation,

$$\frac{\partial n}{\partial t} + \nabla \cdot (n\mathbf{u}) = 0, \tag{2.9}$$

and momentum conservation equation,

$$m(\frac{\partial \mathbf{u}}{\partial t} + (\mathbf{u} \cdot \nabla)\mathbf{u}) = q(\mathbf{E} + \mathbf{u} \times \mathbf{B}), \tag{2.10}$$

along with Gauss's Law,

$$\nabla \cdot \mathbf{E} = \frac{qn}{\epsilon_0}. \tag{2.11}$$

We follow the approach taken by Davidson on page 23-24 [82], but allow solutions which depend only on x with a time-independent term and an oscillatory time-dependent perturbation term:

$$n(x,t) = n_0(x) + \tilde{n}(x)e^{i\omega t}, \tag{2.12}$$

$$\mathbf{u}(x,t) = \mathbf{u}_0(x) + \tilde{\mathbf{u}}(x)e^{i\omega t}, \tag{2.13}$$

$$E_x(x,t) = E_{x0}(x) + \tilde{E}_x(x)e^{i\omega t}. \tag{2.14}$$

The velocity vectors represent component velocities: $\mathbf{u}_0(x) = (u_{x0}(x), u_{y0}(x))$ and $\tilde{\mathbf{u}}(x) = (\tilde{u}_x(x), \tilde{u}_y(x))$. Substituting Eqs. 2.12-2.14 into continuity, Eq. 2.9, and momentum conservation, Eq. 2.10, Gauss's Law, Eq. 2.11, and linearizing with respect to perturbed quantities, the steady-state part of the equations become (1d, electrostatic analog of Eqs. 2.41-2.46 of Davidson):

$$\frac{1}{2}\frac{\partial^2 u_{x0}^2}{\partial x^2} = \omega_p^2 - \Omega^2, \tag{2.15}$$

$$\frac{\partial(n_0 u_{x0})}{\partial x} = 0, \tag{2.16}$$

$$\frac{\partial u_{y0}}{\partial x} = -\Omega. \tag{2.17}$$

E_{x0} was eliminated in the simplification of the equations. Because there is no net particle current across the diode ($n_0 u_{x0} = 0$), to obtain a non-trivial density, i.e. $n_0 > 0$, the x-velocity must be $u_{x0} = 0$. Using this value of u_{x0} in Eq. 2.15 one concludes that $\omega_p^2 = \Omega^2$ (n_0 is constant). The y-velocity at the cathode does not need to be specified in order to solve this problem; only $\partial u_{y0}/\partial x = -\Omega$. There is another steady-state solution where $\partial u_{y0}/\partial x \neq -\Omega$; see the article by Christenson et. al.[105] for details on why the solution used here has $\partial u_{y0}/\partial x = -\Omega$. Briefly, the argument for this solution is as follows. The cathode emission fixes the v_y drift at the cathode to be near zero (thermal around zero); therefore the electric field is near zero ($v_y = (\mathbf{E}\times\mathbf{B})/B^2$). Due to conservation of momentum of each particle (not the fluid element), $\partial v_y/\partial x = -\Omega$; for particle momentum conservation, it does not matter if $v_x = 0$. (In the fluid momentum conservation equation if $u_x = 0$ then $\partial u_y/\partial x$ is not necessarily $-\Omega$. Once u_y is determined the electric field is established which in turn controls the density.) With $u_{x0} = 0$, $\omega_p^2 = \Omega^2$, and $\partial v_y/\partial x = -\Omega$, the linear perturbation equations reduce to:

$$i\omega\tilde{n} + n_0\frac{\partial \tilde{u}_x}{\partial x} = 0, \tag{2.18}$$

$$i\omega\tilde{u}_x = \frac{q}{m}\tilde{E}_x, \tag{2.19}$$

$$\frac{\partial \tilde{E}_x}{\partial x} = \frac{q}{\epsilon_0}\tilde{n}. \tag{2.20}$$

Eqs. 2.18-2.20 reduce to:

$$(1 - \Omega^2/\omega^2)\frac{\partial \tilde{E}_x}{\partial x} = 0. \tag{2.21}$$

Therefore, $\epsilon_R = 1 - \Omega^2/\omega^2$ is taken to be the cold plasma relative dielectric constant for shear flow. Note that the relative dielectric constant, ϵ_R, is real, reflecting that the cold fluid approximation has no loss mechanism and hence no plasma resistivity. The relative dielectric constant is negative for $\omega^2 < \Omega^2$; therefore, the plasma is inductive. To show the plasma inductance, L_p, we will separate the plasma inductance from the hub impedance, $Z_{hub}(\omega) = 1/i\omega C_{hub}$, where $C_{hub} = \epsilon_0\epsilon_R A/d_H = \epsilon_0(1 - \Omega^2/\omega^2)A/d_H$ is the cold electron plasma dielectric constant in a parallel-plate capacitor. The vacuum capacitance of the electron hub is defined to be $C_{d_H} = \epsilon_0 A/d_H$. Then the admittance, $Y_{hub}(\omega)$, of the parallel (LC) circuit representing the hub is

$$Y_{hub}(\omega) = \frac{1}{Z_{hub}(\omega)} = i\omega C_{d_H} + \frac{1}{i\omega L_p}. \tag{2.22}$$

Solving for the plasma inductance, we obtain $L_p = d_H/(\epsilon_0 A\Omega^2)$, independent of frequency. The diode impedance is

$$Z(\omega) = \frac{1}{i\omega C_{hub}} + \frac{1}{i\omega C_v} = \frac{1}{i\omega\epsilon_0 A}(\frac{d_H}{\epsilon_R} + L_x - d_H). \tag{2.23}$$

The series resonance occurs when the total diode reactance is zero ($X(\omega_s) = \mathrm{Im}(Z(\omega_s)) = 0$):

$$\omega_s = \Omega\sqrt{\frac{L_x - d_H}{L_x}} = \Omega\sqrt[4]{1 - (B_H/B)^2}, \tag{2.24}$$

for $B \geq B_H$.

Fig. 2.7 compares the resonance frequency (the peak of the spectrum) measured in the PIC simulations in mid-potential or current to the theoretical series resonance frequency, given above in Eq. 2.24, for various values of the magnetic field. Fig. 2.7 shows good agreement between theoretical series resonance and oscillations observed in simulation. The dominant frequency is the series resonance in a 1d crossed-field diode.

The series resonance frequency has been observed experimentally [88]. The figure showing these oscillations has been reproduced in Okress [7]. The experiment was done in cylindrical geometry; therefore the capacitance of concentric cylinders must be used in the derivation of the series resonance. The series resonance model fits the data better than the plasma oscillations or cyclotron frequency used in [88]. Only the peak of the frequency is shown versus applied magnetic field so the spectrum can not be compared.

We will now show that a small change in the Hull field as B approaches B_H results in a large change in the series resonance, Fig. 2.7; therefore, the initial velocities become more important. To quantify the effect of emission energy we will compare the series resonances with and without the thermal correction. We start with the Hull field for finite (but cold) injection energy: $B_H = \sqrt{2mV_0/eL_x^2 + (mv_x/eL_x)^2} - mv_y/eL_x$, and define the Hull field for zero injection energy as $B_{H0} = \sqrt{2mV_0/eL_x^2}$. The absolute difference in the series resonance between the case with finite injection energy and zero injection energy normalized to the cyclotron frequency, $\Delta\omega_s$, is:

$$\Delta\omega_s = \omega_s(B_H) - \omega_s(B_{H0}). \tag{2.25}$$

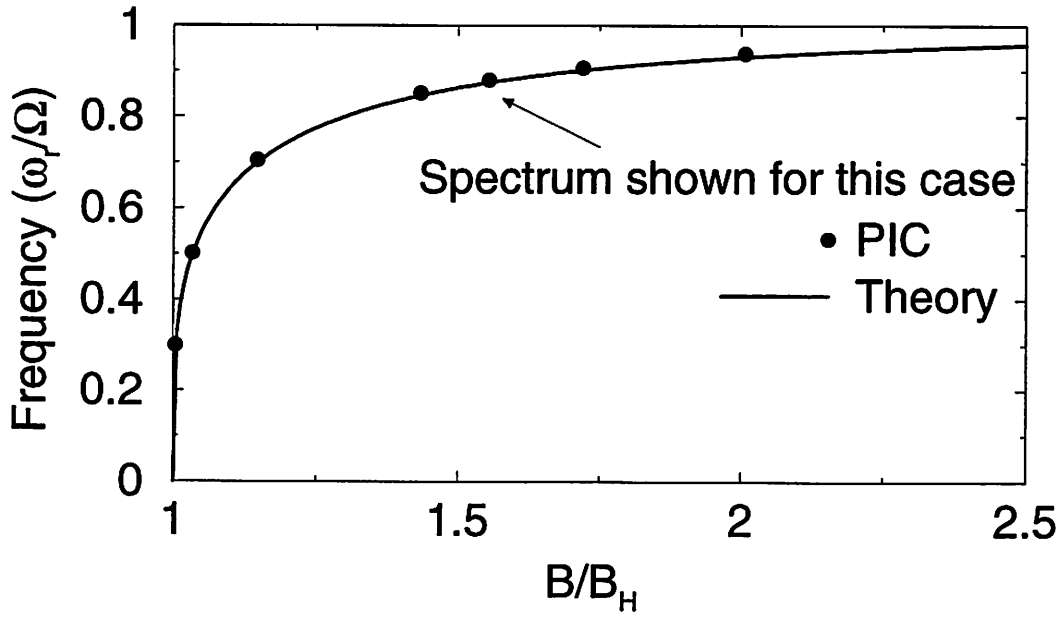

Figure 2.7: Series resonance found in a 1d diode gap versus normalized magnetic field.

Defining two small parameters $\epsilon_y = kT_y/eV_0$ and $\epsilon_x = kT_x/eV_0$, then expanding Eq. 2.25 we obtain:

$$\Delta\omega_s = \frac{1}{2}\left(\frac{B_H}{B}\right)^2\left(\frac{\Omega}{\omega_s}\right)^3\left(\sqrt{\frac{\epsilon_y}{2}} + \frac{3\epsilon_y}{8}\left(1+\frac{\Omega^4}{\omega_s^4}\right) - \frac{\epsilon_x}{4}\right). \tag{2.26}$$

This (Eq. 2.26) confirms the trend that as $B \to B_H$ ($\omega_s \to 0$), the effect of small emission velocities becomes more important. Note that the largest term in $\Delta\omega_s$ is proportional to the square root of the ϵ_y, so the emission temperature in the transverse direction is more important than the emission temperature perpendicular to the cathode. Also, the effect of the emission temperature is larger than one might first expect from the size of the small parameters ($\sqrt{\epsilon_y}$ is still small but it is a half-order correction, not a first-order correction).

Now we will expand on the simple circuit model for the plasma that we have developed in order to explain the spectrum of the potential in the middle of the diode by adding a voltage source to represent the noise of the particles and a resistor to represent loss of energy though collisions. The full circuit model is shown at the top of Fig. 2.8. Below the full circuit model, there are two limiting cases that describe the important features of the spectrum.

Starting with the parallel (LC) circuit representing the hub we add a resistance, $R_H = \nu_H d_H/(\epsilon_0 A\Omega^2)$ to the side of the circuit with the inductor. Note that $\epsilon_0\Omega^2/\nu_H$ is the conductivity of the plasma, where ν_H is the collision frequency in the hub. Adding R_H to the circuit is equivalent to adding a collision term, $-m\nu_H\mathbf{u}$, to the right-hand side of the momentum equation (Eq. 2.10). The source driving the oscillation (from particle

noise) in the hub circuit is modeled as an EMF, $\mathcal{E}_H(\omega)$. The micro-sheath is modeled as another source of noise, $\mathcal{E}_s(\omega)$, and resistance, $R_s = \nu_s L_s/(\epsilon_0 A\Omega^2)$, where ν_s is the collision frequency in the micro-sheath, and L_s is the micro-sheath scale length. The micro-sheath noise source, $\mathcal{E}_s(\omega)$, could also include the voltage fluctuation from the external voltage supply. The analysis of this linear circuit in Fourier space yields the total current, particle current plus displacement current, at any position in the system:

$$I(\omega) = \frac{\epsilon_0 A}{L_x} \frac{\Omega^2\omega\left(\omega\mathcal{E}_s(\omega)\nu_H + i\left(\mathcal{E}_s(\omega)\omega^2 - \Omega^2(\mathcal{E}_H(\omega)+\mathcal{E}_s(\omega))\right)\right)}{\omega_s^2\Omega^2 - \left(\Omega^2 + \nu_H\nu_s L_s/L_x\right)\omega^2 + i\omega\nu_s L_s/L_x\left(\Omega^2(1+\frac{\nu_H L_x}{\nu_s L_s}) - \omega^2\right)}. \tag{2.27}$$

It is illuminating to look at two limiting cases; the first is when the micro-sheath is not in the circuit ($\mathcal{E}_s(\omega) = 0$ and $\tau_s = 0$, Fig. 2.8, b). The resulting current is

$$I(\omega) = \frac{\epsilon_0 A}{L_x} \frac{\Omega^2\omega\mathcal{E}_H(\omega))}{\nu_H\omega + i(\omega^2 - \omega_s^2)}. \tag{2.28}$$

The relation between the current and the potential in the middle of the vacuum gap is

$$\phi_{mid}(\omega) = \frac{L_x + d_H}{i2\omega\epsilon_0 A} I(\omega), \tag{2.29}$$

90^o out of phase as expected for a capacitor. The magnitude of the potential in the middle of the vacuum gap is a Lorentz profile which may be written in the form

$$|\phi_{mid}(\omega)| = \frac{L_x + d_H}{2L_x} \frac{\Omega^2|\mathcal{E}_H(\omega)|}{\sqrt{(\nu_H\omega)^2 + (\omega^2 - \omega_s^2)^2}}. \tag{2.30}$$

To eliminate the micro-sheath from the simulation, a simulation was run with isotropic emission (Case 1) until it reached equilibrium. Then the particle injection was turned off and the spectrum calculated. A spectrum of the potential in the middle of the vacuum gap is shown in Fig. 2.9 with the cathode particle injection turned off with a fitted Lorentz resonance profile. Without the cathode micro-sheath the dip at the cyclotron frequency is removed as predicted by Eq. 2.30. This simplified potential spectrum formula (Eq. 2.30) shows that the collisions cause the width in the peak of the spectrum.

The other limiting case is with the source in the plasma turned off ($\mathcal{E}_H(\omega) = 0$, Fig. 2.8, c). This is the case when the virtual cathode oscillations are large or the system is driven though an external circuit. This circuit model results in the current response

$$I(\omega) = \frac{\epsilon_0 A}{L_x} \frac{\omega\mathcal{E}_s(\omega)(\nu_H\omega + i(\omega^2 - \Omega^2))}{\omega_s^2\Omega^2 - \left(\Omega^2 + \nu_H\nu_s L_s/L_x\right)\omega^2 + i\omega\nu_s L_s/L_x\left(\Omega^2(1+\frac{\nu_H L_x}{\nu_s L_s}) - \omega^2\right)}. \tag{2.31}$$

In Eq. 2.31, there is a dip (pole) in the frequency spectrum of the current when $\omega^2 = \Omega^2$. This circuit model also exhibits a peak in the frequency spectrum at ω_s. This circuit model represents the dominant mode if the system is driven from the boundaries.

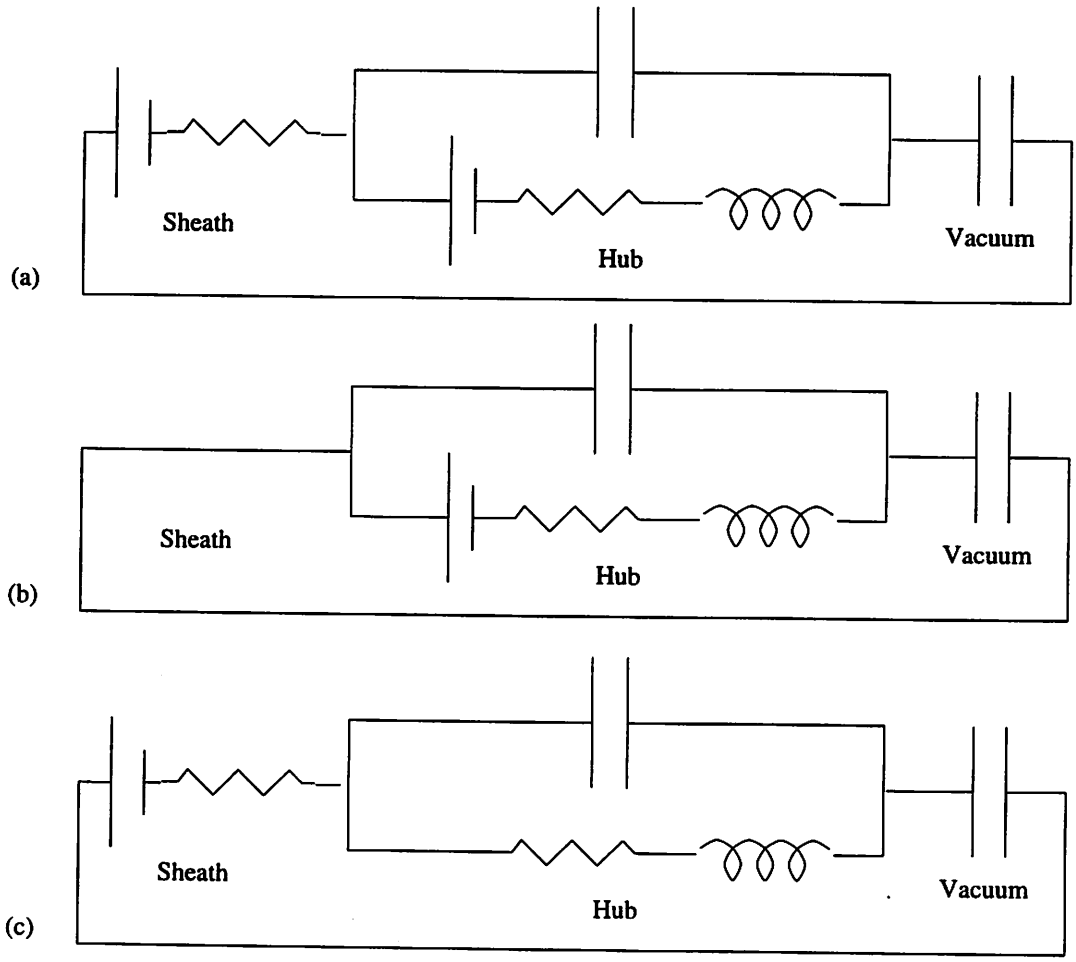

Figure 2.8: Diagram of the circuit model described in the text. The top circuit (a) is the full circuit model. The middle circuit (b) is a model of the hub without the virtual cathode. The bottom circuit (c) is a model where the virtual cathode (or external drive) dominates the system; this configuration gives the pole above the cyclotron frequency.

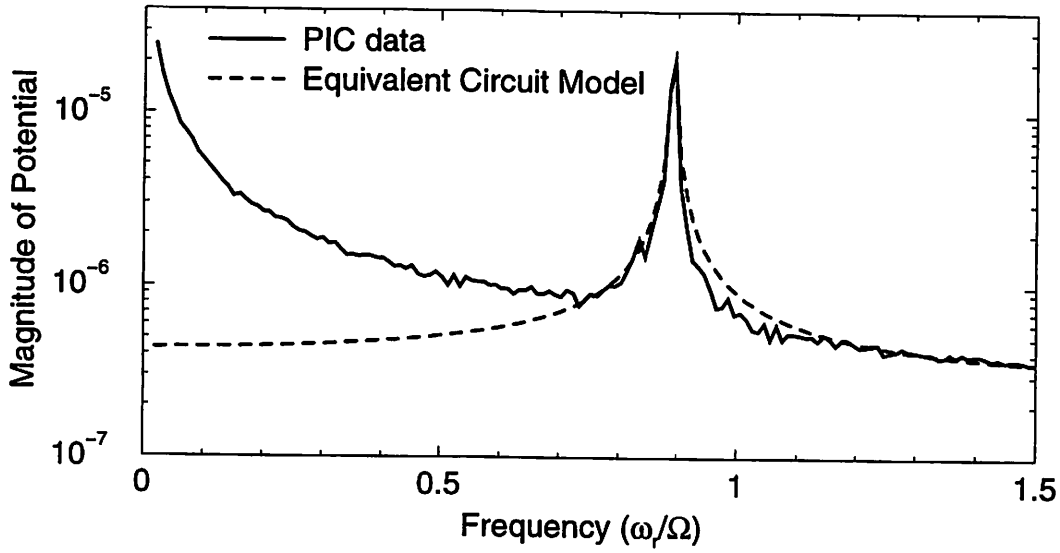

Figure 2.9: Fourier transform of potential versus frequency for Case 1 with the cathode injection turned off at the center of the vacuum gap. Turning off the cathode injection removes the dip in the spectrum around the cyclotron frequency.

To further analyze the frequency spectrum from the PIC simulation, the PIC spectrum is fitted to the circuit model spectrum. The circuit model has four free parameters: the collision frequency in both the plasma (ν_H) and the micro-sheath (ν_s), and the sources of the noise in the plasma ($\mathcal{E}_H$) and micro-sheath ($\mathcal{E}_s$). The magnitude of the potential is obtained in the middle of the vacuum region using the current (Eq 2.27) and the impedance of a vacuum capacitor of half the vacuum region (Eq 2.29). The magnitude of the potential in the middle of the vacuum region can be written as

$$|\phi_{mid}(\omega)| = \frac{(L_x+d_H)\Omega^2\left((\omega\mathcal{E}_s(\omega)\nu_H)^2+\left(\mathcal{E}_s(\omega)\omega^2-\Omega^2(\mathcal{E}_H(\omega)+\mathcal{E}_s(\omega))\right)^2\right)^{1/2}}{2L_x\left((\omega_s^2\Omega^2-(\Omega^2+\nu_H\nu_sL_s/L_x)\omega^2)^2+(\omega\nu_sL_s/L_x\left(\Omega^2(1+\frac{\nu_HL_x}{\nu_sL_s})-\omega^2\right))^2\right)^{1/2}}. \quad (2.32)$$

A fit to the spectrum of the potential in Fig. 2.6 is obtained using the Levenberg-Marquardt method [109] and is also shown in the same figure. The parallel resistor in the plasma driven by the virtual cathode appears as a dip in the spectrum that occurs slightly above the cyclotron frequency. The dip in frequency approaches the cyclotron frequency as collision frequency in the hub ν_H goes to zero. The micro-sheath collision frequency (ν_s) turns out not to be important in the fit of the model to the data. The 95 percent confidence interval for micro-sheath collision frequency is $0 \leq \nu_s/\Omega \leq 22$. The 95 percent confidence interval is defined as the range in parameter space that contains 95 percent of the total number of points in the PIC spectrum. Since, ν_s has a very small effect on the fit of model to the data from the PIC simulation it is set to zero. The collision frequency, ν_H, is shown as

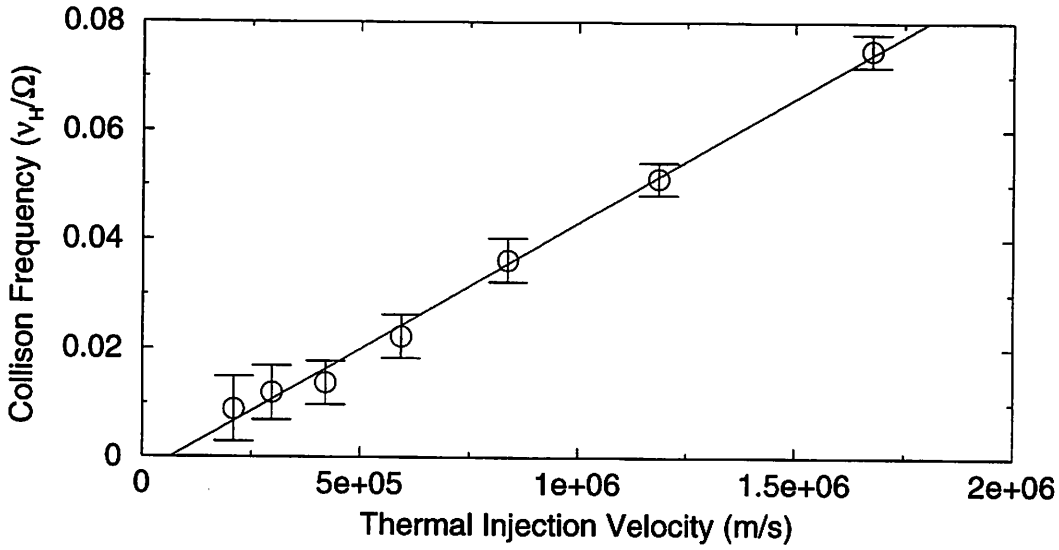

Figure 2.10: The collision frequency, ν_H, from PIC simulation as a function of the thermal injection velocity with the solid line showing the scaling of Coulomb collisions.

a function of the thermal injection velocity in Fig. 2.10 and as a function of the magnetic field in Fig. 2.11. The error bars in each figure shows the 95 percent confidence interval.

We will justify that that the type of collision causing this damping is 1d Coulomb collisions. For a 1d non-neutral plasma, the force between two particles is independent of the distance. Therefore, the Coulomb cross-section, σ, is independent of velocity. Hence, although PIC has a reduced force between particles within a cell, the relative error in 1d scales like the ratio of particles in a cell to the total number of particles, or as $\Delta x/d_H$ for a uniform density hub. The Coulomb collision frequency is $\nu_{e-e} = n\sigma v$, where n is density, σ is the Coulomb cross-section, and v is velocity. We take the velocity for the Coulomb collisions to be the thermal injection velocity, and the density is obtained from the relation $\omega_p^2 = \Omega^2$. The cross-section can be estimated from the simulation by the best-fit slope of collision frequency as a function of thermal velocity, Fig. 2.10; it is calculated to be $\sigma = 3.0 \times 10^{-15}\text{m}^2$. The slope of the line in Fig. 2.11 is calculated from the cross-section obtained from Fig. 2.10. This line is consistent with most of the data points. The two points for the lowest magnetic field might be invalid because not all of the particles are insulated from the anode in those cases. The non-neutral Coulomb collision scaling is different in higher dimensions so that the scaling of the damping in a laboratory device would be different than that shown here [110].

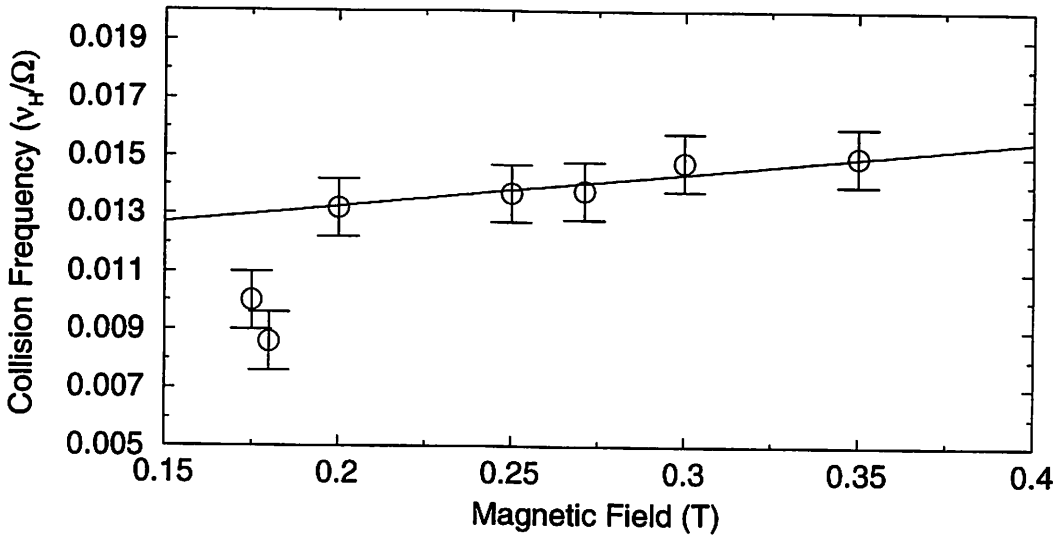

Figure 2.11: The collision frequency, ν_H, from PIC simulation as a function of the magnetic field with the solid line showing the scaling of Coulomb collision obtained from the fit to the data shown in Fig. /refdamping.v0.

2.5.2 The Relationship Between the Series Resonance and the Magnetron or Diocotron Mode

The relation between the magnetron mode or diocotron mode and the series resonance is is discussed in this section. Davidson's Eq. 6.28 [82] is the eigenvalue equation from which the diocotron dispersion is obtained; it was derived using the guiding-center approximation, which is good for low-density plasma ($\omega_p^2 \ll \Omega^2$). This approximation is not appropriate for the densities in the gap simulated here. However, the diocotron instability can also be derived from Eq. 5.56 of Davidson which uses the cold fluid equations [111, 1, 112], and is appropriate for comparison to our model. Eq. 8.12.3 of Davidson is used to find the magnetron mode and can be obtained from the single species, planar limit of Eq. 5.56. It is instructive to obtain the $k_y \to 0$ limit of those modes which do not result in the frequency going to zero. Starting with Davidson's Eq. 8.12.3 on page 502, the following equation is obtained:

$$\begin{aligned} \frac{\partial}{\partial x}\left(\left(1-\frac{\omega_p^2(x)}{(w-k_y v_y(x))^2-(\Omega^2-\omega_p^2(x))}\right)\frac{\partial\tilde{\phi}(x)}{\partial x}\right)-k_y^2\left(1-\frac{\omega_p^2(x)}{(w-k_y v_y(x))^2-(\Omega^2-\omega_p^2(x))}\right)\tilde{\phi}(x) \\ =\frac{k_y\Omega\tilde{\phi}(x)}{\omega-k_y v_y(x)}\frac{\partial}{\partial x}\left(1-\frac{\omega_p^2(x)}{(w-k_y v_y(x))^2-(\Omega^2-\omega_p^2(x))}\right), \end{aligned} \tag{2.33}$$

where $\tilde{E}_x(x) = -\partial\tilde{\phi}(x)/\partial x$. Using the same steady-state solution ($\omega_p^2 = \Omega^2$ and $v_y(x) = -\Omega x$) previously applied in calculating the cold dielectric constant, and expanding to first

order in k_y, we obtain

$$\frac{((\omega/\Omega)((\omega/\Omega)^2-1)-2k_y x)\frac{\partial^2\tilde{\phi}(x)}{\partial x^2}-2k_y\frac{\partial\tilde{\phi}(x)}{\partial x}}{(\omega/\Omega)^3}=0. \tag{2.34}$$

It is possible to let $k_y = 0$, in Eq. 2.34, recover Eq. 2.21, and then apply the boundary conditions below, and thereby obtain the series resonance. However, obtaining a dispersion relation and showing the transition from finite k_y to $k_y = 0$ lends stronger support to the theory that the series resonance is the cutoff of the 2d eigenmode equation. In the vacuum region, the eigenmode equation is

$$\frac{\partial^2\tilde{\phi}(x)}{\partial x^2}-k_y^2\tilde{\phi}(x)=0. \tag{2.35}$$

To first order in k_y, this is $\frac{\partial^2\tilde{\phi}(x)}{\partial x^2}=0$. At the boundary of the plasma ($x = d_H$), the normal electric displacement field and tangential electric field must be continuous, yielding

$$\epsilon_R\left.\frac{\partial\tilde{\phi}}{\partial x}\right|_{d_H^-}=\left.\frac{\partial\tilde{\phi}}{\partial x}\right|_{d_H^+} \quad \text{and} \quad ik_y\tilde{\phi}(d_H^-)=ik_y\tilde{\phi}(d_H^+). \tag{2.36}$$

The boundary conditions for the anode and cathode are $\tilde{\phi}(0)=\tilde{\phi}(L_x)=0$. Applying these boundary conditions we obtain the eigenmodes in the plasma:

$$\tilde{\phi}(x)=\begin{cases}\frac{c_1}{2k_y}\ln(1-\frac{2k_yx}{(\omega/\Omega)((\omega/\Omega)^2-1)}), & 0\le x<d_H,\\ c_1(x-L_x), & d_H<x\le L_x,\end{cases} \tag{2.37}$$

with the dispersion relation

$$\frac{L_x-d_H}{(\omega/\Omega)^3(1-\frac{2k_yd_H}{(\omega/\Omega)((\omega/\Omega)^2-1)})}=\frac{1}{2k_y}\ln(1-\frac{2k_yd_H}{(\omega/\Omega)((\omega/\Omega)^2-1)}). \tag{2.38}$$

The solutions to Eq. 2.38 are plotted in Fig. 2.12 for small values of k_y with $d_H = 0.224L_x$ together with the magnetron resonance condition ($(\omega_r - k_y v_y)^2 = \Omega^2$) using the maximum shear velocity ($v_y = -\Omega d_H$). The magnetron resonance and series resonance conditions are plotted on the same graph to show that the magnetron instability and series resonance mechanism are different. Our Fig. 2.12 is similar to the dispersion relation obtained by Kaup and Thomas and plotted in their Fig. 3 [61]. To finally obtain the limit as $k_y \to 0$, we need to apply l'Hôpital's rule to the dispersion relation, Eq. 2.38, and solve for ω. Upon doing so, we obtain the series resonance frequency of Eq. 2.24.

2.6 Conclusions

We have shown theoretically and through self-consistent PIC simulation that series resonance oscillations are the dominant oscillation in insulated ($B > B_H$) 1d crossed-field

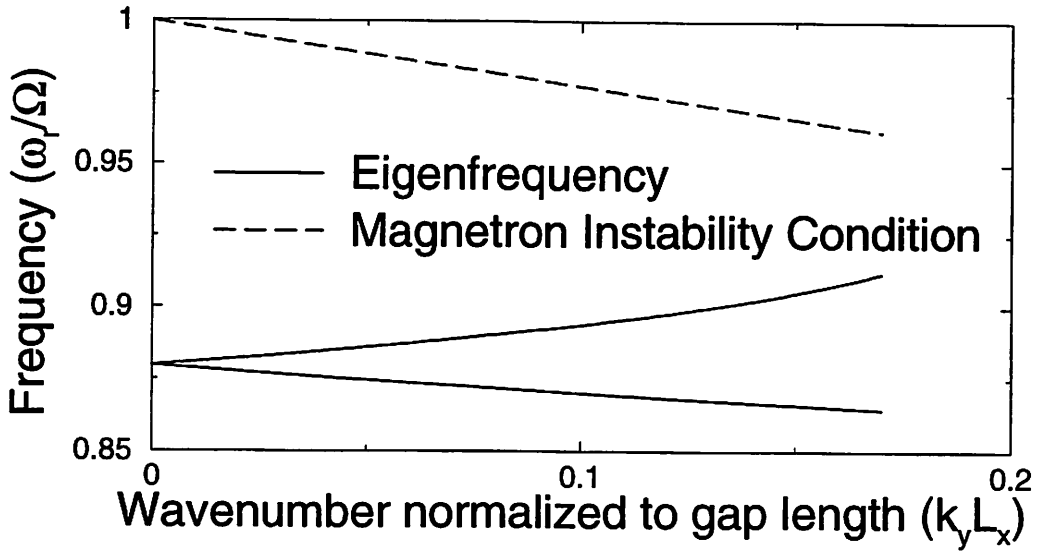

Figure 2.12: Dispersion relation for finite k_y (solid lines) showing that the $k_y \to 0$ limit of the mode is the series resonance. The magnetron resonance condition is also shown (dashed line). This shows that the magnetron instability and series resonance mechanism are different.

diodes. This resonance is the cutoff of the 2d eigenmodes of the diocotron mode and/or magnetron mode. The virtual cathode oscillations are shown to drive the series resonance as well as noise in the Brillouin hub. The time-averaged state obtained in PIC simulation is similar to ideal Brillouin flow. The series resonance is shown to be damped by Coulomb collision which depend on the the temperature of the electron hub. The hub temperature, which is much hotter than the cathode temperature, is shown to depend mostly on the initial velocity parallel to the cathode surface perpendicular to the imposed magnetic field.

Chapter 3

Surface wave enhanced collisionless transport in a bounded crossed-field non-neutral plasma

Submitted to Physics of Plasmas

3.1 Introduction

Electron flows in crossed electric and magnetic fields occur in many devices such as magnetrons[7], crossed-field amplifiers[7], and magnetically insulated diodes[50]. A fundamental aspect of crossed-field flow is that both the single-particle and fluid descriptions of the electron motion in the dc field configuration predict a cutoff condition where the electrons are insulated from the anode. This condition occurs when the magnetic field is greater than the Hull cutoff field [50]. There have been many anode-current measurements showing that the cutoff law is not strictly obeyed [50, 51, 52, 53]. The addition of thermal emission from the cathode was unable to explain the absence of a cutoff [54, 31, 33]. However, the addition of a thermal injection does "smooth" the cutoff and expands the Brillouin hub [55]. Harvey [56] analyzed the effect of emission velocities, tilt of the magnetic field, unequal cathode potential, cathode eccentricity, space charge, and fringe fields and although the cutoff field could be appreciably increased, none of these effects could be found to account for the violation of the cutoff formula. All of these theories are time independent.

Electron shear flow can be unstable to slipping-stream or magnetron instability which cause spontaneous field fluctuations in these diodes that was first explained by Buneman [1]. Various aspects of this instability have been studied over the years [82, 113, 114, 115]. The eigenmode equation for the slipping stream instability is described by Eq. 8.12.3 of Davidson on page 502 [82]. The magnetron instability occurs when the Doppler-shifted frequency of the mode is equal to the cyclotron frequency $((\omega_r - k_y v_y)^2 = \Omega^2$,

Davidson page 500 [82]) within the electron hub. Another instability that can be derived from the cold fluid equations is the diocotron instability. The diocotron instability mechanism is the coupling of two surface waves on two plasma vacuum interfaces with the body wave perturbation within the electron layer (Davidson page 336 [82]). This instability generally occurs for lower density sheared non-neutral electron flow where the guiding-center approximation can be made. These time-dependent fields can transfer energy and momentum to the particles.

Quasi-linear cold fluid approaches have also been used [60, 61, 62] where the oscillatory part of the solution is used to slowly change the evolving background density. A leakage current has been calculated by Kaup and Thomas [61, 62] using this approach. Another quasi-linear approach to diffusion in crossed-field devices used the steady-state Fokker-Planck equation with quasi-linear diffusion coefficients to obtain the leakage current across an insulated diode [63].

There have also been attempts to explain the deviation from the cutoff condition using a statistical mechanics treatment [37, 64]. In this theory the diffusion tensor is proportional to the long wavelength growth rate of the shear flow instability described by Buneman [1]. The statistical mechanics approach done by Mouthaan and Susskind [37] agrees with experiments done at Berkeley by Hoag [65] in the 1950's. The validity of this theory was later disputed by Kuznetsov and Berbasov [66], because it did not agree with their experimental observation. A statistical approach was also taken by Hok [67] in which he calculated the space charge distribution in a magnetron. He assumed that the momentum changes were isotropic and that infinitesimal momentum changes have, by far, the largest probability, so that all momentum exchange may be considered to take place between adjacent volumes in phase space. This resulted in a space charge density that decreased linearly from the potential minimum to zero at the anode.

In this paper, we take a single particle motion approach where the fast oscillation of the fields causes a slow net change in the canonical momentum of the electrons. The electron momentum changes slowly compared to the fluctuation of the fields. The fluctuation of the fields is on the order of the cyclotron frequency, and the transfer of canonical momentum takes place on the order of hundreds of cyclotron periods. We compare our theoretical estimation of the electron drift across a magnetically insulated smooth-bore diode ($B > B_H$) with self-consistent PIC simulations and find that this slow drift of electrons compares well with most of the crossed-field transport. This theory does not explain the rapid transport of electrons to the anode during a current spike. Similar bursts of electrons to the anode have been observed in experiments by Maron [116]. During the time of slow transport of the electron across the diode, the simulation looks qualitatively similar to the oscillatory steady-states that Kaup and Thomas obtain using a quasi-linear cold fluid approach [62].

3.2 Model

The model simulated in this study is a planar smooth-bore diode as shown in Fig. 3.1. We make use of Brillouin flow, a 1d equilibrium solution, to compare with our simulations and as the unperturbed solution for our crossed-field electron transport. An external insulating magnetic field (B) is imposed parallel to the cathode surface. The Hull cutoff field (B_H) is defined as the minimum magnetic field for insulation [50], such that a single electron leaving the cathode with velocity v_{x0} perpendicular to the cathode and velocity v_{y0} parallel to the cathode would just make it to the anode: $B_H = \sqrt{2mV_0/eL_x^2 + (mv_{x0}/eL_x)^2} - mv_{y0}/eL_x$. Here, V_0 is the voltage across the diode, L_x is the diode gap separation, e is the absolute value of the charge of an electron, and m is the mass of an electron. Ideal Brillouin flow is a time independent 1d solution (variation in x only, B in the z direction) to the cold fluid equation, $v_x = 0$ and $v_y = -\Omega x$, where $\Omega = q/Bm$ is the signed cyclotron frequency. The Brillouin flow density profile is uniform between $x = 0$ (cathode) and $x = d_H$ with a value of $n_H = \epsilon_0 B^2/m$; at this density the plasma frequency equals the cyclotron frequency ($\omega_p^2 = \Omega^2$). The hub height is $d_H = L_x(1 - \sqrt{1 - (B_H/B)^2})$. For ideal Brillouin flow, the electric field within the hub varies linearly with x as $E_x = \Omega B x$, and then becomes uniform ($E_x = \Omega B d_H$) in the vacuum region outside the hub [55]. Near-Brillouin flow has a small velocity spread in x, a gradual decrease in the density near $x = d_H$ and could have a virtual cathode with a high electron density next to the cathode. Thermal emission from the cathode is used in the PIC simulations explored in this study.

For magnetic fields larger than the Hull cutoff field the critical injection current density (J_c) is defined as the largest current density for which a steady cycloidal flow solution exists [103]. Cycloidal flow is defined as a steady state in which each electron executes a simple, cycloidal orbit and returns to the cathode with the same energy with which it was emitted. For injection currents above the critical current, electron flow is disrupted, and a turbulent steady state is formed that is close to, but not exactly, Brillouin flow [55]. The injection current in the simulations in this paper is above the critical current; therefore, the flow is turbulent. For currents below the critical current, the cycloidal flow has been found to be easily destabilized, and may be disrupted by a small rf voltage [104], by a small resistor added to an external circuit [105], or by a small misalignment of magnetic fields [106]. Once disrupted, the cycloidal flow collapses into a near-Brillouin flow that is almost identical to the turbulent flow resulting from injection currents above the critical current density. Ideal Brillouin flow is used to provide a simple analytic approximation to the near-Brillouin hub of the simulations. The simulations employ a thermally emitting cathode resulting in a finite temperature electron hub.

The base physical parameters we have chosen to model are as follows. The magnetic field (B) is 0.271 T ($\Omega = 2\pi 7.59 \times 10^9$ radians/sec). The distance across the diode (L_x) is 2.16 mm and the applied voltage (V_0) is 12 kV. For these parameters, the physical scaling characteristics are as follows. The hub height (d_H) is 0.485 mm, so $d_H/L_x = 0.224$. The Hull cutoff field (B_H) is 0.171T, $B = 1.58B_H$. The Brillouin density (n_H) is 7.14×10^{17}

m^{-3}. The electrons are injected with a current of 3×10^5 A/m^2; $J \approx 1.42 J_c$. The injection temperature is 1.0 eV, this is hotter than thermionic cathodes used in laboratories, but is used because it makes the space scales of the simulation larger, thus easier to resolve in simulation.

3.3 Slow Drift Theory

In this section we derive the slow change of the canonical momentum which drives the electron drift across the diode. The momentum change is caused by a ponderomotive-like force where the electrons are interacting with a surface wave. The wave is caused by the shear-flow instability and the net change of electron momentum from one cycle to the next is small. We estimate this change and the resulting transport that it causes across the magnetically insulated gap. We find that the slowly changing canonical momentum plays a larger role in the transport across the diode than the energy. There is no mechanism in our system that will impart enough energy to the electrons quickly enough to cause transport across the diode.

We obtain a ponderomotive-like force by adding a harmonically oscillating potential that is periodic in the y-direction to the 1d Brillouin steady-state. To obtain this ponderomotive-like force we will start with the Lorentz force equation for the electrons that is

$$\ddot{x} = \frac{q}{m} E_x + \Omega v_y \text{ and } \ddot{y} = \frac{q}{m} E_y - \Omega v_x. \tag{3.1}$$

Using the dc 1d Brillouin potential ($\phi_0(x) = -\Omega B x^2/2$ for $0 < x < d_H$ and $\Omega B d_H (d_H/2 - x)$ for $x > d_H$) and adding the harmonically oscillating solution that is periodic in the y-direction, the potential can be written as

$$\phi(x, y, t) = \phi_0(x) + \tilde{\phi}(x) e^{i(ky - wt)}. \tag{3.2}$$

Using the electrostatic approximation, the electric field is curl free and can be written as $\mathbf{E} = -\nabla\phi$. The electron trajectory is approximated as a harmonically oscillating solution added to the 1d steady-state Brillouin solution ($v_x = 0, v_y = -\Omega x + v_{y0}$). The electron trajectories can be written as

$$x(t) = x_0 + x_1 e^{i(ky - wt)} \text{ and } y(t) = (v_{y0} - \Omega x)t + y_1 e^{i(ky - wt)}. \tag{3.3}$$

The electron trajectories (Eq. 3.3) combined with the harmonically varying potential (Eq. 3.2) and Lorentz force equation (Eq. 3.1) constitute a linear problem in which the complex amplitudes of the perturbed trajectories can then be obtained in terms of the perturbed potential.

Since a quasi-linear approach is used to find the change in the canonical momentum, we changed the complex representation of the perturbed trajectories to a real one. This is because multiplying and taking the real part does not commute. The perturbed

potential (with an arbitrary phase chosen to be zero) is $\tilde{\phi}(x)cos(kx - wt)$ with $\tilde{\phi}(x)$ real. The instantaneous change in canonical momentum in the y-direction can be written as

$$\frac{\partial p_y}{\partial t} = m(v_y + \Omega x). \tag{3.4}$$

Using the linear solution to the perturbed potential (the change of momentum of the dc solution is zero) and expanding the amplitude of the perturbed potential to first order (i. e., $\tilde{\phi}(x_0 + x_1) = \tilde{\phi}(x_0) + x_1 \partial\tilde{\phi}(x_0)/\partial x$) and averaging over the Doppler shifted drive frequency $(kv_y - \omega)$, we obtain the average momentum lost in the y-direction during a cycle

$$\frac{\partial \bar{p}_y}{\partial t} = -\frac{q^2}{m}\frac{1}{4\omega\Omega}\frac{\partial \tilde{E}_y^2(x)}{\partial x}. \tag{3.5}$$

Calculating the electron trajectories in a frozen (dc) Brillouin hub, we can evaluate the importance of the changing canonical momentum and total energy. The allowed orbits can be calculated using energy and momentum conservation. Starting with the total energy,

$$H = q\phi(x) + \frac{1}{2}m(v_x^2 + v_y^2), \tag{3.6}$$

we obtain a 1d effective potential $\psi(x)$ which is a function of the canonical momentum $(p_y = mv_{y0} = m(v_y + \Omega x))$. The effective 1d potential is

$$\psi(x) = \frac{1}{2}m\left(v_{y0} - \Omega x\right)^2 + q\phi(x) \tag{3.7}$$

The effective potential is plotted in Fig. 3.2. To compare the relative effect of changing momentum and energy, we plot v_{y0} in the form $mv_{y0}^2/2$ so that it has units of energy. The sign of the momentum is ambiguous, but it is negative for the the cases plotted. Note that the shape of the potential well is independent of the electron energy. The change of the effective potential as an electron slowly loses canonical momentum is the underling reason that electrons are transported across the diode. The energy of the electron dictates where the particle will sit in the well. As seen in Fig. 3.2, changing the momentum is more effective in allowing an electron to move to the anode than changing the energy of the electron. A particle gaining energy can get closer to the anode; however, it is also allowed to return to the cathode. An electron that gains total energy will be quickly lost back to the cathode and will not be transported across the diode. An electron that has lost canonical momentum is unable to return to the cathode. The position of the effective potential minimum (x_{pm}) as a function of energy and canonical momentum is

$$m\Omega(\Omega x - v_{y0}) + q\frac{\partial\phi(x)}{\partial x} = 0 \tag{3.8}$$

For Brillouin flow (in the vacuum beyond the hub) the effective potential minimum is

$$x_{pm} = d_H - v_{y0}/\Omega. \tag{3.9}$$

The position, x_{pm}, is the equilibrium point of an electron with canonical velocity v_{y0}. The potential well is not harmonic, therefore, electrons with different energy will have different oscillation periods. The other point that is clarified in Fig. 3.2 is that once the electron loses momentum or energy, it is isolated from both the anode and the cathode. Hok refers to these electrons as 'secular' (in Okress[7]). Although all electrons that are collected by the anode are at one time 'secular', the space charge (as shown by simulation) of these electrons does not overwhelm the space charge of the Brillouin hub. The electrons that are transported across the gap have a low space charge so the electrons in the Brillouin hub control the fields.

3.4 Simulation Results

A diagram of the simulation region is depicted in Fig. 3.1. A sufficiently high thermal electron current is injected from the cathode such that a near-Brillouin flow is formed. Fig. 3.3 shows the growth rate for the dominant electrostatic mode in the simulation (the solid line) and the growth rate for the same mode as predicted by Buneman, Levy, and Linson [1] (the dashed line). The theoretical model also predicts that this dominant mode is the fastest growing mode.

After the initial transient has past, and the mode has saturated, the following data were taken. Fig.s 3.4 and 3.5 show the x velocity, v_x, versus x, and y velocity, v_y, versus x phase space plots respectively. Both plots indicate that electrons extend out beyond the Brillouin hub, that is, beyond $x = 1$ in the plots. Notice that the v_x-x phase-space indicates a much hotter population (approximately 15 eV in the near-Brillouin hub) than might be expected based on the injection temperature of 1 eV. This apparent heating of the electron hub has be seen in experiment [85, 86], corroborated by E. A. Ash [87] (quoted by G. D. Sims p. 183 [7]), and explained in reference [117]. The v_y-x phase-space plot shows the shear flow in the Brillouin hub and in the electrons beyond the hub. The v_y-x phase-space clearly shows that the electrons beyond the hub region have a lower y-velocity than expected based on the relation $v_y = v_{y0} - \Omega x$. The lower y-velocities indicate the loss of momentum to the time varying electric field described above in the theory. The canonical y momentum, p_y, versus x phase space plot, Fig. 3.6, and the total energy, H, versus x phase space plot, Fig. 3.7, indicate the loss of both momentum and total energy, respectively, as the electrons traverse the diode.

The momentum in Fig. 3.6 is normalized to the momentum required for an electron to reach the anode with zero velocity in the x direction. The total energy in Fig. 3.7 is normalized to the energy that would be gained by an electron falling through the voltage drop of the diode. Figures 3.6 and 3.7 show that the electrons in the simulation have finite v_x as they impact the anode.

The density is plotted in Fig.3.8 showing the Brillouin hub and the electron spoke. The density in Fig.3.8 has been smoothed slightly by taking a time average of the density

over a period that is short compared to the motion of the spoke.

In order to measure the collective transport of electrons, we inject marked electrons rather than the normal PIC electrons over a time of roughly five cyclotron periods, a short time compared to the time it takes the particles to traverse the diode. The marked electrons are injected after the initial transient, i.e., after saturation of the magnetron mode. The average position of the marked electrons is plotted as a function of time in Fig. 3.9. Fig. 3.9 shows linear behavior in time after an initial transient that is related to the marked electrons entering the Brillouin hub. This linear behavior can be recovered theoretically through the use of Eq. 3.9 and Eq. 3.5 by taking the time derivative of Eq. 3.9 and substituting Eq. 3.5 into that expression. The drift in this paper has the same dependence on the eigenmodes as the flux in the quasi-linear cold fluid approach taken by Davidson [60] (namely $\partial \tilde{E}_y^2(x)/\partial x$). Kaup and Thomas have used this quasi-linear method to calculated the second-order DC current density [61].

As the electrons slowly move across the diode the tip of the density spoke comes into contact with the anode and a current spike due to the expulsion of electrons occurs. The wave form of a typical current spike is shown in Fig. 3.10, and the average distance of all the electrons from the cathode is shown in Fig. 3.11. The time-averaged density before the current spike is shown in Fig. 3.8, and the time-averaged density after the current spike is shown in Fig. 3.12. The size of the density perturbation in the spoke greatly decreases during the current pulse. The electron spoke gradually drifts across the diode, but once it reaches the anode a rapid loss of some of the electrons in the spoke occurs.

The spoke density will build up again, and the process will repeat itself. The interval between the current spikes is not constant in time, nor is the total charge deposited by each current spike a constant. Maron [116] has found similar results experimentally, that is, variably sized current bursts and a varying time between bursts. While it is theoretically possible to obtain a statistical comparison between experiment and PIC simulation within a reasonable amount of time, it would take more computer power than is currently available. Our goal in this study was to obtain qualitative agreement with experiment to confirm the mechanism for electron transport across a magnetically insulated diode.

An extension of this work would be the addition of an slow-wave anode structure to the simulation. The anode structure may have significant effect on the dynamics of the system. We have chosen the smooth-bore anode because it is the simplest structure.

3.5 Conclusion

Electron transport across a magnetically insulated diode has been described in terms of a ponderomotive-like force driving the electrons across the magnetic field. This theorized mechanism predicts a transport of electrons linear in time across the magnetic field. The theory is in good qualitative agreement with the results of self-consistent 2d PIC simulation. While it is beyond the scope of the theory, the slow transport of electrons across

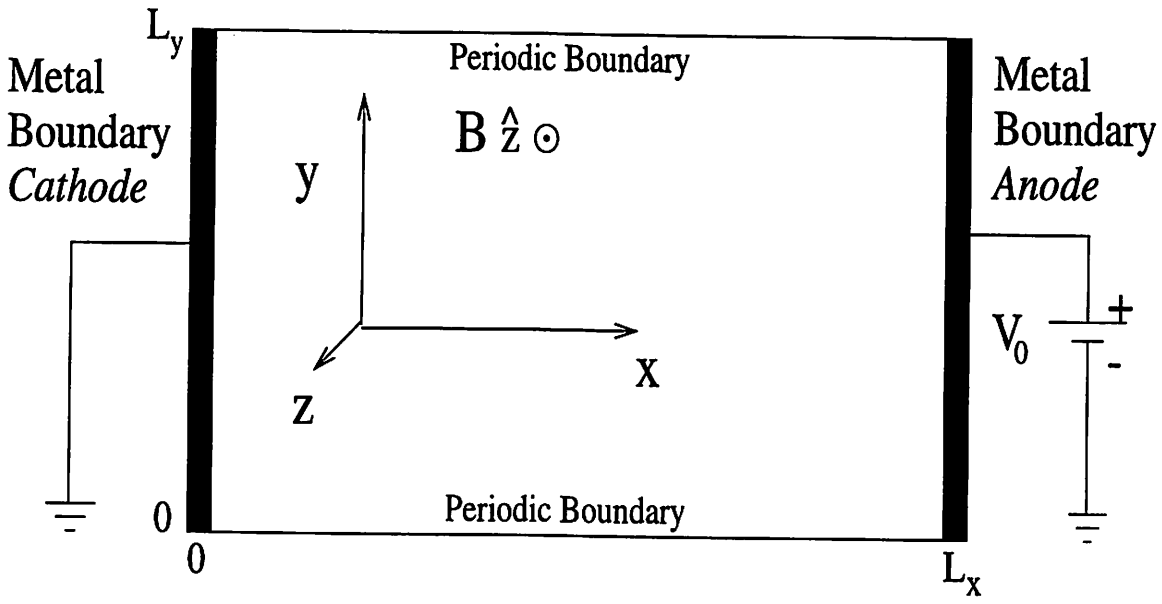

Figure 3.1: Diagram of 2d smooth-bore diode model.

the diode is punctuated by current spikes due to rapid loss of electrons to the anode. The current spikes have also been experimentally measured in smooth-bore crossed-field devices and noted in literature[116]. Qualitative agreement between the PIC simulations reported on in this study and the experimental observations reported in literature is noted; however, a detailed comparison to experiment is beyond the scope of this paper.

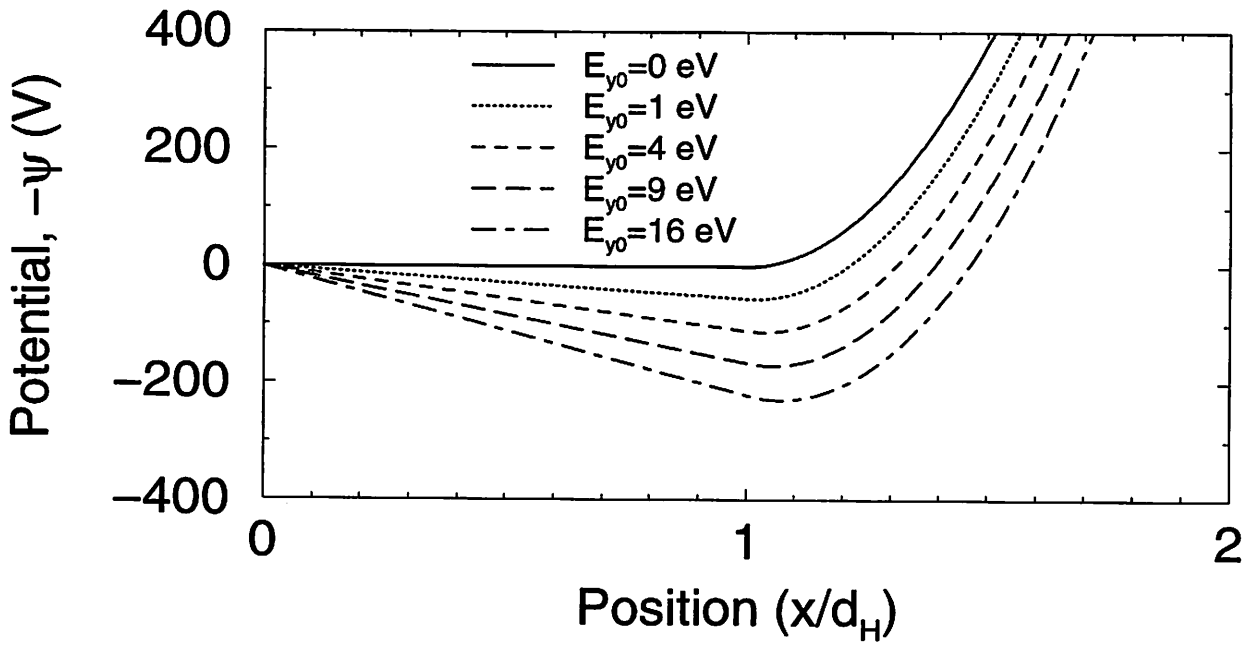

Figure 3.2: The 1d effective potential, $\psi(x) = 1/2m(v_{y0} - \Omega x)^2 + q\phi(x)$. This shows the change of the effective potential as the momentum of the a electron is modified by the ponderomotive-like force.

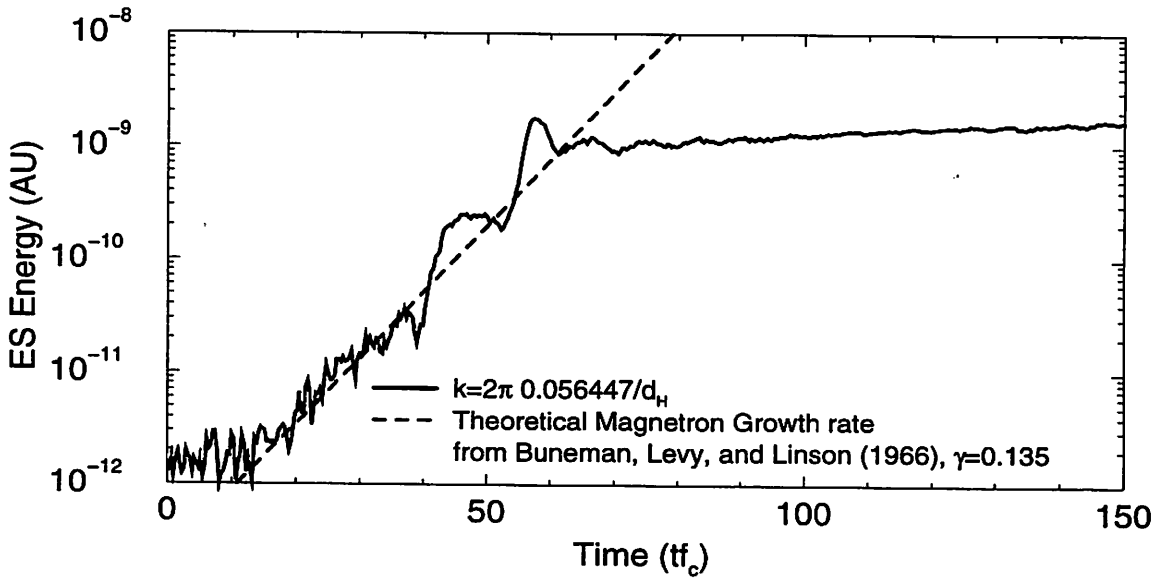

Figure 3.3: The growth in electro static energy in time, plus the theoretical growth from Buneman, Levy, and Linson [1].

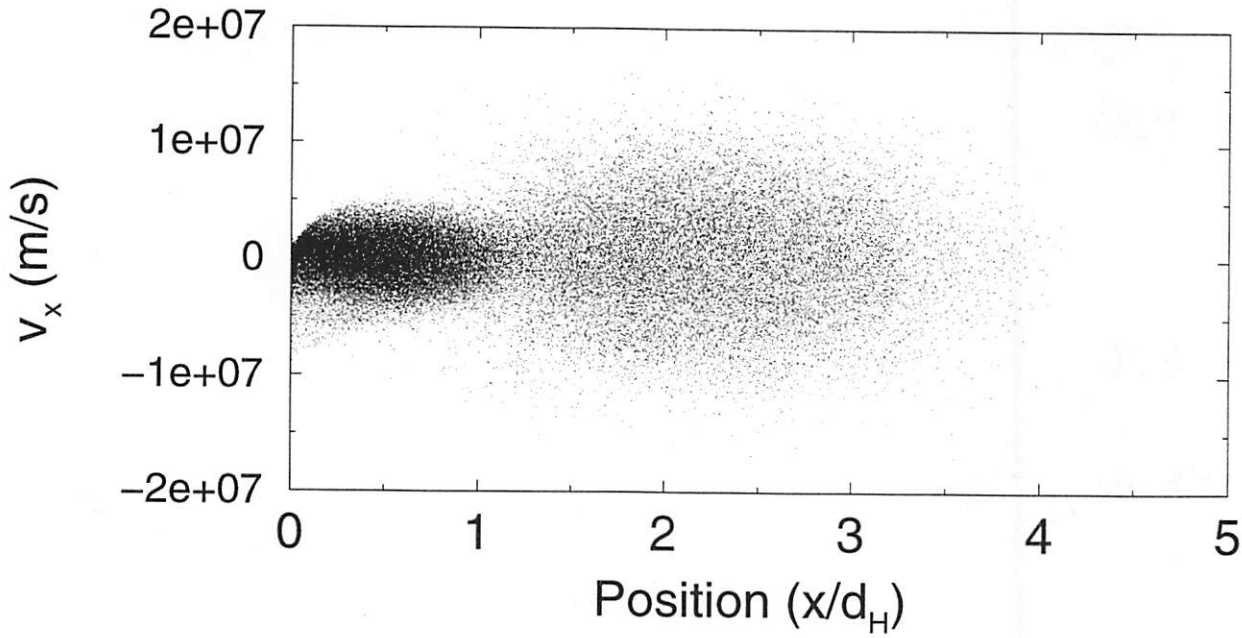

Figure 3.4: The v_x-x phase space. The anode is located at $x/d_H = 4.46$, d_H is the Brillouin hub extent.

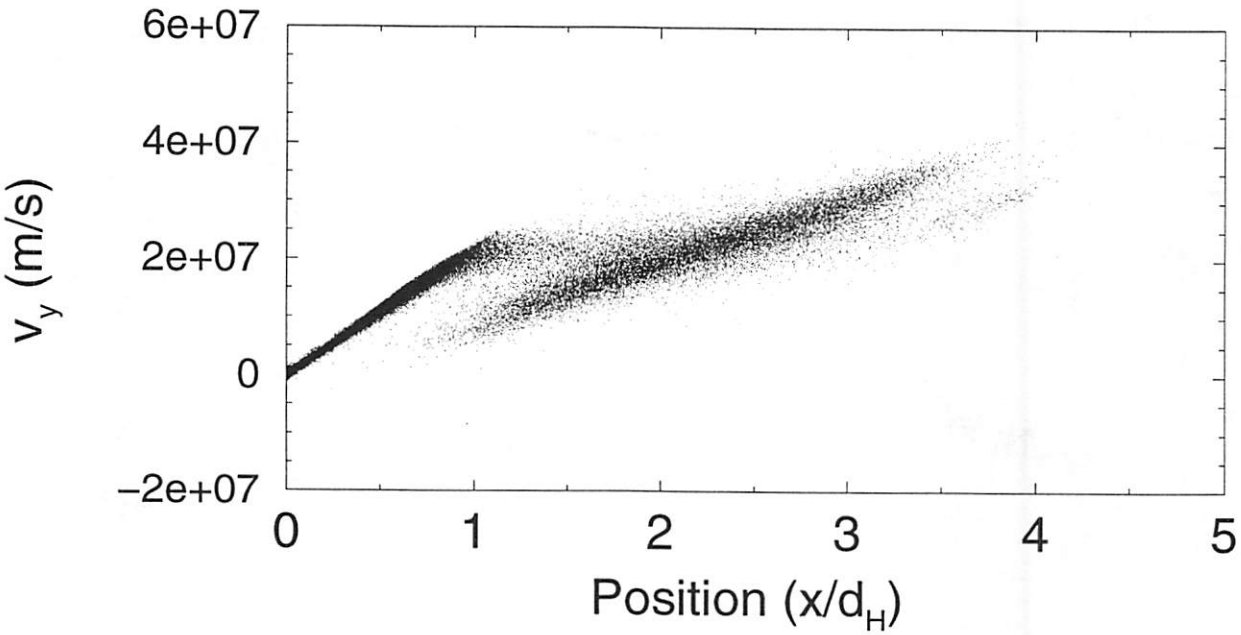

Figure 3.5: The v_y-x phase space showing the shear flow in the Brillouin hub. The anode is located at $x/d_H = 4.46$, d_H is the Brillouin hub extent.

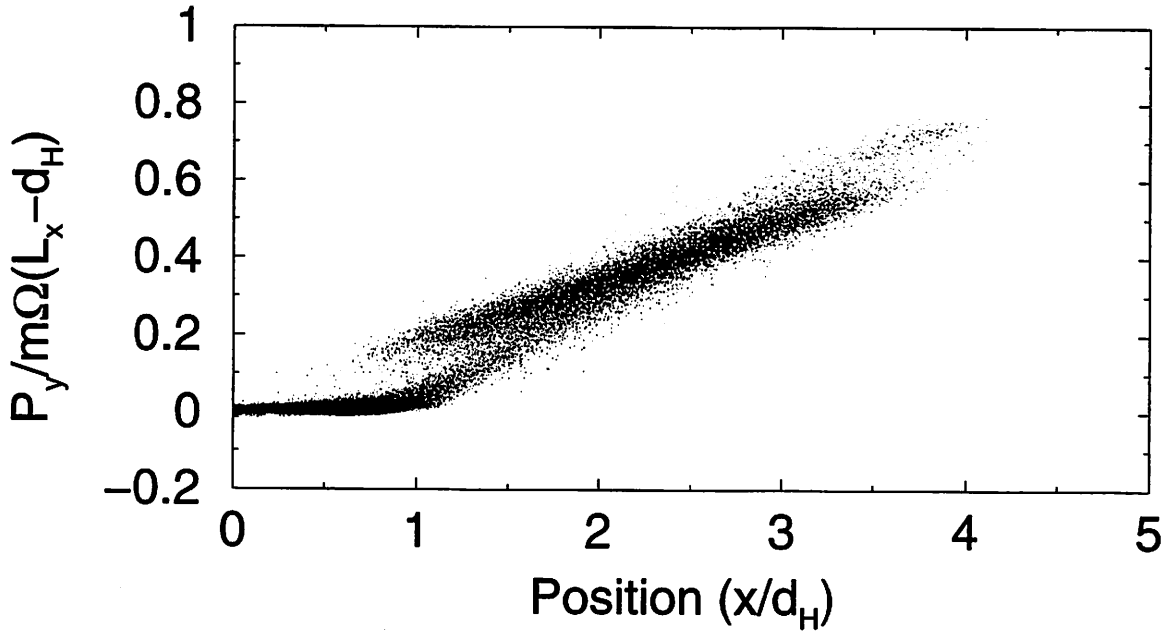

Figure 3.6: The normalized canonical momentum in the y-direction normalized to the canonical momentum required to traverse the diode with $v_x(x = L_x) = 0$ as a function of position. The anode is located at $x/d_H = 4.46$, d_H is the Brillouin hub extent.

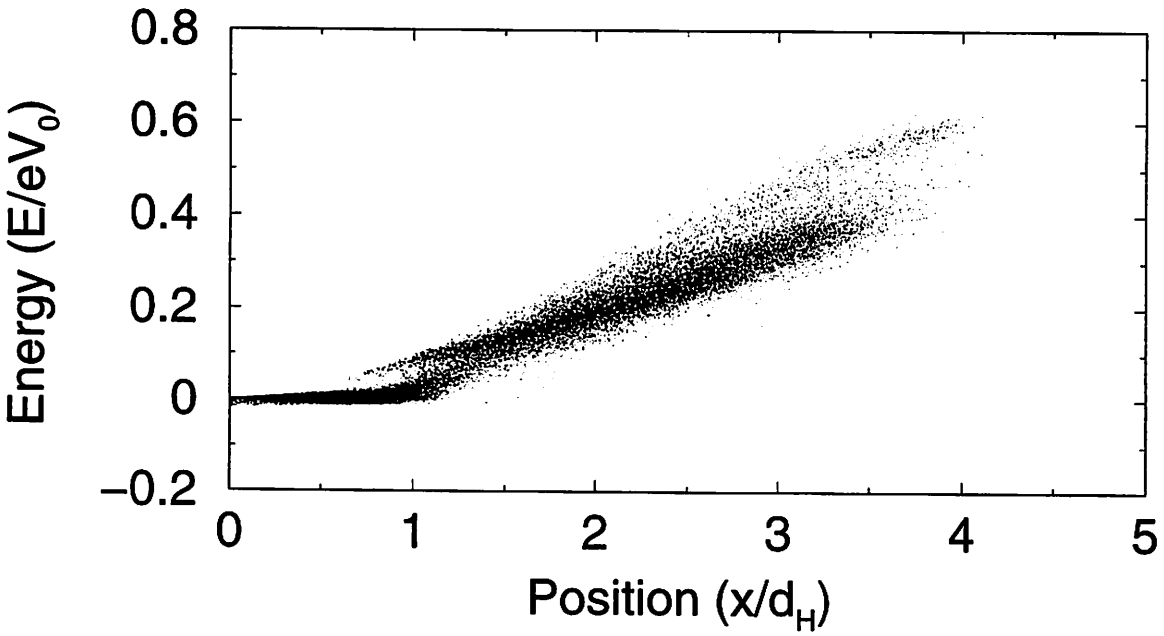

Figure 3.7: The normalized total energy as a function of position. The anode is located at $x/d_H = 4.46$, d_H is the Brillouin hub extent.

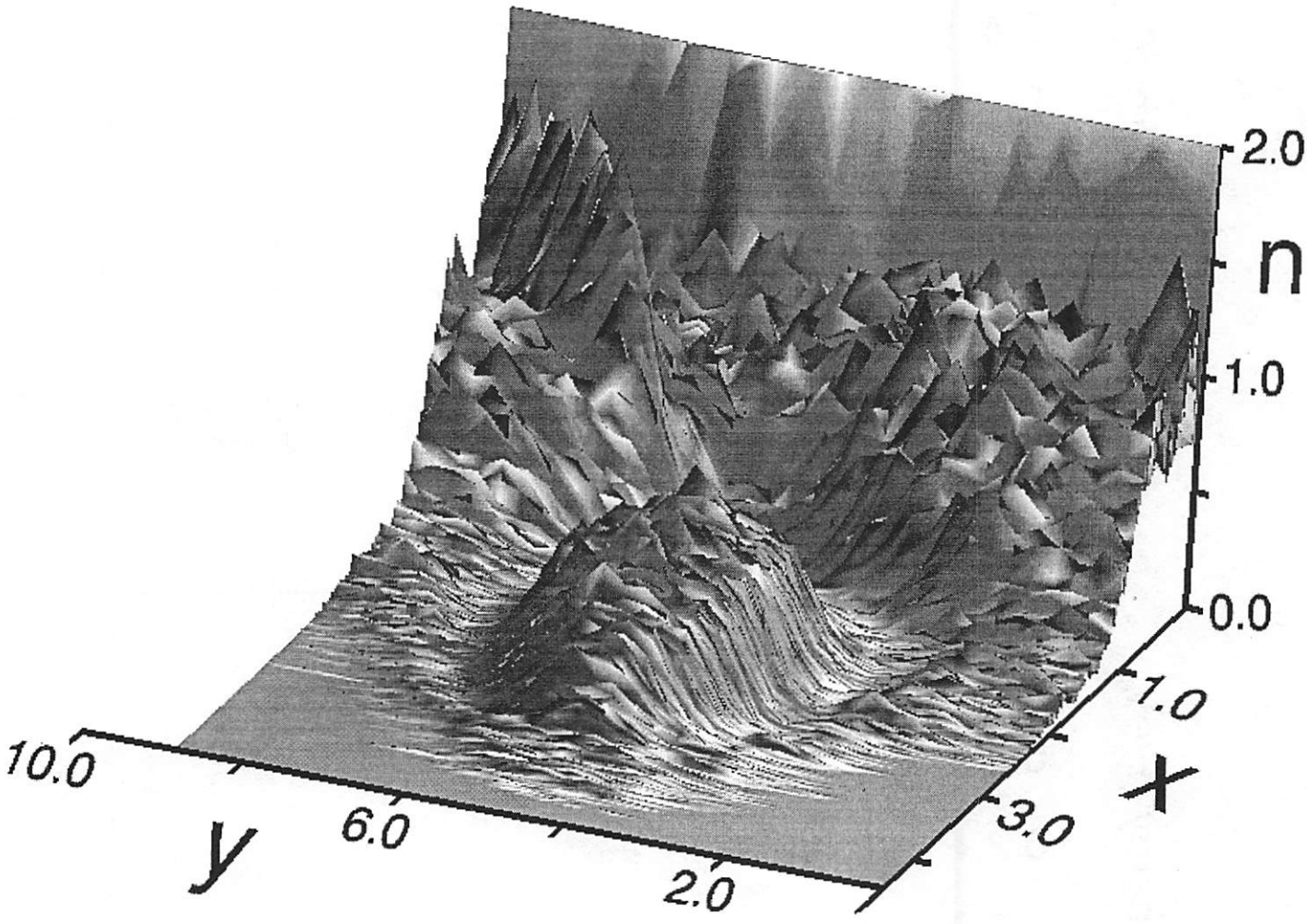

Figure 3.8: The density in the crossed-field diode showing the Brillouin hub and spoke beyond the hub.

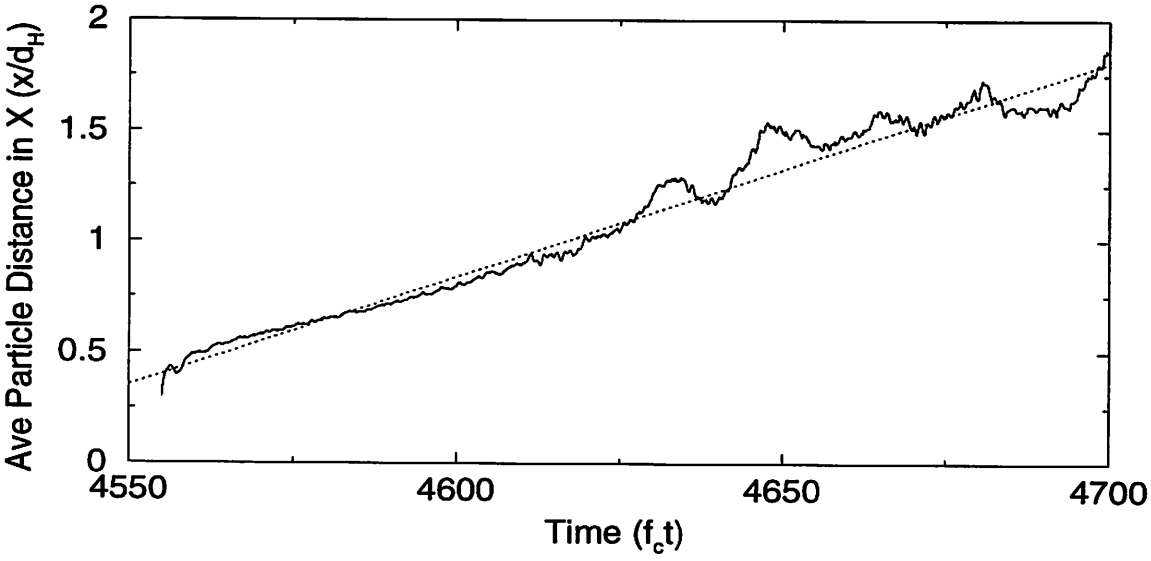

Figure 3.9: The average distance of the electrons from the cathode.

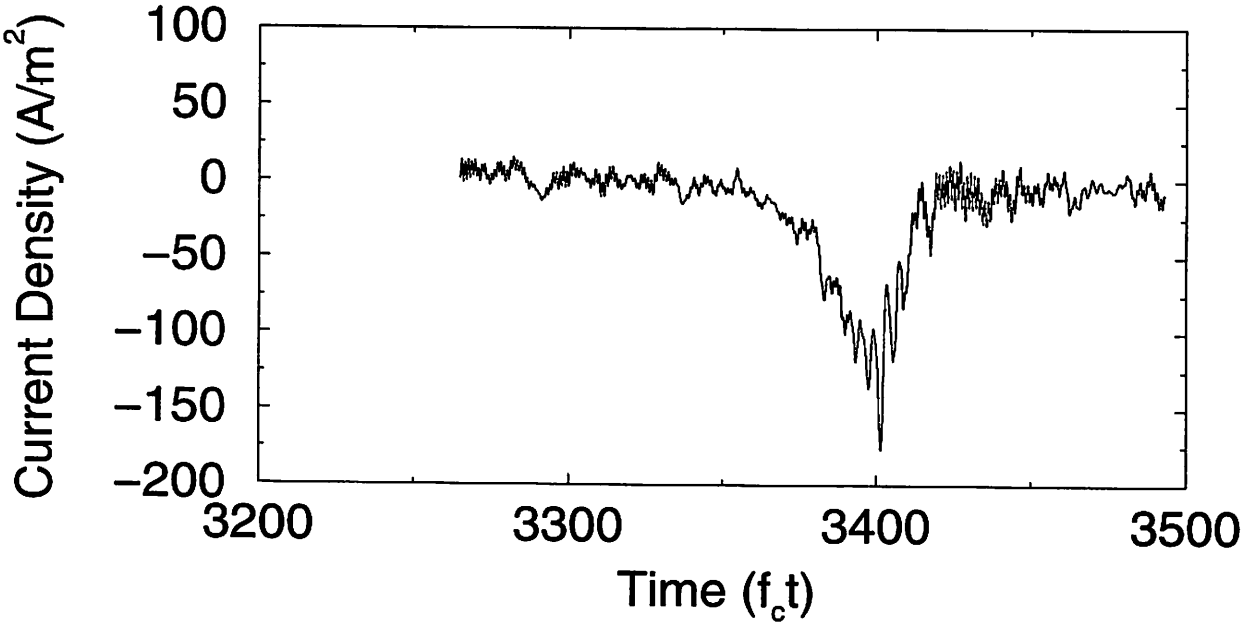

Figure 3.10: The current collect by the anode as a function of time.

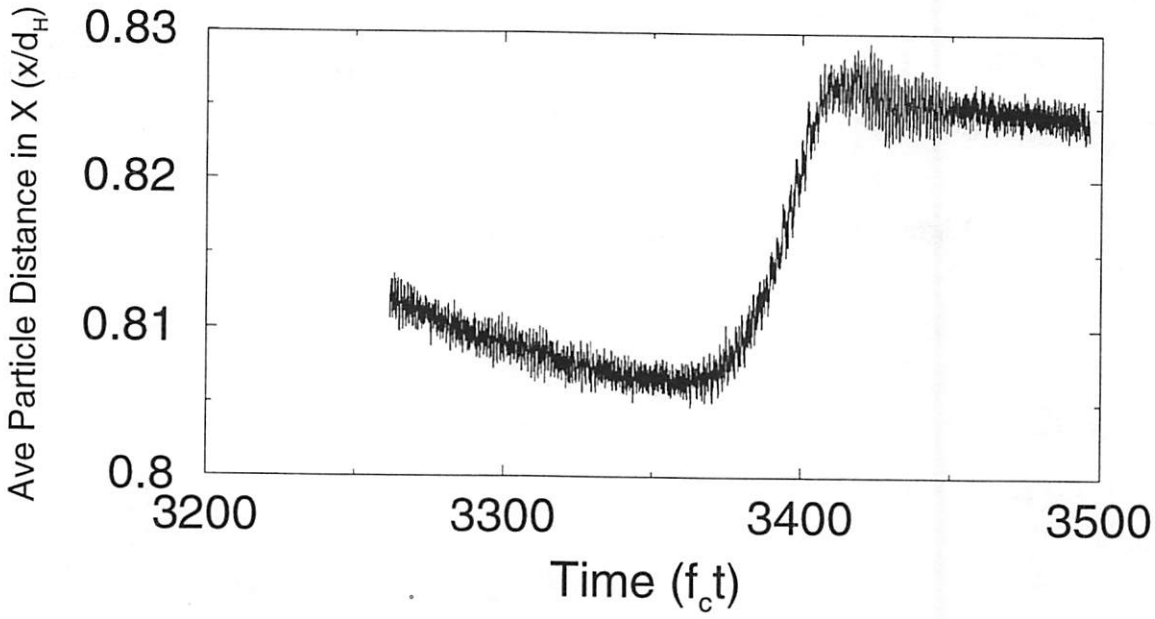

Figure 3.11: The average distance of the electrons from the cathode during a current spike.

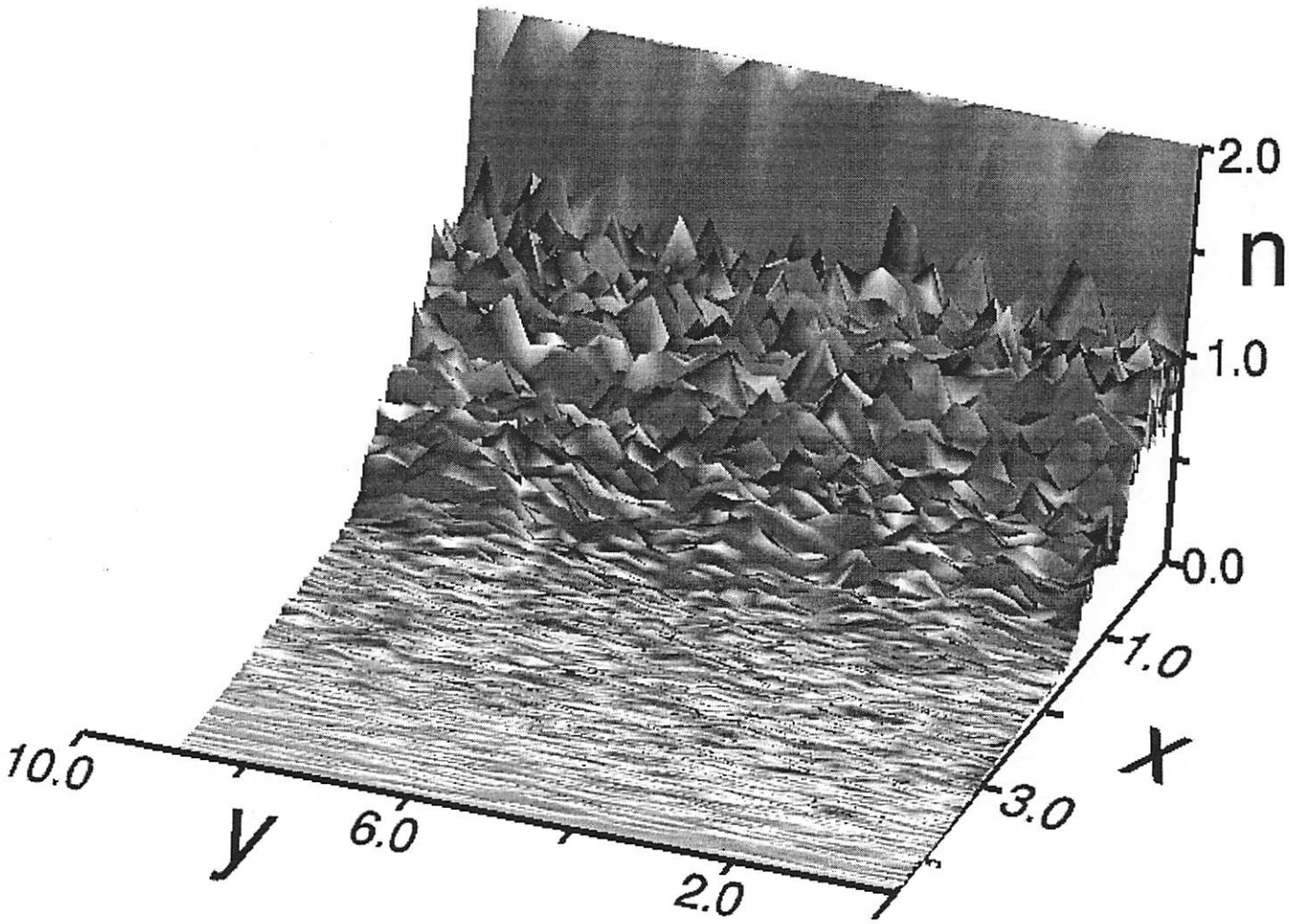

Figure 3.12: The density in the crossed-field diode after a current spike was collected showing the density with no spoke.

Chapter 4

Loading and Injection of Maxwellian Distributions in Particle Simulations

Submitted to Journal of Computational Physics

4.1 Introduction

We first observed injection difficulties when detailed comparisons were made between 1d and 2d diodes [118, 119, 120] when using common particle loading and injection algorithms. The phase space plots (position-velocity; Fig. 4.1) showed incorrect velocities with small gaps (incorrect position) in emission. The culprit was initiating the leap-frog integrator with velocity, $\mathbf{v}$ and position, $\mathbf{x}$ at the same time; $\mathbf{v}$ and $\mathbf{x}$ should be $\Delta t/2$ apart in time, in order to obtain second-order accuracy. The result of not time-centering the velocity and position correctly was a zero-order error in each emitted particle.

For some models, this error might have a small or unnoticeable effect on the simulation. However, in models we were (and are) studying for noise and stability in cross field devices, these errors were unacceptable. Hence, the choice was to devise a second-order accurate method to start the leap-frog integrator.

The initial conditions of the particle distribution function, $f(\mathbf{x}, \mathbf{v}, t = 0)$, where $\mathbf{x}$, $\mathbf{v}$, and t are the position, velocity, and time respectively, are important in determining the later behavior of the system, especially for the study of transients or instabilities. The distribution function continues to be important for simulations with collisions using Monte Carlo Collision (MCC) packages, but the emphasis here is long time (longer than an ion transit time) scale developments. The boundary condition of the particle distribution, $f(\mathbf{x} = wall, \mathbf{v}, t)$, (for example, thermionic, field or secondary emission) which may be a function of time, is also important in determining the continuing behavior of the system. These considerations are especially important for modeling diodes[121], electron guns[122],

crossed–field emission[121, 123, 124], multipactor breakdown[125], and any time particle emission is near the space charge limit[117]. Incorrect loading and injection can often manifest itself in non-obvious ways, such as larger than expected field fluctuations; this will be discussed in detail later.

Chapter 16 of Birdsall and Langdon [46] discusses some methods in wide use for inverting densities n(x) and f(v) as well as the particle flux, $\Gamma = \mathbf{v}_\perp f(\mathbf{x} = wall, \mathbf{v}, t)$, where $\mathbf{v}_\perp$ is the velocity perpendicular to the wall. Although these boundary conditions are required for many bounded PIC codes, a comprehensive accuracy or error analysis has not appeared in the literature. The purpose of this paper is to expand upon the commonly used injection and loading schemes, adding an analysis of the accuracy of a number of techniques. This paper discusses techniques for converting model distributions (stated with x and v given at the same time) into x and v suitable for the common second-order accurate leap-frog integrator (with x and v half a time step, $\Delta t/2$, apart).

The organization of this paper is as follows. First, we will discuss and define cumulative distribution and scalings used in this paper. Second, we will review the inversion of Maxwellian distributions and fluxes with the addition of refinements to improve numerical accuracy and efficacy. Lastly, we will discuss several new methods for time-centering particles injected from the edge of the simulation and compare the results of these new methods in a crossed-field diode.

4.1.1 Motivation

In order to demonstrate the error, we present highlights of injection in a magnetized crossed-field diode, previously simulated and published by Verboncoeur and Birdsall [121] using the particle-in-cell (PIC) code XPDP1 (X-Window Plasma Device Planar One-Dimensional) [49]. A diagram of the diode is shown in Fig. 4.6, and the physical and numerical parameters are summarized in Table 4.2; the complete behavior is given in Section 4.3.4. The theory for this diode was derived by Lau et al.[126].

Compared to the theoretical predictions, XPDP1 version 3.1 (which used the old initial advance for x and v), obtains a small 0.2 percent error in the critical current, and a large 64 percent error in the cathode electric field, and surface charge. Using the second-order initial step presented in this paper, with the same numerical parameters, results in a less than 3×10^{-5} percent error in the critical current, and a 4 percent error in the expected cathode electric field. These errors also illustrate that not all parameters in a simulation are affected equally by the initial push. The critical current is insensitive to the initial push while the surface field was sensitive.

Phase space near the cathode, when the simulation is in equilibrium, is shown for both old (zeroth-order) and new (second-order) initial step algorithms in Fig. 4.1. The phase space shows the results of using the more accurate injection push; first, it removes the incorrect spacing of particles in the successive time steps. Second, the correct positions of the particles produces a space charge different than the incorrect injection; thus, the electric

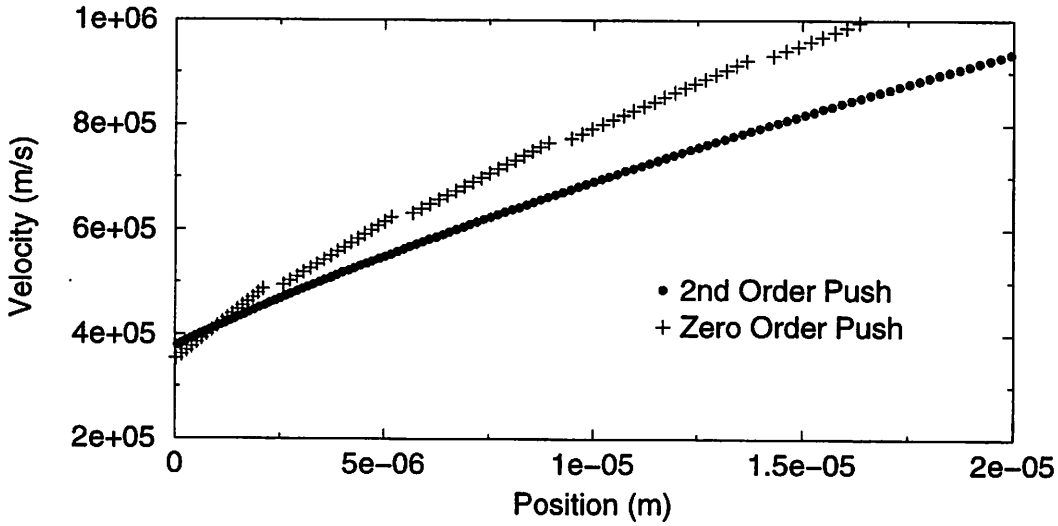

Figure 4.1: The particle phase space near the cathode emitter in equilibrium with the critical current injected for the zero-order injection model and the new second-order accuracy injection method.

field that was used in the second-order injection method is different from that produced by the zero-order injection. These changes in the equilibrium state agree better with theory [126].

4.1.2 Background

In the literature, papers that discuss particle injection and loading are usually focused on reducing macro-particle induced noise in PIC simulations by careful ordering of the particles in position and velocity space, called a *quiet start*. These ordering methods are first attributed to J. A. Byers (1970) [127] and discussed and reviewed in 1980 by Denavit and Kruer [128]. While quiet starts are not the main focus of this paper they are applicable to the inversion algorithms presented here. Quiet starts are most useful in transient or instability growth simulations when low initial noise levels are important. Indeed, the intent of a quiet start is to postpone the development of thermal fluctuations in a simulation; it can not prevent them. The following is a brief literature review of the different methods proposed for reducing the injection and loading noise in a PIC simulation.

In 1971, Morse and Nielson [129] re-adjusted randomly picked velocities so that the first moment (momentum) in each cell was equal to that of the initial distribution function. This technique was expanded upon by Gitomer in the same year [130] so that both the first and second (energy) moments were correct. These methods yield a small reduction of noise but do not have the published numerical problems of the the following schemes.

In 1972, Denavit [131] used a hybrid PIC model and numerical solutions of the

Vlasov equation in order to reduce noise in phase space. The distribution function is reconstructed periodically, as in Vlasov solutions, by a local averaging operation in phase space. This distribution function is inverted to obtain particle velocities using the variable weights. The analysis of this variable weighting method was later published by Gitomer and Adams [132].

Gitomer and Adams [132] discussed two methods; one assigned the velocities in an ordered manner and another varied the particles weights. The first method, ordered velocity initialization, can give rise to a multi-beam instability, which was predicted by Dawson [133]. The second method, variable particle weights, leads to a multi-beam instability [132], and was later found to have a non-physical heat exchange between the particles of different numerical weight [134]. Both of these methods are still useful because these non-physical (numerical) problems are significant only in certain parameter regimes, which are discussed in the articles.

In 1988 Lawson [135] modified the ordered velocity sequencing of Gitomer and Adams [132] for flux injection, but cooling occurs due to the particles becoming disordered, giving up energy to the electric field fluctuations.

Inverting a velocity distribution requires an understanding of the ramifications of using macro-particles. Denavit [136] discusses the effect of discrete particles and discrete particle position and velocity loading, for electrostatic and Darwin (magneto-inductive) field solves. For simulations that reach a steady state, an understanding of the effects of discrete particles and fluctuations is important because quiet starts do not reduce the fluctuations in steady state. Matsuda and Okuda [137] studied numerically and analytically the discrete particle effect on drag and diffusion of particles in velocity space. Loading and injection are mentioned briefly in these papers.

4.1.3 Cumulative distribution functions

The cumulative distribution function maps the distribution function variable (e.g., velocity) to a uniformly distributed set of numbers, R, typically normalized between 0 and 1. The cumulative distribution, $F(v)$ is:

$$R = F(v) \equiv \frac{\int_{v_{cl}}^{v} f(v)dv}{\int_{v_{cl}}^{v_{cu}} f(v)dv}, \tag{4.1}$$

where v_{cl} and v_{cu} are the lower and upper cutoffs, respectively. The method of choosing R in the cumulative distribution function may affect the results of a simulation (See Appendix A). The cumulative distribution function will be inverted analytically whenever possible and where it is not, it will be numerically. The numerical inversion consists of making a second-order table and then interpolating the cumulative distribution function between table values. The whole process is second-order accurate in table value spacing.

4.1.4 Definitions and Scaling

Due to the ubiquity of the Maxwellian-Boltzmann velocity distribution, emphasis has been on loading Maxwellian distributions and injecting Maxwellian fluxes. The methods presented here are also applicable to any separable continuous distribution function, $f(v_x)f(v_y)f(v_z)$, with continuous and finite first and second derivatives. The Maxwell-Boltzmann distribution is given by:

$$f(E) \propto \exp\left(\frac{-E}{kT}\right), \tag{4.2}$$

where k is Boltzmann's constant, E is the kinetic energy and T is the temperature .

A non–relativistic anisotropic Maxwellian distribution can be broken into three separate one-dimensional distributions and then inverted independently; this separation is properly exploited whenever practicable in this paper. For this work, the definition of the $i\,th$ component of thermal velocity, v_{ti}, is taken to be,

$$\frac{1}{2}mv_{ti}^2 = \frac{1}{2}kT_i. \tag{4.3}$$

The thermal velocity of an isotropic Maxwellian is given by:

$$\frac{1}{2}mv_t^2 = \frac{3}{2}kT, \text{ with } v_t^2 = \sum_{i=1}^{3} v_{ti}^2. \tag{4.4}$$

Using the 1d definitions (Eq. 4.3) a Maxwellian distribution is defined as:

$$f(v) \propto e^{-\frac{v^2}{2v_{ti}^2}}. \tag{4.5}$$

With these definitions the standard deviation of the distribution is v_{ti}. The velocities in this paper are normalized by $v_{ti}\sqrt{2}$ (the normalized velocity is equal to $v/(v_{ti}\sqrt{2})$), in order to simplify the equations, unless otherwise noted.

4.2 Loading a Maxwellian Velocity Distribution

The cumulative distribution function for a Maxwellian with both an upper, v_{cu}, and lower, v_{cl}, velocity cutoff in one dimension is:

$$F(v) = R = \frac{\int_{v_{cl}}^{v} e^{-v^2}dv}{\int_{v_{cl}}^{v_{cu}} e^{-v^2}dv} = \frac{\mathrm{Erf}(v) - \mathrm{Erf}(v_{cl})}{\mathrm{Erf}(v_{cu}) - \mathrm{Erf}(v_{cl})}, \tag{4.6}$$

where Erf is the error function. Solving for v:

$$v = \mathrm{Erf}^{-1}(R\,\mathrm{Erf}(v_{cu}) + (1-R)\mathrm{Erf}(v_{cl})). \tag{4.7}$$

With present day digital computers it is faster to tabulate Eq. 4.6 and then interpolate within the table than to calculate Eq. 4.7 for each particle. Effective tabulation (numerical root finding) and interpolation techniques using the attributes of cumulative distributions are presented in Appendix B.

A Maxwellian distribution can also be inverted using the Box-Muller method [138] and is presented here because it is easily modified for upper cutoff Maxwellian distributions. This method transforms a uniformly distributed pseudo-random number to a Maxwellian distribution. First, pick two pseudo-random numbers, ν_1 and ν_2, with $0 < \nu_1, \nu_2 \leq 1$. Because of the requirement that ν_1 and ν_2 be uncorrelated, this method is not well suited for use with sub-random sequences. The sum of the squares, $R^2 = \nu_1^2 + \nu_2^2$, is formed. If $R^2 > 1$, then reject ν_1 and ν_2, otherwise accept them. The Box-Muller transformation returns two normal deviates,

$$v_1 = \nu_1 \sqrt{-\frac{\ln(R^2)}{R^2}}, \text{ and } v_2 = \nu_2 \sqrt{-\frac{\ln(R^2)}{R^2}}. \tag{4.8}$$

This is equivalent to inverting $vf(v)$ (see Section 4.3) and then randomly choosing an angle to obtain two velocities. To show that this is the correct transformation between uniform deviates and the distribution function, take the determinant of the Jacobian of the transformation:

$$\frac{\partial(\nu_1, \nu_2)}{\partial(v_1, v_2)} = \begin{vmatrix} \frac{\partial \nu_1}{\partial v_1} & \frac{\partial \nu_1}{\partial v_2} \\ \frac{\partial \nu_2}{\partial v_1} & \frac{\partial \nu_2}{\partial v_2} \end{vmatrix}. \tag{4.9}$$

If the Jacobian is a product of a function of v_1 and v_2 alone, then each velocity is independently distributed according to each function in the product. The Jacobian for the Box-Muller transform, Eq. 4.8, is

$$\frac{\partial(\nu_1, \nu_2)}{\partial(v_1, v_2)} = -\exp(-v_1^2)\exp(-v_2^2). \tag{4.10}$$

The domain of the pseudo-random number can be scaled so that that it transforms to a cutoff Maxwellian distribution. Since the Box-Muller transformation is equivalent to inverting $vf(v)$ and then randomly choosing an angle (Section 4.3), it can be solved for v with an upper cutoff and then an angle can be chosen at random to obtain two velocities. Let $R_{cu} = e^{v_{cu}^2}$, where v_{cu} is the upper velocity cutoff. The transformation for an upper cutoff Maxwellian is:

$$\begin{aligned} v_1 &= \frac{\nu_1}{R}\sqrt{v_{cu}^2 - \ln\left(R^2 + (1-R^2)\,R_{cu}\right)}, \text{ and} \\ v_2 &= \frac{\nu_2}{R}\sqrt{v_{cu}^2 - \ln\left(R^2 + (1-R^2)\,R_{cu}\right)}. \end{aligned} \tag{4.11}$$

This method is not easily expanded for a lower cutoff; hence, the transformation for a lower cutoff must be done numerically.

When the desired distribution is a Maxwellian with a non-relativistic drift component, the drift, $\mathbf{v}_0$, can be added linearly, $\mathbf{v}' = \mathbf{v}_0 + \mathbf{v}$. For the relativistic case, the addition is nonlinear; see, for example, Smith [139] page 117. For this section only, $v_{\|}$ and $\mathbf{v}_{\perp}$ are

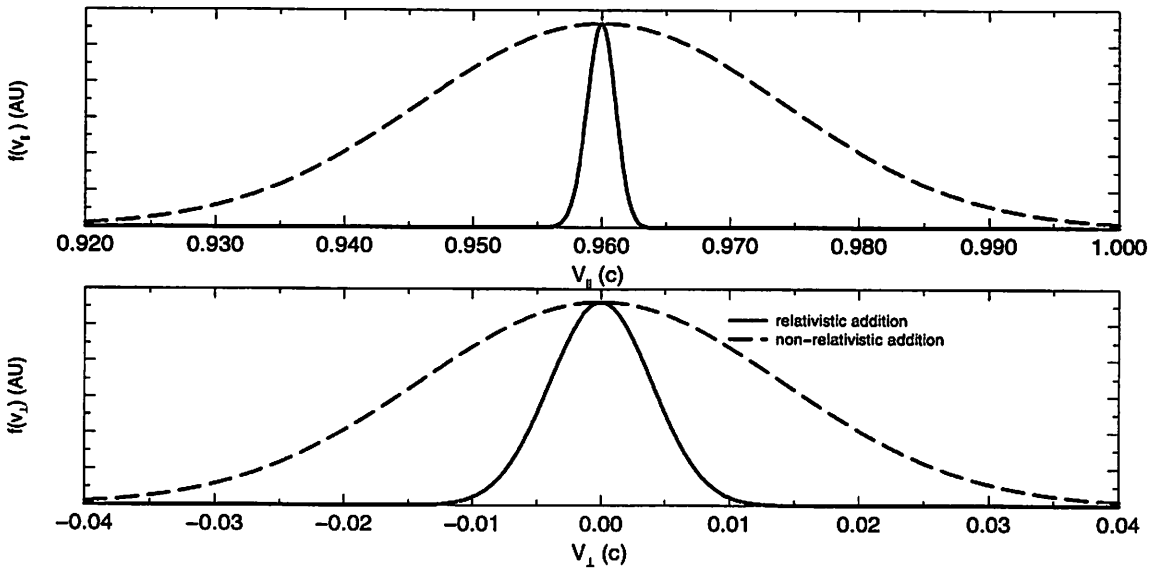

Figure 4.2: Comparing the effect of relativistic and non–relativistic velocity addition on a Maxwellian distribution with $v_0 = 0.96c$ and $v_t = 0.02c$. The relativistic velocity addition shows different cooling in the velocity components parallel and perpendicular to the drift, whereas the non–relativistic velocity addition does not cool.

the velocity parallel and perpendicular to the relativistic drift respectively. The relativistic transformation for the parallel velocity is

$$v'_{\|} = \frac{v_{\|} + v_0}{1 + v_0 v_{\|}/c^2}, \tag{4.12}$$

and the transformation for the perpendicular velocity is

$$\mathbf{v}'_{\perp} = \frac{\mathbf{v}_{\perp}}{\gamma(1 + v_0 v_{\|}/c^2)}. \tag{4.13}$$

Here

$$\gamma = \frac{1}{\sqrt{1 - v_0^2/c^2}}, \tag{4.14}$$

c is the speed of light, v_0 is the magnitude of the drift, and the velocities are not normalized. A drifting Maxwellian distribution is appropriate if the beam has had time to thermalize in the rest frame of the beam due to, for example, Coulomb collisions. The relativistic velocity addition causes the thermal velocity components parallel and perpendicular to the drift to cool, as shown in Fig. 4.2, compared to a non–relativistic velocity addition.

4.2.1 Time-Centering of Loaded Particles

Many PIC codes use a leap–frog integrator in order to integrate the equations of motion for the particles. In the leap-frog algorithm, the velocities and positions are offset

by half a time step, often called time-centering. In Sec. 2-7 of Birdsall and Langdon [46] a second-order method for time-centering particles at $t = 0$ is presented for uniform plasma with the electron having an initial position of the form $x_i(t = 0) = x_{i0} + x_{i1}cos(k_s x_{i0})$ with zero velocity; $x_{i1}cos(k_s x_{i0})$ is a perturbation of equally spaced positions (x_{i0}). This method is first-order for when $da/dt \neq 0$, or when $\mathbf{B} \neq 0$, or when, $\mathbf{v}_0 \neq 0$, as shown below. This section will present a generalized second-order method for time-centering particles. In this paper the velocities have been arbitrarily (but computationally efficient) chosen to lag the positions at the end of a time step. Time-centering will also be discussed for particle injection in Sec. 4.3.1, applying the same formalism.

To formulate a numerical PIC injection or loading method, one can begin with the Lorentz equation of motion,

$$m\ddot{\mathbf{x}}(t) = q\mathbf{E}(\mathbf{x}(t), t) + q\mathbf{v}(t) \times \mathbf{B}(\mathbf{x}(t), t), \tag{4.15}$$

which can be rewritten as,

$$\ddot{\mathbf{x}}(t) = \mathbf{e}(\mathbf{x}(t), t) + \Omega(\mathbf{x}(t), t)\mathbf{v}(t) \times \hat{\mathbf{b}}(\mathbf{x}(t), t), \tag{4.16}$$

where $\mathbf{e} = q\mathbf{E}/m$, $\Omega = q|\mathbf{B}|/m$, and $\hat{\mathbf{b}} = \mathbf{B}/|\mathbf{B}|$. Continuous quantities will be denoted by (), e.g., $\mathbf{E}(t)$ is the electric field as a continuous function of time.

Before discussing the half-step needed for loading, a review of the standard leap-frog integrator with the magnetic term centered by averaging [46] is presented:

$$\begin{aligned} \mathbf{x}_{n+1} - \mathbf{x}_n &= \mathbf{v}_{n+1/2}\Delta t, \text{ and} \\ \mathbf{v}_{n+1/2} - \mathbf{v}_{n-1/2} &= \mathbf{e}_n\Delta t + \tan(\Omega_n\Delta t/2)(\mathbf{v}_{n-1/2} + \mathbf{v}_{n+1/2}) \times \hat{\mathbf{b}}_n, \end{aligned} \tag{4.17}$$

where n indicates the time after n time steps, $t_n = n\Delta t$. Loading is usually done at $t = 0$ ($n = 0$), but to maintain generality so that we can use these results for injecting particles from a boundary (Sec. 4.3.1) we will center particles at time t_n (time step n). Discrete quantities are denoted by subscripts, e.g., $\mathbf{E}_n$ is the electric field at time step n. To find the order of accuracy these equations may be combined and Taylor expanded around t_n. The acceleration truncation error, $\mathcal{E}$, will be defined as the continuous acceleration equation, Eq. 4.16, minus the discrete acceleration equation, Eq. 4.17, at time, t_n:

$$\begin{aligned} \mathcal{E} = \ddot{\mathbf{x}}(t_n) - \Big(\mathbf{e}(\mathbf{x}(t_n), t_n) + \Omega(\mathbf{x}(t_n), t_n)\mathbf{v}(t_n) \times \hat{\mathbf{b}}(\mathbf{x}(t_n), t_n)\Big) \\ - \Big(\tfrac{\mathbf{x}_{n+1} - 2\mathbf{x}_n + \mathbf{x}_{n-1}}{\Delta t^2} - (\mathbf{e}_n + \tfrac{\tan(\Omega_n\Delta t/2)(\mathbf{x}_{n+1} - \mathbf{x}_{n-1}) \times \hat{\mathbf{b}}_n}{\Delta t^2})\Big). \end{aligned} \tag{4.18}$$

Assuming that the discrete and continuous fields agree at integer time steps, the error may be simplified at the $n\,th$ time step to:

$$\mathcal{E} = \ddot{\mathbf{x}}(t_n) - \frac{\mathbf{x}_{n+1} - 2\mathbf{x}_n + \mathbf{x}_{n-1}}{\Delta t^2} + \left(\frac{\tan(\Omega_n\Delta t/2)(\mathbf{x}_{n+1} - \mathbf{x}_{n-1})}{\Delta t^2} - \Omega(\mathbf{x}(t_n), t_n)\dot{\mathbf{x}}(t_n)\right) \times \hat{\mathbf{b}}_n. \tag{4.19}$$

Taylor expanding in time around t_n and explicitly writing the second-order error term, we obtain:

$$\mathcal{E} = -\frac{1}{12}\left[d_{tttt}\mathbf{x}(t) - \Omega(\mathbf{x}(t),t)\left(\Omega^2(\mathbf{x}(t),t)\dot{\mathbf{x}}(t) + 2d_{ttt}\mathbf{x}(t)\right) \times \hat{\mathbf{b}}_n\right]\Delta t^2 + \mathcal{O}(\Delta t^4), \tag{4.20}$$

where $d_{t\times n}$ is shorthand for $(d/dt)^n$ and $\mathcal{O}(\Delta t^n)$ is a vector where the lowest order component is order n. Eq. 4.20 shows that the leap-frog integration is globally second-order accurate. From Eq. 4.20 and the velocity update of Eq. 4.17 one might expect that the velocity would have a local truncation error of $\mathcal{O}(\Delta t^3)$; however, the velocity is only $\mathcal{O}(\Delta t^2)$. As shown here by Taylor expanding the position update of Eq. 4.17 and showing the second-order term explicitly:

$$\mathbf{v}_{n+1/2} = \frac{\mathbf{x}_{n+1} - \mathbf{x}_n}{\Delta t} = \mathbf{v}((n+1/2)\Delta t) + \frac{1}{24}d_{ttt}\mathbf{x}(t_n)\Delta t^2 + \mathcal{O}(\Delta t^3). \tag{4.21}$$

It will be shown that the second-order loading (and later the injection) method will have the same $\mathcal{O}(\Delta t^2)$ local truncation error as shown in Eq. 4.21. The position, as expected, has a local truncation of $\mathcal{O}(\Delta t^4)$, which can be shown from Eq. 4.20 and Eq. 4.17. It would be incorrect to assume that a fourth-order position injection and any second-order velocity injection would comprise a second-order global method. In this case, the second-order error in Eq. 4.21 cancels when it is differenced with $\mathbf{v}_{n-1/2}$ to form the acceleration:

$$\begin{aligned}\mathbf{a}_n &= \frac{\mathbf{v}_{n+1/2}-\mathbf{v}_{n-1/2}}{\Delta t} \\ &= \frac{\mathbf{v}((n+1/2)\Delta t)+\frac{1}{24}d_{ttt}\mathbf{x}(t_n)\Delta t^2+\mathcal{O}(\Delta t^3)-(\mathbf{v}((n-1/2)\Delta t)+\frac{1}{24}d_{ttt}\mathbf{x}(t_n)\Delta t^2+\mathcal{O}(\Delta t^3))}{\Delta t} \\ &= \frac{\mathbf{v}((n+1/2)\Delta t)-\mathbf{v}((n-1/2)\Delta t)}{\Delta t} + \mathcal{O}(\Delta t^2).\end{aligned} \tag{4.22}$$

This shows how the second-order truncation error in velocity cancels when combined to form the acceleration. This seemly trivial cancellation is the essence of the difficulty in forming a second-order truncation error.

The proper way to obtain the truncation error of a loading or injection method is to substitute the position and velocity into Eq. 4.19, the leap-frog error equation:

$$\begin{aligned}\mathcal{E} = \ddot{\mathbf{x}}(t_n) &- \frac{\mathbf{x}_{n+1}-\mathbf{x}_n-\mathbf{v}_{n-1/2}\Delta t}{\Delta t^2} \\ &+ \left(\frac{\tan(\Omega_n\Delta t/2)(\mathbf{x}_{n+1}-\mathbf{x}_n+\mathbf{v}_{n-1/2}\Delta t)}{\Delta t^2} - \Omega(\mathbf{x}(t_n),t_n)\dot{\mathbf{x}}(t_n)\right)\times\hat{\mathbf{b}}_n.\end{aligned} \tag{4.23}$$

Here $\mathbf{x}_n$ is the position at time step n and $\mathbf{v}_{n-\frac{1}{2}}$ is the velocity at time step $n-\frac{1}{2}$, the first position and velocity after time-centering. For Eq. 4.23 to be second-order, the local truncation error in position of the time-centered particle, $\mathbf{x}_n$, must be at least fourth-order, as in standard leap-frog. It is important that the position have the same truncation error as leap-frog because the particle position, x_n, is used in the field solve at time step n. For Eq. 4.23 to be second-order accurate, the velocity of the time-centered particle, $\mathbf{v}_{n-1/2}$, must have the same second-order local truncation error as leap-frog (Eq. 4.21) because the truncation error cancels as the particle integrator advances (Eq. 4.22). Also, it is necessary

to have the velocity error second-order, in order to have accurate current collection for an electromagnetic field solve. In the analysis of the following methods the truncation error will be kept through second-order in the Lorentz equation error (Eq. 4.23) and third-order in $\mathbf{v}_{n-1/2}$.

We will analyze two loading methods. First the loading methods presented in Birdsall and Langdon[46] with an added magnetic field. The second method is a second-order method for general time-dependent fields.

Half Time Step Push for Particle Loading

First we will analyze the method of time-centering presented in Sec. 2-7 of Birdsall and Langdon[46] in which the velocity is pushed back a half-step. This method may written in the form,

$$\mathbf{v}_{n-1/2} - \mathbf{v}_n = -\mathbf{e}\frac{\Delta t}{2} - \tan(\Omega\Delta t/4)(\mathbf{v}_{n-1/2} + \mathbf{v}_n) \times \hat{\mathbf{b}}. \tag{4.24}$$

Substituting Eq. 4.24 into the truncation error equation, Eq. 4.23, then Taylor expanding and applying the chain rule we obtain a first-order accurate method for general time-dependent fields. Due to the complexity and length of the analytic expression for the truncation error for this method with time-dependent fields, the expression is not shown here. The local truncation error for the half-step velocity, $\mathcal{E}_v$, is second-order.

The above method is first order in general, however, it is second-order under limited conditions. For an illustration of when this method is second-order we will choose the magnetic field to be zero, then the truncation error of the above method can be written as

$$\mathcal{E} = -\frac{1}{6}\left(\mathbf{v}(t_n) \cdot \nabla\mathbf{e}(t_n) + \frac{\partial \mathbf{e}(t_n)}{\partial t}\right)\Delta t + \mathcal{O}(\Delta t^2). \tag{4.25}$$

This truncation error (Eq. 4.25) will be second-order if the velocity ($\mathbf{v}(t_n)$) or $\nabla\mathbf{e}(t_n)$ is zero or $\nabla\mathbf{e}(t_n)$ is perpendicular to $\mathbf{v}(t_n)$ and the derivative of the electric field in time is zero. These assumptions are true for for the loading of the perturbation in Birdsall and Langdon (Sec. 2-7) thus their loading scheme is second-order accurate for that special case. The velocity error for zero magnetic field is

$$\mathcal{E}_v = \mathbf{v}((n-1/2)\Delta t) - \mathbf{v}_{n-1/2} = -\frac{1}{24}d_{ttt}\mathbf{x}(t_n)\Delta t^2 - \frac{1}{6}\left(\mathbf{v}(t_n) \cdot \nabla\mathbf{e}(t_n) + \frac{\partial \mathbf{e}(t_n)}{\partial t}\right)\Delta t^2. \tag{4.26}$$

Comparing Eq. 4.26 with the error in the leap-frog velocity, Eq. 4.21, we see the second term on the right does not cancel, leaving the velocity with a second order local error term, which is globally first order in the general case (per Eq. 4.25).

General Second Order Time-Centering for Particle Loading

The particle injection method discussed later (Sec. 4.3.1) is a generalization of a second-order loading method where all the particle velocities and positions are known at

time t_n. (The injection method shown later is for particles that are injected at an arbitrary time between time steps.) To save space we will not derive the specific results here and the more general results later, but simplify the more general results from Sec. 4.3.1. For the second-order injection method past time step field values are used. However, for the loading previous field values are not available; instead the time derivative of the fields must be given as an initial condition to at least first-order. Therefore, the fields needed for the half step push (a simplification of Eq. 4.52, with $f = 0$ and the time index on the fields shifted from $n-1$ to n) are

$$\begin{aligned} \Omega_v &= \Omega(\mathbf{x}_n, n) - \tfrac{3}{4}\tfrac{\partial \Omega(\mathbf{x}_n,n)}{\partial t}\Delta t - \tfrac{1}{4}\mathbf{v}_n \cdot \nabla\Omega(\mathbf{x}_n, n)\Delta t, \\ \hat{\mathbf{b}}_v &= \hat{\mathbf{b}}(\mathbf{x}_n, n) - \tfrac{3}{4}\tfrac{\hat{\mathbf{b}}(\mathbf{x}_n,n)}{\partial t}\Delta t - \tfrac{1}{4}\mathbf{v}_n \cdot \nabla\hat{\mathbf{b}}(\mathbf{x}_n, n), \\ \mathbf{e}_v &= \mathbf{e}(\mathbf{x}_n, n) - \tfrac{3}{4}\tfrac{\mathbf{e}(\mathbf{x}_n,n)}{\partial t}\Delta t - \tfrac{1}{4}\mathbf{v}_n \cdot \nabla\mathbf{e}(\mathbf{x}_n, n)\Delta t. \end{aligned} \tag{4.27}$$

The velocity half-step for the load (a simplification of Eq. 4.54) is

$$\begin{aligned} \mathbf{v}' - \mathbf{v}_n &= -\tfrac{1}{2}\mathbf{e}_v\Delta t - \tan(\Omega_v\Delta t/4)(\mathbf{v}' + \mathbf{v}_n) \times \hat{\mathbf{b}}_v, \\ \mathbf{v}_{n-1/2} - \mathbf{v}' &= \tfrac{\Delta t^2}{24}\Big(\mathbf{e} \times \hat{\mathbf{b}}\Omega/\Delta t + (\hat{\mathbf{b}}(\hat{\mathbf{b}} \cdot \mathbf{v}_n) - \mathbf{v}_n)\Omega^2 \\ &\quad + \mathbf{v}_n \cdot \Big(\nabla\mathbf{e} + (\nabla\Omega\mathbf{v}_n) \times \hat{\mathbf{b}} + \Omega\mathbf{v}_n \times \nabla\hat{\mathbf{b}}\Big) \\ &\quad + \tfrac{\partial \mathbf{e}(\mathbf{x}_n,n)}{\partial t} + \Omega\mathbf{v}_n \times \tfrac{\partial \hat{\mathbf{b}}(\mathbf{x}_n,n)}{\partial t} + \tfrac{\partial \Omega(\mathbf{x}_n,n)}{\partial t}\mathbf{v}_n \times \hat{\mathbf{b}}\Big). \end{aligned} \tag{4.28}$$

This simplified version of Eq. 4.54 is obtained because x_n does not need to changed to be time-centered and we have used the relation:

$$\mathbf{v}_n = \frac{\mathbf{v}_{n+1/2} + \mathbf{v}_{n-1/2}}{2} + \mathcal{O}(\Delta t^2). \tag{4.29}$$

The local truncation error for the half-step velocity, $\mathcal{E}_v$, has $d_{ttt}\mathbf{x}(t_n)/24$ as a second-order term, which properly cancels in the leap-frog integrator. The global error of the leap-frog integrator with this time centering is second-order.

4.3 Injection of Maxwellian Flux

The flux of a distribution is used to inject particles from a boundary in the system. This boundary may not be the physical edge of the simulation, just the computational one. Since the emission will only occur for velocities moving away from the boundary, the coordinate system is chosen so that the positive velocities are moving away from the boundary. A point that is often confused is whether a Maxwellian flux or a drifting Maxwellian flux model should be applied. The electron flux from a hot (thermionic) cathode is a non-drifting Maxwellian flux, which has an average velocity, $v_{ave} = \int_0^\infty v f(v) dv$. To model electrons that came from a Maxwellian source and were accelerated (i.e., by an electric field), a Maxwellian flux with no drift should be inverted (as inverting the distribution at the source) and then

a velocity corresponding to the acceleration should be added (relativistically by Eqs. 4.12 and 4.13 or non-relativistically); a drifting Maxwellian flux should not be used.

A drifting Maxwellian flux is used to inject a thermalized drifting plasma. The drifting plasma could be a beam that has thermalized due to Coulomb collisions, normally a long time (distance) for beams. Also it could be used when the simulation frame is moving through a resting plasma, for example, a space tether or spacecraft in the rest frame of the space tether or spacecraft. The computational boundary emitting the flux represents an infinite plasma.

The normal to the emitting surface defines the direction of the flux at the surface; the other two directions are not fluxes but distributions (as treated in Section 4.2). For example, in Fig. 4.5 the emission flux direction normal to the surface is in the x_1 direction; in the transverse directions, x_2 and x_3, the distribution is inverted (Section 4.2). The direction of the velocity of the inverted flux is normal to the wall with a magnitude denoted by v.

A Maxwellian flux without a drift at the emitting surface can be inverted in closed form, with or without cutoffs. The cumulative distribution function is

$$R' = F(v) = \frac{\int_{v_{cl}}^{v} ve^{-v^2}dv}{\int_{v_{cl}}^{v_{cu}} ve^{-v^2}dv}, \tag{4.30}$$

where R' is a uniformly distributed pseudo-random number, $0 \leq R' \leq 1$. Eq. 4.30 can be integrated and then solved for velocity,

$$v = \sqrt{v_{cl}^2 + v_{cu}^2 - \ln\left(R' \exp\left(v_{cl}^2\right) + (1 - R') \exp\left(v_{cu}^2\right)\right)}. \tag{4.31}$$

For a distribution without cutoffs, this reduces to

$$v = \sqrt{-\ln(1 - R')} = \sqrt{-\ln(R)} \tag{4.32}$$

where $R = 1 - R'$ is a uniformly distributed pseudo-random number, $0 < R \leq 1$; $R = 0$ is removed from the domain because an infinite velocity is not easily representable by a computer.

For a Maxwellian flux with a drift, the velocity cannot be written in closed form. Instead, the flux distribution must be inverted numerically. The cumulative distribution for a Maxwellian flux with drift and upper and lower cutoffs is

$$R = F(v) = \frac{\int_{v_{cl}}^{v} ve^{-(v-v_0)^2}dv}{\int_{v_{cl}}^{v_{cu}} ve^{-(v-v_0)^2}dv}. \tag{4.33}$$

This can be integrated:

$$R = F(v) = \frac{e^{(v_{cl}-v_0)^2} - e^{(v-v_0)^2} + \sqrt{\pi}\, v_0 \operatorname{Erf}(v - v_0) - \sqrt{\pi}\, v_0 \operatorname{Erf}(v_{cl} - v_0)}{e^{(v_{cl}-v_0)^2} - e^{(v_{cu}-v_0)^2} + \sqrt{\pi}\, v_0 \operatorname{Erf}(v_{cu} - v_0) - \sqrt{\pi}\, v_0 \operatorname{Erf}(v_{cl} - v_0)}. \tag{4.34}$$

For $v_{cu} \to \infty$ and $v_{cl} \to 0$,

$$R = F(v) = \frac{e^{-{v_0}^2} - e^{-(v-v_0)^2} + \sqrt{\pi}\, v_0(\mathrm{Erf}(v - v_0) + \mathrm{Erf}(v_0))}{e^{-{v_0}^2} + \sqrt{\pi}\, v_0(1 + \mathrm{Erf}(v_0))}. \tag{4.35}$$

The inversion of these equations to obtain $v = F^{-1}(f)$ must be done numerically. The details of the numerical inversion are in Appendix B. The integration for an arbitrary distribution can also be done numerically. The effects of discretizing the distribution are analyzed in Appendix C.

For a Maxwellian flux in which the drift is much larger than the thermal velocity, this method can be approximated by a drifting Maxwellian as done in Section 4.2. A drifting Maxwellian is easily inverted using the Box-Muller transform, whereas, for a drifting Maxwellian flux the inversion must be done numerically; therefore, it is advantageous to use a drifting Maxwellian wherever appropriate. Most of the error (Maxwellian flux minus drifted Maxwellian) occurs at $v_0 \pm 1/\sqrt{2}$ as shown in Fig. 4.3 with $v_0 = 1$, 3, 6, and 10. The largest positive error occurs at,

$$v_{pos} = v_0 + \frac{1 - \sqrt{1 + 2e^{2v_0^2}\pi(1 + \mathrm{Erf}(v_0))^2}}{2e^{v_0^2}\sqrt{\pi}\,(1 + \mathrm{Erf}(v_0))}, \tag{4.36}$$

and the largest negative error occurs at,

$$v_{neg} = v_0 + \frac{1 + \sqrt{1 + 2e^{2v_0^2}\pi\,(1 + \mathrm{Erf}(v_0))^2}}{2e^{v_0^2}\sqrt{\pi}\,(1 + \mathrm{Erf}(v_0))}. \tag{4.37}$$

An analytic expression for the integrated RMS (L_2 norm) error is:

$$||error||_{L_2} = \frac{a}{2(a + v_0 e^{v_0^2})}\sqrt{-8ae^{v_0^2} - 4v_0 + b(4a^2 + e^{2v_0^2})}, \tag{4.38}$$

where

$$a = \frac{1}{\sqrt{\pi}(1 + \mathrm{Erf}(v_0))} \text{ and } b = \sqrt{2\pi}(1 + \mathrm{Erf}(\sqrt{2}v_0)). \tag{4.39}$$

In the limit $v_0 \gg 1$ the $||error||_{L_2} = 1/(2\sqrt[4]{2\pi}v_0)$. The integrated RMS error is shown as a function of v_0 in Fig. 4.4. Also, a Maxwellian with a relativistic drift and non-relativistic thermal velocity may replace a drifting Maxwellian flux through the use of the relativistic velocity addition of Eqs. 4.12, 4.13, and 4.14.

4.3.1 Time-Centering Injected Particles

Time-centering of velocity, **v**, and position, **x**, when loading particles is common; however, time-centering injected particles emitted from the boundaries is not. Fig. 4.5 conveys the problem graphically. The authors have found two papers that have some discussion of time-centering at the boundaries. Lawson [140] states the need for particles to be

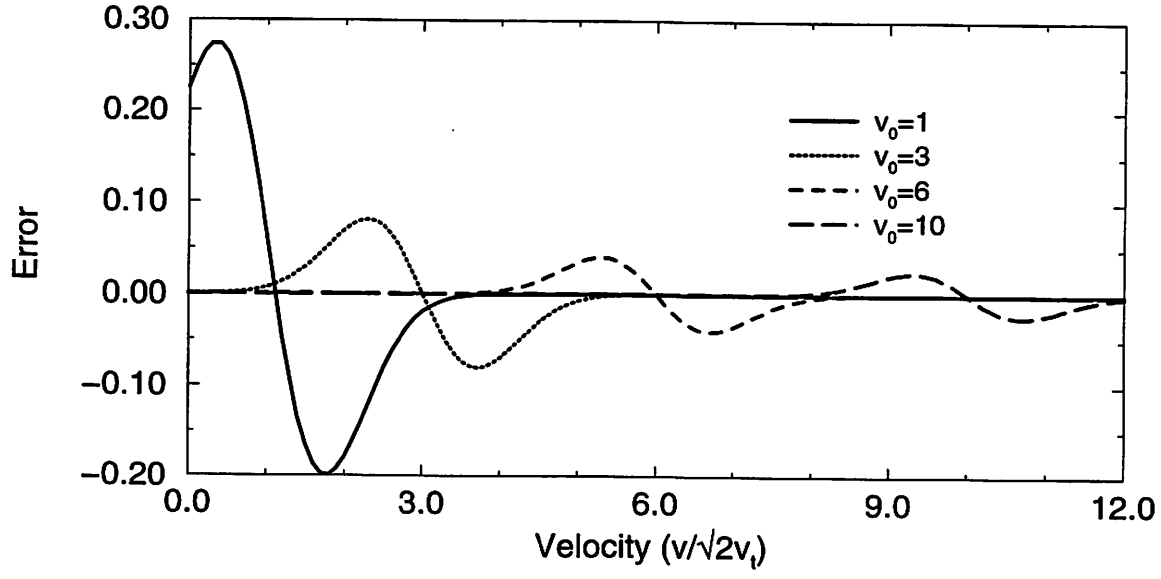

Figure 4.3: The absolute error, Maxwellian flux minus the flux of a drifting Maxwellian, as a result of using a drifting Maxwellian instead of a drifting Maxwellian flux for $v_0 = 1, 3, 6$, and 10 (v_0 normalized by $\sqrt{2}v_{ti}$).

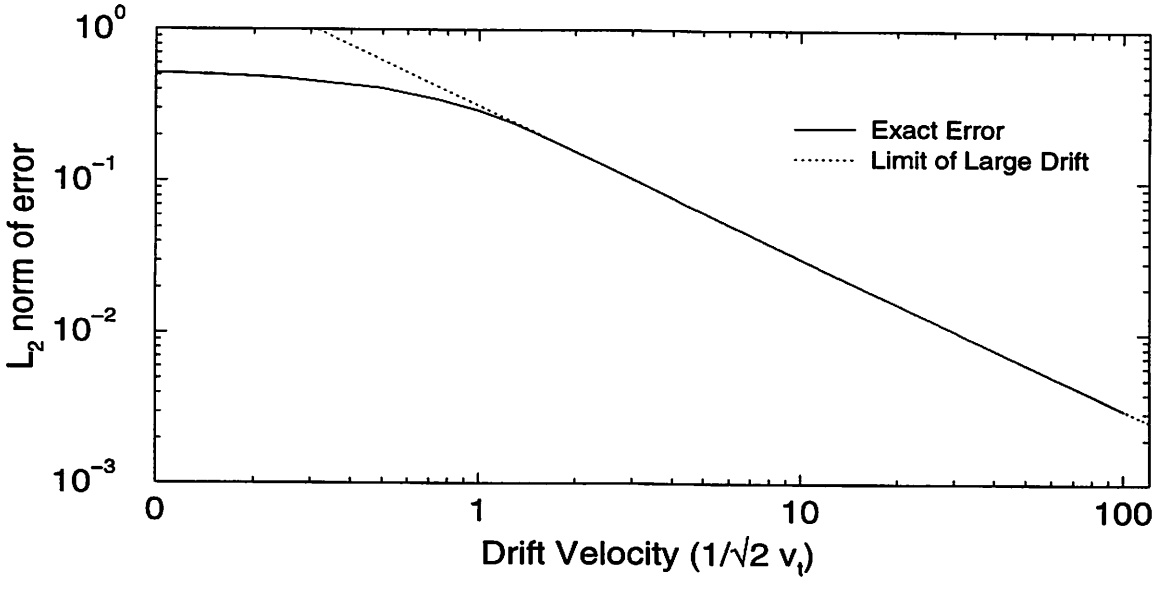

Figure 4.4: The integrated absolute error squared (L_2 norm) as a result of using a drifting Maxwellian instead of a drifting Maxwellian flux.

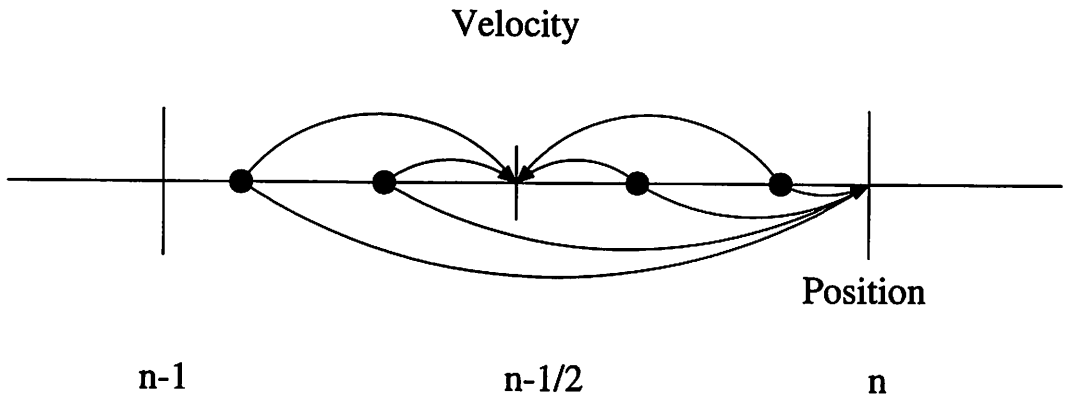

Figure 4.5: To inject a particle in a time-centered manner in the interval $(n-1)\Delta t < t \leq n\Delta t$, the particle needs to be advanced from $\mathbf{x}(t)$ and $\mathbf{v}(t)$ to $\mathbf{x}(t = n\Delta t)$ and $\mathbf{v}(t = (n - \frac{1}{2})\Delta t)$.

time-centered, but does not provide a method. Schwager and Birdsall [141] uses an energy-conserving reflection algorithm which time-centers the particle positions and velocities (due to Lawson), but is not second-order accurate. Many simulations are not sensitive to the shape of the emitted distribution function. However, it has been observed recently that in some cases, time-centering is critical, such as in cross–field diodes and virtual cathode diodes [119, 120]. Inaccurate emission of a distribution function can be thought of as changing the shape of the emitted distribution function, which varies during a time step since the error is a function of when during the time step the particle is injected. The difference between a non-time-centered distribution and a time-centered distribution is at most the change in the velocity and position (the placement of the emitter) of a leap-frog advance. In other word, if the position $(\mathbf{x}_{n-f})$ and velocity $(\mathbf{v}_{n-f})$ is used in the leap-frog advance (Eq. 4.17) as $(\mathbf{x}_n)$ and $(\mathbf{v}_{n-1/2})$ the change in position to $(\mathbf{x}_{n+1})$ and $(\mathbf{v}_{n+1/2})$ bounds the changes that any of the time-centering methods in this paper generates during the time-centering procedure. If this difference in distribution function is unimportant to the results of the simulation the accuracy of the emission can be disregarded.

In this section, a second-order accurate method is derived for particle injection at an arbitrary time with time-dependent, inhomogeneous fields. Derivation of the methods and an accuracy analysis are in Section 4.3.2. The performance (computer speed) is discussed in Section 4.3.3. Comparison to analytic test problems and a self-consistent simulation is in Section 4.3.4.

4.3.2 Injection Methods

To formulate a numerical PIC injection method, begin with the Lorentz equation of motion, Eq. 4.15, just as in the time-centering of loaded particles (Sec. 4.2.1). It will be shown that the second-order injection method will have the same $\mathcal{O}(\Delta t^2)$ local truncation error in $(\mathbf{v}_{n-1/2})$ (as shown in Eq. 4.21) so that this error cancel when the particle integrator

advances (as shown in Eq. 4.22). The position, as expected, has a local truncation of $\mathcal{O}(\Delta t^4)$, which can be shown from Eq. 4.20 and Eq. 4.17. It is incorrect to assume that a fourth-order position injection and any second-order velocity injection would comprise a second-order global method because of the cancellation shown in Eq. 4.22. The order of the injection method is obtained by substituting the injection velocity and position algorithm into Eq. 4.23. For Eq. 4.23 to be second-order, the local truncation error in position of the injected particle, $\mathbf{x}_n$, is fourth-order, as in standard leap-frog. It is important that the position have the same truncation error as leap-frog because the particle position, x_n, is used in the field solve at time step n. Also, the velocity of the injected particle, $\mathbf{v}_{n-1/2}$, must have the same second-order local truncation error as leap-frog in order to cancels the second order error of Eq. 4.21 when substituted into Eq. 4.22. It is necessary to have the velocity error second-order in order to have accurate current collection for an electromagnetic field solve. In the analysis of the following methods the truncation error will be kept through second-order in the Lorentz equation error (Eq. 4.23) fourth order in $\mathbf{x}_n$ and third-order in $\mathbf{v}_{n-1/2}$. In many applications a general second-order method is not needed because requirements are relaxed; for example, uniform fields or time-independent fields.

The five injection methods to be presented were chosen for the following reasons. The method used in the plasma device codes [49] illustrates the inaccuracy of injection when the problem was observed, which will be referred to as the 'simple' injection method . The simple Boris push with fractional time step is a simple but much improved first order method. The next three methods are second-order for special cases. The modified Boris push with fractional time step is second-order for time-independent uniform fields. The fractional Boris push with field gradients is second-order for time-independent fields. For simulation parameters near these special cases the first-order error will be small. The last method, using field values from the previous time step, is second-order for the general case. Other second-order special cases may be constructed; for example, past field values can be used with the modified Boris push if a problem has time-dependent uniform fields.

Historical analysis of simple injection method

The first method to be examined was implemented in the suite of plasma device codes from Berkeley [49] about 1988:

$$\begin{aligned} \mathbf{x}_n - \mathbf{x}_{n-f} &= \mathbf{v}_{n-f} f \Delta t, \text{ and} \\ \mathbf{v}_{n-\frac{1}{2}} - \mathbf{v}_{n-f} &= \mathbf{e}(\mathbf{x}_{n-f}, n-1)(f-\tfrac{1}{2})\Delta t. \end{aligned} \tag{4.40}$$

Here $\mathbf{x}_{n-f}$ and $\mathbf{v}_{n-f}$ are the position and velocity, respectively, at the fractional time step of injection, $n-f$, where $f = \delta t/\Delta t$, $0 \le f < 1$. The algorithm that is used to pick f makes the current as continuous as possible by injecting particles uniformly in time during a time step. Accumulated current that is a non-integer number of computer particles is carried over to the next time step. To obtain the truncation error, substitute Eq. 4.40 into

Eq. 4.23, Taylor expand around the $n\,th$ time step, and apply the chain rule:

$$\mathcal{E} = -\frac{1}{2}\left((f^2+2f-1)\Omega_n \mathbf{v}_n \times \hat{\mathbf{b}}_n + f^2 \mathbf{e}_n\right) + \mathcal{O}(\Delta t). \tag{4.41}$$

Eq. 4.41 shows that this method is a zeroth-order accurate method. The position is second-order accurate:

$$\mathcal{E}_x = x(t_n) - x_n = -\frac{1}{2} f^2 (\mathbf{e}_n + \Omega_n \mathbf{v}_n \times \hat{\mathbf{b}}_n)\Delta t^2 + \mathcal{O}(\Delta t^3). \tag{4.42}$$

The velocity is first-order accurate:

$$\mathcal{E}_v = v((n-1/2)\Delta t) - v_{n-1/2} = -(f-\frac{1}{2})\Omega_n \mathbf{v}_n \times \hat{\mathbf{b}}_n \Delta t + \mathcal{O}(\Delta t^2). \tag{4.43}$$

This method is a poor choice because the lowest-order error in the Lorentz equation is independent of Δt. One consequence of an error term independent of Δt is that it renders a commonly used error checking technique useless. This non-rigorous method for checking error for a given problem is to measure the result as a function of Δt. If the injection error dominates the truncation error, the zeroth-order error is hidden and changing Δt will not change the error even if it is unacceptable.

Simple Boris Push

This method is a generalization of the Boris push using fractional time steps. The method depends only on the field values at time step n-1, of which the first (zeroth-order) method (called the simple injection method, Section 4.3.2) is a subset:

$$\begin{aligned} \mathbf{v}_{n-1/2} - \mathbf{v}_{n-f} &= \mathbf{e} c_1 \Delta t + \tan(\Omega c_2 \Delta t/2)(\mathbf{v}_{n-1/2} + \mathbf{v}_{n-f}) \times \hat{\mathbf{b}}, \\ \mathbf{x}_n - \mathbf{x}_{n-f} &= c_3 \mathbf{v}_{n-f/2} \Delta t, \text{ and} \\ \mathbf{v}_{n-f/2} - \mathbf{v}_{n-f} &= \mathbf{e} c_4 \Delta t + \tan(\Omega c_5 \Delta t/2)(\mathbf{v}_{n-f/2} + \mathbf{v}_{n-f}) \times \hat{\mathbf{b}}. \end{aligned} \tag{4.44}$$

Here the parameters $(c_1, \ldots, c_5)$ are independent of Δt, and $\mathbf{v}_{n-f/2}$ is a fictitious (not accurate) velocity at the fractional time step $n - f/2$, and $\Omega = \Omega(\mathbf{x}_{n-f}, n-1)$, $\mathbf{b} = \mathbf{b}(\mathbf{x}_{n-f}, n-1)$, and $\mathbf{e} = \mathbf{e}(\mathbf{x}_{n-f}, n-1)$. Substituting Eq. 4.44 into the injection truncation error equation, Eq. 4.23, then Taylor expanding, applying the chain rule, and choosing the five parameters to cancel the error coefficients in the expansions results in a first-order accurate method for general time-dependent fields. Due to the complexity and length of the analytic expression for the truncation error for this method with time-dependent fields, the expression is not shown here. The truncation error for the post-injection position, $\mathcal{E}_x$, is third-order, and the truncation error for the post-injection velocity, $\mathcal{E}_v$, is second-order. Table 4.3 shows the truncation error for the three test cases that will be described later.

The method with $c_1 = c_2 = f - 1/2$, $c_3 = f$, and $c_4 = c_5 = f/2$ is rewritten as,

$$\begin{aligned} \mathbf{v}_{n-1/2} - \mathbf{v}_{n-f} &= \mathbf{e}(f-\tfrac{1}{2})\Delta t + \tan(\Omega(f-\tfrac{1}{2})\Delta t/2)(\mathbf{v}_{n-1/2} + \mathbf{v}_{n-f}) \times \hat{\mathbf{b}}, \\ \mathbf{x}_n - \mathbf{x}_{n-f} &= f \mathbf{v}_{n-f/2} \Delta t, \text{ and} \\ \mathbf{v}_{n-f/2} - \mathbf{v}_{n-f} &= \mathbf{e}\tfrac{f\Delta t}{2} + \tan(\Omega f \Delta t/4)(\mathbf{v}_{n-f/2} + \mathbf{v}_{n-f}) \times \hat{\mathbf{b}}. \end{aligned} \tag{4.45}$$

Thus, from Eq. 4.45 it is seen that this method is almost as simple as standard leap-frog and has the minimum requirement that the error decreases with decreasing Δt.

Modified Fractional Time Step Boris Push

In this section, the fractional Boris push is modified to make it second-order accurate for uniform fields. To make an injection method second-order accurate, the velocity push must have an added term that is independent of the fractional time step, f, that an injected particle is pushed, but which depends on the time step for the push, Δt. This term is the lowest order truncation term from Eq. 4.21 ($d_{ttt}\mathbf{x}(t)\Delta t^2/24$). As shown in Section 4.3.2, Eq. 4.22, the second-order velocity error cancels in the left hand side of the leap-frog velocity update, Eq. 4.17, because of symmetry. On the right hand side of Eq. 4.17, the second-order velocity error contributes only to the second-order acceleration error. The entire truncation term ($d_{ttt}\mathbf{x}(t)\Delta t^2/24$) will be taken into account later; however, for this method only field terms independent of time and position will be used to construct this term. Using the normalized Lorentz equation (Eq. 4.16), $d_{ttt}\mathbf{x}(t)$ for a constant field is $d_{tt}\mathbf{x}(t) \times \mathbf{B}$; this can be calculated efficiently using $(\mathbf{v}_{n+1-f} - \mathbf{v}_{n-f}) \times \hat{\mathbf{b}}\Omega/\Delta t$. Alternatively, $d_{tt}\mathbf{x}(t) \times \mathbf{B}$ can be calculated using $\mathbf{e} \times \hat{\mathbf{b}}\Omega + \left(\hat{\mathbf{b}}(\hat{\mathbf{b}} \cdot \bar{\mathbf{v}}) - \bar{\mathbf{v}}\right)\Omega^2$; however, this is numerically less efficient because $\bar{\mathbf{v}}$ is not known.

The position advance, unlike the velocity push, has no cancellation of error terms due to symmetry. There is a neglected $d_{ttt}\mathbf{x}(t)$ term which is taken into account by a term $(\mathbf{v}_{n-f/2} - \mathbf{v}_{n-f}) \times \hat{\mathbf{b}}\Omega/\Delta t$, similar to the velocity update.

A second-order method for constant fields that incorporates the previously neglected velocity truncation term ($d_{ttt}\mathbf{x}(t)\Delta t^2/24$) is:

$$
\begin{aligned}
\mathbf{v}' - \mathbf{v}_{n-f} &= \mathbf{e}c_1\Delta t + \tan(\Omega c_2\Delta t/2)(\mathbf{v}' + \mathbf{v}_{n-f}) \times \hat{\mathbf{b}}, \\
\mathbf{v}_{n+1-f} - \mathbf{v}_{n-f} &= \mathbf{e}\Delta t + \tan(\Omega\Delta t/2)(\mathbf{v}_{n+1-f} + \mathbf{v}_{n-f}) \times \hat{\mathbf{b}}, \\
\mathbf{v}_{n-1/2} - \mathbf{v}' &= b_1(\mathbf{v}_{n+1-f} - \mathbf{v}_{n-f}) \times \hat{\mathbf{b}}\Omega\Delta t, \\
\mathbf{x}_n - \mathbf{x}_{n-f} &= c_3\mathbf{v}_{n-f/2}\Delta t + b_2(\mathbf{v}_{n-f/2} - \mathbf{v}_{n-f}) \times \hat{\mathbf{b}}\Omega\Delta t^2, \text{ and} \\
\mathbf{v}_{n-f/2} - \mathbf{v}_{n-f} &= \mathbf{e}c_4\Delta t + \tan(\Omega c_5\Delta t/2)(\mathbf{v}_{n-f/2} + \mathbf{v}_{n-f}) \times \hat{\mathbf{b}}.
\end{aligned}
\tag{4.46}
$$

Here the parameters $(c_1, \ldots, c_5)$, Ω, $\mathbf{b}$, $\mathbf{v}_{n-f/2}$, and $\mathbf{e}$ are defined as in Section 4.3.2 and parameters (b_1 and b_2) are independent of Δt. The velocity, $\mathbf{v}'$, is the final velocity in the fractional time step Boris push method (Section 4.3.2) and is now modified explicitly (all the other velocity equations of Eq. 4.46, are implicit) by the truncation term ($d_{ttt}\mathbf{x}(t)\Delta t^2/24$) discussed previously. Again substituting Eq. 4.46 into Eq. 4.23 and canceling all possible terms, it is found that this method is first-order for general time-dependent fields, but is second-order for spatial uniform fields. The truncation error for the injected position, $\mathcal{E}_x$, is third-order for general time-dependent fields and fourth-order for constant fields. The truncation error for the injected velocity, $\mathcal{E}_v$, is second-order for general fields, but for uniform fields the truncation coefficient is $d_{ttt}\mathbf{x}(t_n)/24$, the same as for leap-frog (Eq. 4.17). This results in a cancellation when going from the injection to the leap-frog integrator. The

method is rewritten as,

$$\begin{aligned}
\mathbf{v}' - \mathbf{v}_{n-f} &= \mathbf{e}(f-\tfrac{1}{2})\Delta t + \tan(\Omega(f-\tfrac{1}{2})\Delta t/2)(\mathbf{v}' + \mathbf{v}_{n-f}) \times \hat{\mathbf{b}}, \\
\mathbf{v}_{n+1-f} - \mathbf{v}_{n-f} &= \mathbf{e}\Delta t + \tan(\Omega\Delta t/2)(\mathbf{v}_{n+1-f} + \mathbf{v}_{n-f}) \times \hat{\mathbf{b}}, \\
\mathbf{v}_{n-1/2} - \mathbf{v}' &= \tfrac{1}{24}(\mathbf{v}_{n+1-f} - \mathbf{v}_{n-f}) \times \hat{\mathbf{b}}\Omega\Delta t, \\
\mathbf{x}_n - \mathbf{x}_{n-f} &= f\mathbf{v}_{n-f/2}\Delta t + \tfrac{f^2}{12}(\mathbf{v}_{n-f/2} - \mathbf{v}_{n-f}) \times \hat{\mathbf{b}}\Omega\Delta t^2, \\
\mathbf{v}_{n-f/2} - \mathbf{v}_{n-f} &= \mathbf{e}\tfrac{f\Delta t}{2} + \tan(\Omega f\Delta t/4)(\mathbf{v}_{n-f/2} + \mathbf{v}_{n-f}) \times \hat{\mathbf{b}}.
\end{aligned} \tag{4.47}$$

This method is more complex than the fractional time step Boris push.

Field Gradient Fractional Time Step Boris Push

This method achieves second-order accurate for time-independent fields by using the spatial derivatives of **B** and **E** that are calculated and used on the injection boundary. This method is based on the modified fractional time step Boris push of Section 4.3.2. First, the fields that are used are modified by the derivatives with different constants for the velocity and position integration:

$$\begin{aligned}
\Omega_v &= \Omega(\mathbf{x}_{n-f}, n-1) + d_1\mathbf{v}_{n-f} \cdot \nabla\Omega(\mathbf{x}_{n-f}, n-1)\Delta t, \\
\hat{\mathbf{b}}_v &= \hat{\mathbf{b}}(\mathbf{x}_{n-f}, n-1) + d_2\mathbf{v}_{n-f} \cdot \nabla\hat{\mathbf{b}}(\mathbf{x}_{n-f}, n-1)\Delta t, \\
\mathbf{e}_v &= \mathbf{e}(\mathbf{x}_{n-f}, n-1) + d_3\mathbf{v}_{n-f} \cdot \nabla\mathbf{e}(\mathbf{x}_{n-f}, n-1)\Delta t, \\
\Omega_x &= \Omega(\mathbf{x}_{n-f}, n-1) + d_4\mathbf{v}_{n-f} \cdot \nabla\Omega(\mathbf{x}_{n-f}, n-1)\Delta t, \\
\hat{\mathbf{b}}_x &= \hat{\mathbf{b}}(\mathbf{x}_{n-f}, n-1) + d_5\mathbf{v}_{n-f} \cdot \nabla\hat{\mathbf{b}}(\mathbf{x}_{n-f}, n-1)\Delta t, \text{ and} \\
\mathbf{e}_x &= \mathbf{e}(\mathbf{x}_{n-f}, n-1) + d_6\mathbf{v}_{n-f} \cdot \nabla\mathbf{e}(\mathbf{x}_{n-f}, n-1)\Delta t.
\end{aligned} \tag{4.48}$$

Second, for the velocity push, the truncation term $d_{ttt}\mathbf{x}(t_n)$ has the additional terms for time-independent fields denoted by:

$$\begin{aligned}
\zeta_x = \Omega(\mathbf{x}(t_n))d_{tt}\mathbf{x}(t_n) \times \hat{\mathbf{b}}(\mathbf{x}(t_n)) + \mathbf{v}(t_n) \cdot (\nabla\mathbf{e}(\mathbf{x}(t_n)) \\
+\nabla\Omega(\mathbf{x}(t_n))\mathbf{v}(t_n) \times \hat{\mathbf{b}} + \Omega(\mathbf{x}(t_n))\mathbf{v}(t_n) \times \nabla\hat{\mathbf{b}}(\mathbf{x}(t_n))\Big).
\end{aligned} \tag{4.49}$$

Time-independent second-order solutions do exist without the new term, ζ_x, in the truncation term, $d_{ttt}\mathbf{x}(t_n)/24$, in the velocity push; however, the coefficients have a functional form $1/(f-1/2)$ and are singular at $f = 1/2$; therefore, ζ_x will be used. Incorporating ζ_x and the fields modified by the derivatives of the fields into the previous injection method (Section 4.3.2) yields:

$$\begin{aligned}
\mathbf{v}' - \mathbf{v}_{n-f} &= \mathbf{e}_v c_1\Delta t + \tan(\Omega_v c_2\Delta t/2)(\mathbf{v}' + \mathbf{v}_{n-f}) \times \hat{\mathbf{b}}_v, \\
\mathbf{v}_{n+1-f} - \mathbf{v}_{n-f} &= \mathbf{e}\Delta t + \tan(\Omega\Delta t/2)(\mathbf{v}_{n+1-f} + \mathbf{v}_{n-f}) \times \hat{\mathbf{b}}, \\
\mathbf{v}_{n-1/2} - \mathbf{v}' &= b_1(\mathbf{v}_{n+1-f} - \mathbf{v}_{n-f}) \times \hat{\mathbf{b}}\Omega\Delta t \\
&\quad +d_7\mathbf{v}_{n-f} \cdot \left(\nabla\mathbf{e} + (\nabla\Omega\mathbf{v}_{n-f}) \times \hat{\mathbf{b}} + \Omega\mathbf{v}_{n-f} \times \nabla\hat{\mathbf{b}}\right)\Delta t^2, \\
\mathbf{x}_n - \mathbf{x}_{n-f} &= c_3\mathbf{v}_{n-f/2}\Delta t + b_2(\mathbf{v}_{n-f/2} - \mathbf{v}_{n-f}) \times \hat{\mathbf{b}}_x\Omega\Delta t^2, \text{ and} \\
\mathbf{v}_{n-f/2} - \mathbf{v}_{n-f} &= \mathbf{e}_x c_4\Delta t + \tan(\Omega_x c_5\Delta t/2)(\mathbf{v}_{n-f/2} + \mathbf{v}_{n-f}) \times \hat{\mathbf{b}}_x.
\end{aligned} \tag{4.50}$$

Here the parameters (b_1 and b_2), ($c_1, \ldots, c_5$), $\mathbf{v}_{n-f/2}$, $\mathbf{v}'$, Ω, $\mathbf{b}$, and $\mathbf{e}$ are the same as defined in Section 4.3.2 and the parameters ($d_1, \ldots, d_7$) are independent of Δt. Again substituting

Eq. 4.50 into Eq. 4.23 and canceling all possible terms by choosing parameters results in a second-order method for all time-independent field configurations, but a first-order method for time-dependent fields. The truncation error for the post-injected position, $\mathcal{E}_x$, is third-order for time-dependent fields and fourth-order for time-independent fields. The truncation error for the post-injected velocity, $\mathcal{E}_v$, is second-order for time-dependent fields, and the second-order term is $d_{ttt}\mathbf{x}(t_n)/24$ for time-independent field configurations. This method (with $d_7 = 1/24$) can be rewritten as:

$$\begin{aligned}
\mathbf{v}' - \mathbf{v}_{n-f} &= \mathbf{e}_v(f-\tfrac{1}{2})\Delta t + \tan(\Omega_v(f-\tfrac{1}{2})\Delta t/2)(\mathbf{v}' + \mathbf{v}_{n-f}) \times \hat{\mathbf{b}}_v, \\
\mathbf{v}_{n+1-f} - \mathbf{v}_{n-f} &= \mathbf{e}\Delta t + \tan(\Omega\Delta t/2)(\mathbf{v}_{n+1-f} + \mathbf{v}_{n-f}) \times \hat{\mathbf{b}}, \\
\mathbf{v}_{n-1/2} - \mathbf{v}' &= \tfrac{1}{24}(\mathbf{v}_{n+1-f} - \mathbf{v}_{n-f}) \times \hat{\mathbf{b}}\Omega\Delta t \\
&\quad + \tfrac{1}{24}\mathbf{v}_{n-f} \cdot \left(\nabla\mathbf{e} + (\nabla\Omega\mathbf{v}_{n-f}) \times \hat{\mathbf{b}} + \Omega\mathbf{v}_{n-f} \times \nabla\hat{\mathbf{b}}\right)\Delta t^2, \\
\mathbf{x}_n - \mathbf{x}_{n-f} &= \mathbf{v}_{n-f/2} f\Delta t + \tfrac{f^2}{12}(\mathbf{v}_{n-f/2} - \mathbf{v}_{n-f}) \times \hat{\mathbf{b}}_x\Omega\Delta t^2, \text{ and} \\
\mathbf{v}_{n-f/2} - \mathbf{v}_{n-f} &= \mathbf{e}_x\tfrac{f\Delta t}{2} + \tan(\Omega_x f\Delta t/4)(\mathbf{v}_{n-f/2} + \mathbf{v}_{n-f}) \times \hat{\mathbf{b}}_x,
\end{aligned} \tag{4.51}$$

using $d_1 = d_2 = d_3 = (f-1/2)/2$ and $d_4 = d_5 = d_6 = f/3$ in Eq. 4.48. Without a field gradient this case reduces to the modified fractional time step Boris push (Section 4.3.2).

General Second-Order Method

This is a method that is second-order for general spatially and temporally varying fields. This method requires field values at a previous time as well as spatial derivatives of **B** and **E**. Defining the field values to be used in this method to be a combination of old, new, and spatial derivatives results in:

$$\begin{aligned}
\Omega_v &= (1-t_1)\Omega(\mathbf{x}_{n-f}, n-1) + t_1\Omega(\mathbf{x}_{n-f}, n-2) + d_1\mathbf{v}_{n-f} \cdot \nabla\Omega(\mathbf{x}_{n-f}, n-1)\Delta t, \\
\hat{\mathbf{b}}_v &= (1-t_2)\hat{\mathbf{b}}(\mathbf{x}_{n-f}, n-1) + t_2\hat{\mathbf{b}}(\mathbf{x}_{n-f}, n-2) + d_2\mathbf{v}_{n-f} \cdot \nabla\hat{\mathbf{b}}(\mathbf{x}_{n-f}, n-1)\Delta t, \\
\mathbf{e}_v &= (1-t_3)\mathbf{e}(\mathbf{x}_{n-f}, n-1) + t_3\mathbf{e}(\mathbf{x}_{n-f}, n-2) + d_3\mathbf{v}_{n-f} \cdot \nabla\mathbf{e}(\mathbf{x}_{n-f}, n-1)\Delta t, \\
\Omega_x &= (1-t_4)\Omega(\mathbf{x}_{n-f}, n-1) + t_4\Omega(\mathbf{x}_{n-f}, n-2) + d_4\mathbf{v}_{n-f} \cdot \nabla\Omega(\mathbf{x}_{n-f}, n-1)\Delta t, \\
\hat{\mathbf{b}}_x &= (1-t_5)\hat{\mathbf{b}}(\mathbf{x}_{n-f}, n-1) + t_5\hat{\mathbf{b}}(\mathbf{x}_{n-f}, n-2) + d_5\mathbf{v}_{n-f} \cdot \nabla\hat{\mathbf{b}}(\mathbf{x}_{n-f}, n-1)\Delta t, \text{ and} \\
\mathbf{e}_x &= (1-t_6)\mathbf{e}(\mathbf{x}_{n-f}, n-1) + t_6\mathbf{e}(\mathbf{x}_{n-f}, n-2) + d_6\mathbf{v}_{n-f} \cdot \nabla\mathbf{e}(\mathbf{x}_{n-f}, n-1)\Delta t.
\end{aligned} \tag{4.52}$$

For the velocity injection push, the $d_{ttt}\mathbf{x}(t_n)$ truncation term for time-dependent fields contains the same terms, ζ_x (Eq. 4.49), as for time-independent fields in addition to the following terms:

$$\zeta_t = \partial_t\mathbf{e}(\mathbf{x}(t), t) + \partial_t\Omega(\mathbf{x}(t), t)\mathbf{v}(t) \times \hat{\mathbf{b}}(\mathbf{x}(t), t) + \Omega(\mathbf{x}(t), t)\mathbf{v}(t) \times \partial_t\hat{\mathbf{b}}(\mathbf{x}(t), t). \tag{4.53}$$

Therefore $d_{ttt}\mathbf{x}(t_n) = d_{tt}\mathbf{x}(t) \times \mathbf{B} + \zeta_x + \zeta_t$ for general fields. Incorporating this into the previous injection method given in Eq. 4.50 yields:

$$\begin{aligned}
\mathbf{v}' - \mathbf{v}_{n-f} &= \mathbf{e}_v c_1 \Delta t + \tan(\Omega_v c_2 \Delta t/2)(\mathbf{v}' + \mathbf{v}_{n-f}) \times \hat{\mathbf{b}}_v, \\
\mathbf{v}_{n+1-f} - \mathbf{v}_{n-f} &= \mathbf{e}\Delta t + \tan(\Omega \Delta t/2)(\mathbf{v}_{n+1-f} + \mathbf{v}_{n-f}) \times \hat{\mathbf{b}}, \\
\mathbf{v}_{n-1/2} - \mathbf{v}' &= b_1(\mathbf{v}_{n+1-f} - \mathbf{v}_{n-f}) \times \hat{\mathbf{b}}\Omega\Delta t \\
&\quad + d_7 \mathbf{v}_{n-f} \cdot \left(\nabla \mathbf{e} + (\nabla \Omega \mathbf{v}_{n-f}) \times \hat{\mathbf{b}} + \Omega \mathbf{v}_{n-f} \times \nabla \hat{\mathbf{b}}\right) \Delta t^2 \\
&\quad + t_7 \left(\mathbf{e} - \mathbf{e}(\mathbf{x}_{n-f}, n-2) + \Omega \mathbf{v}_{n-f} \times (\hat{\mathbf{b}} - \hat{\mathbf{b}}(\mathbf{x}_{n-f}, n-2)) \right. \\
&\quad \left. + (\Omega - \Omega(\mathbf{x}_{n-f}, n-2)) \mathbf{v}_{n-f} \times \hat{\mathbf{b}}\right) \Delta t, \\
\mathbf{x}_n - \mathbf{x}_{n-f} &= c_3 \mathbf{v}_{n-f/2} \Delta t + b_2 (\mathbf{v}_{n-f/2} - \mathbf{v}_{n-f}) \times \hat{\mathbf{b}}_x \Omega \Delta t^2, \text{ and} \\
\mathbf{v}_{n-f/2} - \mathbf{v}_{n-f} &= \mathbf{e}_x c_4 \Delta t + \tan(\Omega_x c_5 \Delta t/2)(\mathbf{v}_{n-f/2} + \mathbf{v}_{n-f}) \times \hat{\mathbf{b}}_x.
\end{aligned} \tag{4.54}$$

Here the parameters (b_1 and b_2), ($c_1, \ldots, c_5$), ($d_1, \ldots, d_7$), $\mathbf{v}_{n-f/2}$, $\mathbf{v}'$, Ω, $\mathbf{b}$, and $\mathbf{e}$ are as defined in Section 4.3.2, and the parameters ($t_1, \ldots, t_7$) are independent of Δt. Substituting Eq. 4.54 into Eq. 4.23, canceling all possible terms by choosing the $t_1, \ldots, t_7$ parameters results in a second-order method for arbitrary fields. The truncation error for the post-injected position, $\mathcal{E}_x$, is fourth-order for general fields. The truncation error for the post-injected velocity, $\mathcal{E}_v$, has $d_{ttt}\mathbf{x}(t_n)/24$ as a second-order term. For this method to be $\mathcal{O}(\Delta t^2)$ accurate, $t_1 = t_2 = t_3 = (2f-3)/4$, $t_4 = t_5 = t_6 = 2f/3 - 1$ in Eq. 4.52 and $t_7 = 1/24$ in Eq. 4.54. Since the only difference between Eq. 4.54 and Eq. 4.51 is the term with the t_7 coefficient added to the velocity update, this method will not be rewritten. With time-independent fields this method reduces to the field gradient fractional time step method in Section 4.3.2.

4.3.3 Computer Performance of Injection

The more accurate pushes are computationally more expensive. An operation count for the methods described here is given in Table 4.1, in three spatial and velocity coordinates; standard leap-frog is given as well. On contemporary computers the tangent function is by far the most expensive part of the push. If the tangent is used, then the ratio of the speed per each push is roughly proportional to the number of tangent function calls. Because of the expense of the tangent call, a small angle approximation is almost always used for time changing magnetic fields (if the magnetic field is time-independent then $\tan(\Omega\delta t/2)$ can be calculated once and stored, on a grid for spatially changing fields). If the small angle approximation is used, the ratio of the multiplication operation count will roughly be the ratio of the computation speed for each push. Therefore the fractional time step Boris push, modified Boris push, Boris push with field gradients, and the general second-order method are about 2.5, 4.7, 5.9, and 7 times as expensive as leap-frog. Due to different coding methods and compiler optimizations for implementing a push, a more accurate ratio is hard to estimate. For example, for the leap-frog push there is generally not a function call overhead for each particle; however, for our implementation, each injection

Method	Operation Count		
	Addition	Multiply	Tan
Simple Push	7	6	0
Fractional Time Step Boris Push	43	56	2
Modified Boris Push	89	105	3
Boris Push with Field Gradients	110	129	3
Second-Order Method	123	155	3
leap-frog	21	22	1

Table 4.1: Operation count for the different methods discussed in the text.

push does have a function call overhead. Also, more information is used in the higher order pushes, past time field values, and derivatives of fields; the retrieval time from the main memory of the computer may be a significant part of the time needed to calculate the injection push. However, due to the increase in accuracy the time step could be increased by up to an order of magnitude with the same error, see Figs. 4.13 through 4.15. The increased expense of calculating a higher order injection push is negated by a large savings in pushing particles in the plasma bulk with a larger time step, assuming the bulk has many more particles than are being injected each time step (it is difficult to construct a case were this is not true). For single species diode simulation which will have the fewest number of bulk particles to injected particles, the ratio can be as small as a hundred.

4.3.4 Results

The test cases analyzed here are special cases of the crossed-field diode [121, 126], illustrated in Fig. 5. For clarity, examples will be given in one dimension (XPDP1 [49]); however the general second-order method is implemented in XOOPIC [47] and XPDP2 [142, 143] in 2d. A uniform time-independent external magnetic field, B, is imposed parallel to the cathode surface along z. Under a constant imposed voltage, V_0, on the diode, the Hull field, B_H, is defined as the minimum field for magnetic insulation, such that one electron leaving the cathode with velocity v_x would just graze the anode:

$$B_H = \sqrt{\frac{2mV_0}{|e|L_x} + (\frac{mv_x}{|e|L_x})^2}, \tag{4.55}$$

where m is the mass and e is the charge of an electron. The imposed magnetic field for all the cases is 1.5×10^{-2} percent below the Hull field, hence, electrons are collected by the anode. For emission below the limiting current, J_c [103], all the current injected at the cathode propagates to the anode. This current is also known as the critical current, the largest current where a steady state cycloidal flow exists. The definition of critical current is also valid for solutions with fields larger than the Hull field where no particle current is transmitted. The three imposed field test cases are idealized limits of this diode,

	Case 1 *constant E*	Case 2 *gradient of E*	Case 3 *oscillatory E*
$mv_{0x}^2/(2q)$	0.5 eV		
$mv_{0y}^2/(2q)$	0.5 eV		
B $\hat{z}$	337 G ($\|\Omega\| = 5.92617 \times 10^9 rad/s$)		
Δ t	5×10^{-12} sec ($\|\Omega\|\Delta t = 0.0296$)		
E_0	-10^6 V/m	-9.391×10^4 V/m	-10^5 V/m
E_1	0	-4.49×10^9 V/m^2	0
ϵ	0	22.4824	0
ω	1	4.84580	1
$\tilde{E}$	0	0	1

Table 4.2: A summary of parameters used in the three test cases.

summarized in Table 4.2. The self-consistent case, summarized in Table 4.4, is a simulation near the limiting current slightly below the Hull field, then comparing with theory [126] the L_2 norm of the density for different injection methods and number of cells keeping $\Delta x/\Delta t$ a constant.

Case 1 approximates the initial condition ($t = 0$) in the gap. Initially, the gap is empty and there is a large vacuum electric field with no gradient. Case 2 approximates the steady state behavior of the gap for currents below the critical current. At steady state the electric field is smaller than the vacuum case, and the electric field gradient is large near the cathode. Both of these cases will be approximated by time-independent fields to simplify the problem. Case 3, a time-dependent example, approximates the 'oscillatory steady state' of a gap with a current above the critical current. The fields are not self-consistent but oscillate harmonically to make the analysis tractable. The frequency and amplitude of the electric field oscillation for the third case were obtained from a self-consistent PIC simulation with twice the critical current injected. Efficacy of injection methods will be compared. After the injection push, the particles are pushed with leap-frog as usual.

The lack of an unmagnetized example is not an oversight; because an unmagnetized push is a subset of the magnetized push, it is not done. These methods can be greatly simplified for the unmagnetized case; $\mathbf{v}_{n+1-f}$ is not needed for any of the pushes.

For the three test cases an analytic solution can be obtained. The equations of motion describing the idealized cases are:

$$\begin{aligned} \ddot{x}(t) &= \tfrac{q}{m}(E(x,t) + \dot{y}(t)B_0) \text{ and} \\ \ddot{y}(t) &= -\tfrac{q}{m}\dot{x}(t)B_0, \end{aligned} \tag{4.56}$$

where $E(x,t) = E_0(1 + \tilde{E}\cos(\omega_0' t)) + E_1 x$, and q and m are the charge and mass of the particle respectively. In terms of the dimensionless variables, $\tilde{x} = \Omega^2 m/(qE_0)\, x$ and $\tilde{t} = \Omega t$

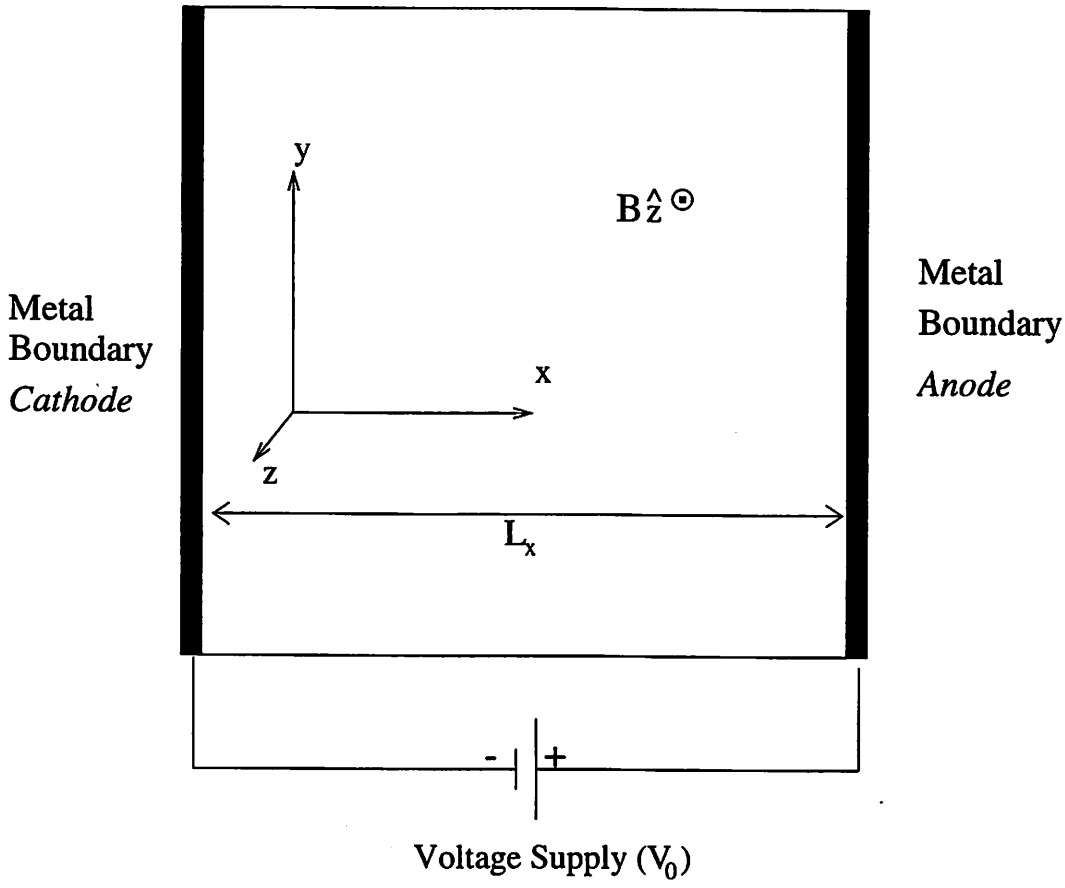

Figure 4.6: Model for the three cases and self-consistent examples. The cathode is at x=0.

with $\Omega = qB_0/m$ (signed cyclotron frequency) results in:

$$\begin{aligned} \ddot{\tilde{x}}(\tilde{t}) &= 1 + \tilde{E}\cos(\omega_0\tilde{t}) + \epsilon\tilde{x}(\tilde{t}) + \dot{\tilde{y}}(\tilde{t}) \\ \ddot{\tilde{y}}(\tilde{t}) &= -\dot{\tilde{x}}(\tilde{t}) \end{aligned} \tag{4.57}$$

where $\omega_0 = \omega_0'/\Omega$ and $\epsilon = (q/m)E_1/\Omega^2$. The solution may be written in closed form for this equation with the initial conditions $x(0) = 0$, $v_x(0) = \dot{x}(0) = v_{x0}$, and $v_y(0) = \dot{y}(0) = v_{y0}$.

$$\begin{aligned} \tilde{x}(\tilde{t}) &= \left\{\left[(v_{y0}+1)(\omega^2-\omega_0^2) + \omega^2\tilde{E}\right]\cos(\omega\tilde{t}) - \omega^2\tilde{E}\cos(\omega_0\tilde{t})\right. \\ &\quad \left. + (\omega^2-\omega_0^2)\left[v_{x0}\omega\sin(\omega\tilde{t}) - (v_{y0}+1)\right]\right\}/(\omega^2(\omega^2-\omega_0^2)) \\ \tilde{y}(\tilde{t}) &= \left\{\omega\omega_0(\omega^2-\omega_0^2)\left[-v_{x0} + (v_{y0}(\omega^2-1)-1)\tilde{t} + v_{x0}\cos(\omega\tilde{t})\right]\right. \\ &\quad \left. +\omega_0\left(\tilde{E}\omega^2 + (\omega^2-\omega_0^2)(v_{y0}+1)\right)\sin(\omega\tilde{t}) - \tilde{E}\omega^3\sin(\omega_0\tilde{t})\right\}/(\omega^3\omega_0(\omega^2-\omega_0^2)) \\ \tilde{v}_x(\tilde{t}) &= \left\{v_{x0}\omega(\omega^2-\omega_0^2)\cos(\omega\tilde{t}) + \left[(v_{y0}+1)(\omega^2-\omega_0^2) + \omega^2\tilde{E}\right]\sin(\omega\tilde{t})\right. \\ &\quad \left. -\tilde{E}\omega\omega_0\sin(\omega_0\tilde{t})\right\}/(\omega(\omega^2-\omega_0^2)) \\ \tilde{v}_y(\tilde{t}) &= \left\{\left[(v_{y0}+1)(\omega^2-\omega_0^2) + \omega^2\tilde{E}\right]\cos(\omega\tilde{t}) - \omega^2\tilde{E}\cos(\omega_0\tilde{t})\right. \\ &\quad \left. +(\omega^2-\omega_0^2)\left[v_{y0}(\omega^2-1) - 1 - v_{x0}\omega\sin(\omega\tilde{t})\right]\right\}/(\omega^2(\omega^2-\omega_0^2)) \end{aligned} \tag{4.58}$$

where $\omega^2 = 1 - \epsilon$. $\tilde{x}(\tilde{t})$, $\tilde{v}_x(\tilde{t})$, and $\tilde{v}_y(\tilde{t})$ will be compared to the numerical calculation. Figs. 4.7 through 4.12 compare the accuracy of the first push. The error is normalized by the Δx, Δv_x, or Δv_y of leap-frog push; this effectively slides the vertical axes without changing the shape of the graph. In other words, the normalization is reasonable but not unique. A different normalization would change the magnitude but not the shape of the error. The horizontal axis is the time elapsed since the particle has been injected from the cathode. Note that the error in v_y is dominated by the $d_{ttt}\mathbf{x}(t)\Delta t^2/24$ term in the non-corrected pushes. Figs. 4.13 through 4.15 show the root mean squared truncation error averaged over the fractional time step,

$$< ||\mathcal{E}|| >_f = \int_0^1 ||\mathcal{E}|| df, \tag{4.59}$$

for the different cases as a function of Δt. The lowest-order term in the RMS error is shown in Table 4.3. The leap-frog error is for a full time step. These figures were made by keeping one higher truncation error than the lowest order term; because of this, these figures may be inaccurate as $\Omega\Delta t$ approaches one.

The reason that injection push error is substantially larger than the leap-frog push in Case 3 as compared to Case 1 and Case 2 is that the time-dependent field is being extrapolated to a future point which incurs a larger error.

For models with cathode-field characteristics similar to one of the cases presented here using the truncation error can determine whether the injection push error is negligible. For example, assume for the moment that a fractional time step Boris push has been implemented. Using the electric field given in case 2, $E_0 = 9.391 \times 10^4\ V/m$, the gradient of

	Case 1	Case 2	Case3
Simple Push	g_{11}	g_{12}	g_{13}
Simple Boris Push	$g_{21}\Delta t$	$g_{22}\Delta t$	$g_{23}\Delta t$
Modified Boris Push	$g_{31}\Delta t^2$	$g_{32}\Delta t$	$g_{33}\Delta t$
Boris Push with Field Gradients	$g_{31}\Delta t^2$	$g_{42}\Delta t^2$	$g_{43}\Delta t$
Second-order Push	$g_{31}\Delta t^2$	$g_{42}\Delta t^2$	$g_{53}\Delta t^2$
Leap-Frog	$g_{61}\Delta t^2$	$g_{62}\Delta t^2$	$g_{63}\Delta t^2$

Table 4.3: A summary of the order of the injection methods shown in the text for different cases, the constant can be found in Appendix D.

the electric field which would result in hundred times the error over implementing the field gradient injection push is

$$g_{22}\Delta t \geq (100) g_{42}\Delta t^2, \tag{4.60}$$

where g_{22} and g_{42} are defined in Appendix D. By reducing Δt this relationship will be satisfied for some Δt; however, assuming because of other constraints in the bulk that Δt should be about 1×10^{-12} second, then Eq. 4.60 is satisfied if the normalized electric field gradient is between -2.25 ($4.00 \times 10^{11} V/m^2$) and -0.14 ($2.52 \times 10^{10} V/m^2$). For all other values of the electric field gradient it is more than one hundred times more accurate to use the field gradient push.

The above analysis is only the push truncation error and does not take into account the feedback of the coupling of the particles to the fields. The injection push is important when space charge is important and the error propagates through the system due to the error in the fields as well as the particles directly.

When a lower order or a non-time-centered push is used, the effects of the discrete time steps can be severe. For the examples shown here, there are gaps in particle positions between the time steps; if the field was chosen so that it decelerated the injected particles, particle positions from different time steps would have overlapped. This is a source of "noise" when these particles are weighted to the grid.

For the self-consistent simulation (all the parameters are shown in Table 4.4) the externally imposed magnetic field of 336G is 0.371 percent below the Hull field) and the injected current of 16705 A/m^2 is 2.50 percent below the critical current. Therefore, all the current injected at the cathode is collected by the anode.

The convergence in the cell size Δx is limited by the cold beam non-physical instability [46] proportional to Δx; whereas the accuracy of the field solve is Δx^2. This instability only occurs for a cold beam; we are using this cold example because we have a closed form for the solution. To reduce the effect of the cold beam instability, 8192 cells are used in the simulation of the crossed-field diode. This adds a fixed error in the simulation based on the grid error from the instability rather than the truncation error of the method. The L_2 norm of relative error $\|n_{PIC}/n_t - 1\|_2$ is shown is Fig. 4.16 as a function

Physical Parameters	$mv_{0x}^2/(2q)$	0.5 eV
	$B\ \hat{z}$	336 G ($\|\Omega\| = 5.9086 \times 10^9$rad/s)
	V_0	-10^4 V
	L	0.01 m
	J	16705 A/m^2
Physical Scaling Parameters	$B_H\ \hat{z}$	337.25 G
	J_c	17133.81 A/m^2
Numerical Parameter	Δx	1.22070×10^{-6} m

Table 4.4: A summary of parameters used in the self-consistent case.

of number of the time step in the simulation. This figure shows the error decreasing for the second-order (the general second-order method and the field gradient fractional time step Boris push because the problem is time-independent) injection method as Δt^2, first-order (modified fractional time step Boris push and fractional time step Boris push) injection methods methods Δt, and the zeroth-order (simple injection push) injection method not decreasing. Since the size of the cell Δx is not changing there is a constant error with respect to changing the time step Δt. The L_2 norm of the relative error due to the grid is approximated by the L_2 norm of the simulation run with $\Omega\Delta t = 9.2e-4$ to be about 4.74×10^{-4}. A fit to error of the second-order methods and first-order methods with the constant error (4.74×10^{-4}) from the grid is also shown on Fig. 4.16 and is labeled "Second Order Fit" and "First Order Fit" respectively.

4.4 Conclusions

Giving attention to detail, the authors have found methods that are second-order accurate for the inversion of distributions and injections of particles. The inversion process is limited to Maxwellian distributions and fluxes, both full distributions and arbitrary cutoff at a lower and upper velocity. The second-order injection method starts for an arbitrary position and velocity at the same time and results in a position and velocity half a time step apart, With an error consistent with the standard leap-frog integrator.

A number of common cases demonstrate sensitivity to low-order injection schemes. We have shown that using a higher order method is far more effective in obtaining a more accurate result that decreasing the time step with a lower order method. Use of these methods does not significantly increase the run time of the simulation, unless the number of particles injected is comparable to the total number of particles in the simulation.

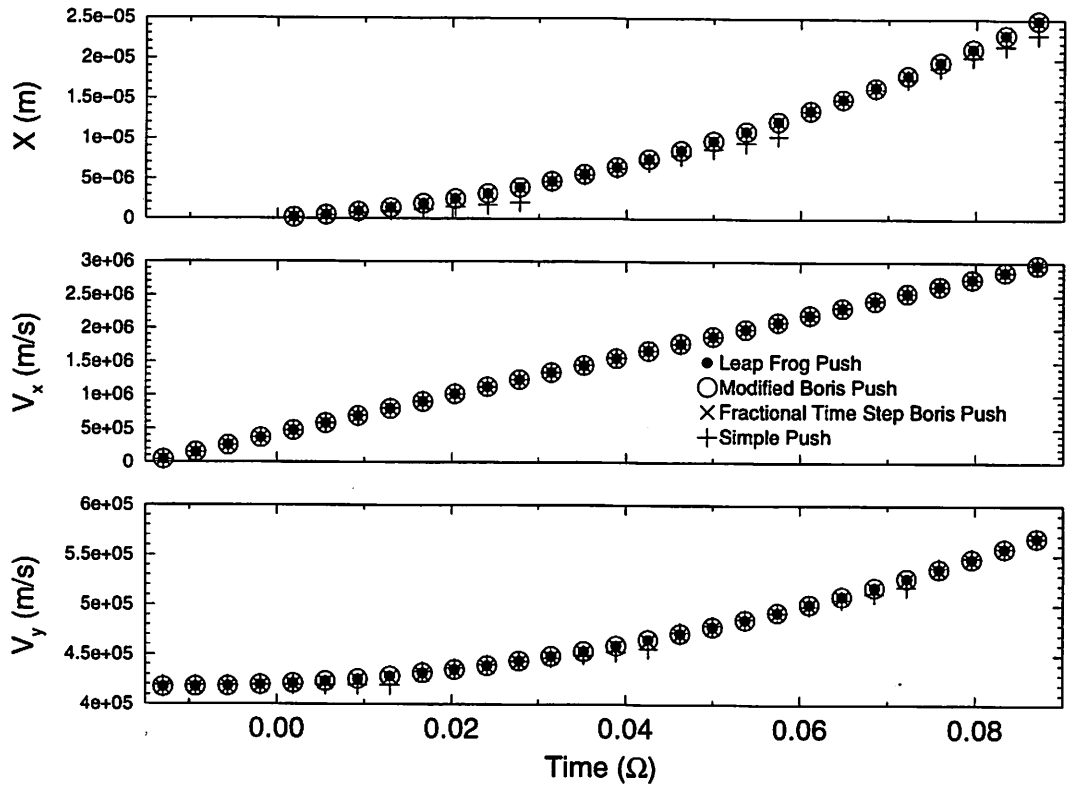

Figure 4.7: Comparison of position and velocity components for injection schemes with analytic results for Case 1 (constant electric field).

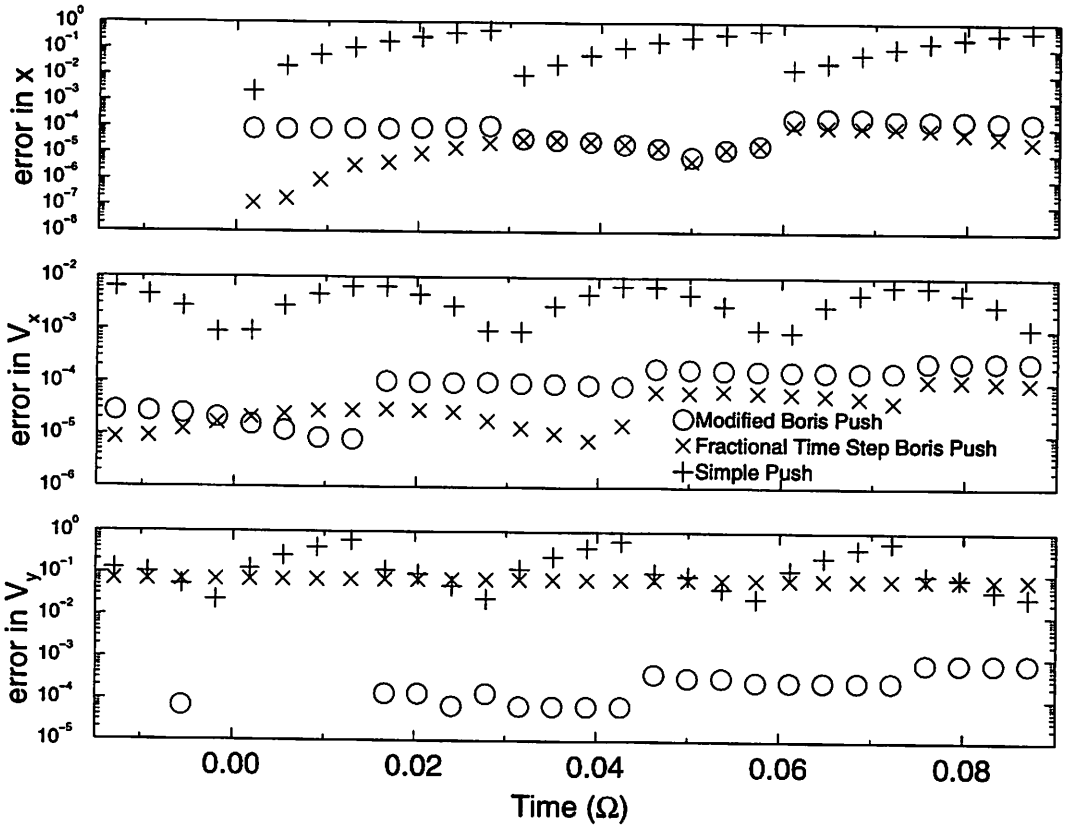

Figure 4.8: The fractional error in the injected particle's position and velocity with injection methods discussed in the text for Case 1 (constant electric field).

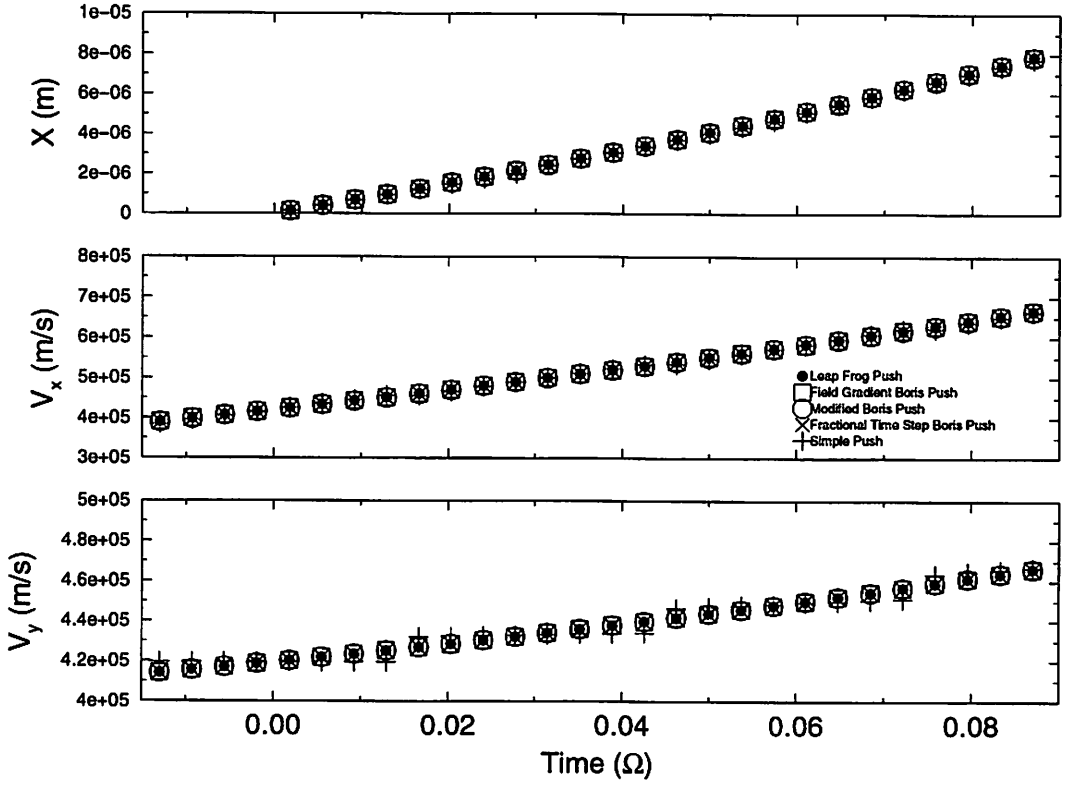

Figure 4.9: Comparison of position and velocity components for injection schemes with analytic results for Case 2.

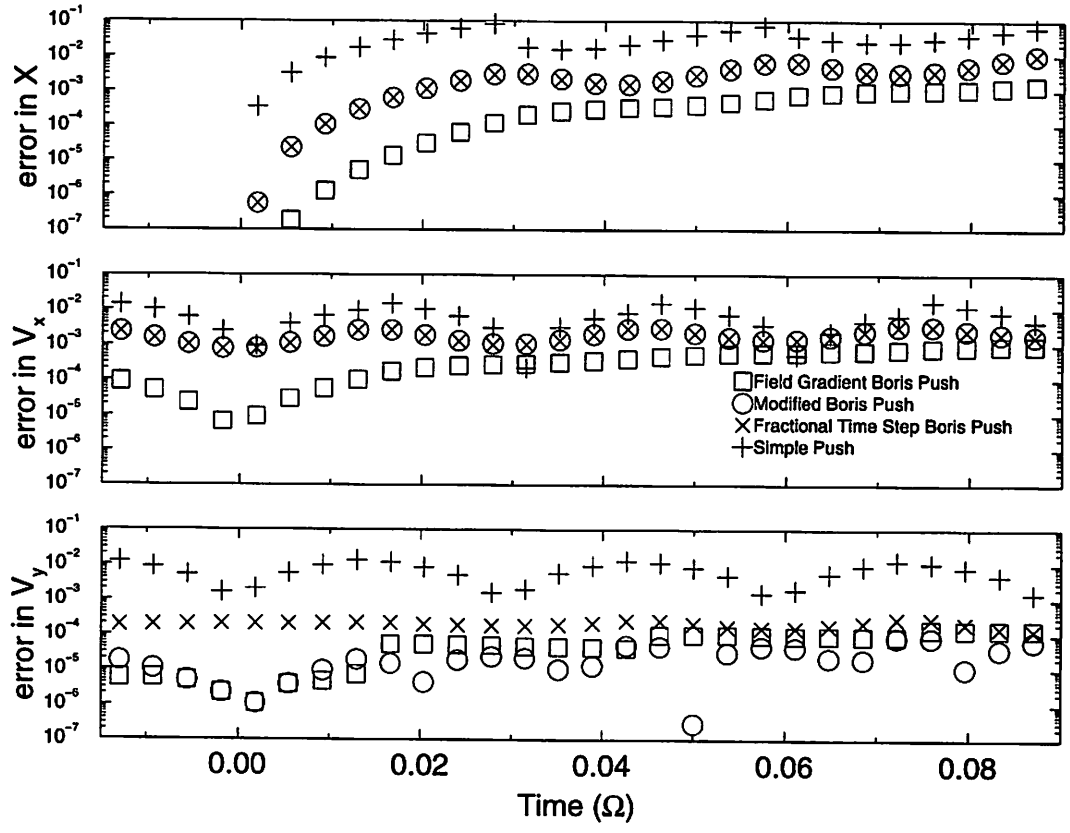

Figure 4.10: The fractional error in the injected particle's position and velocity with injection methods discussed in the text for Case 2.

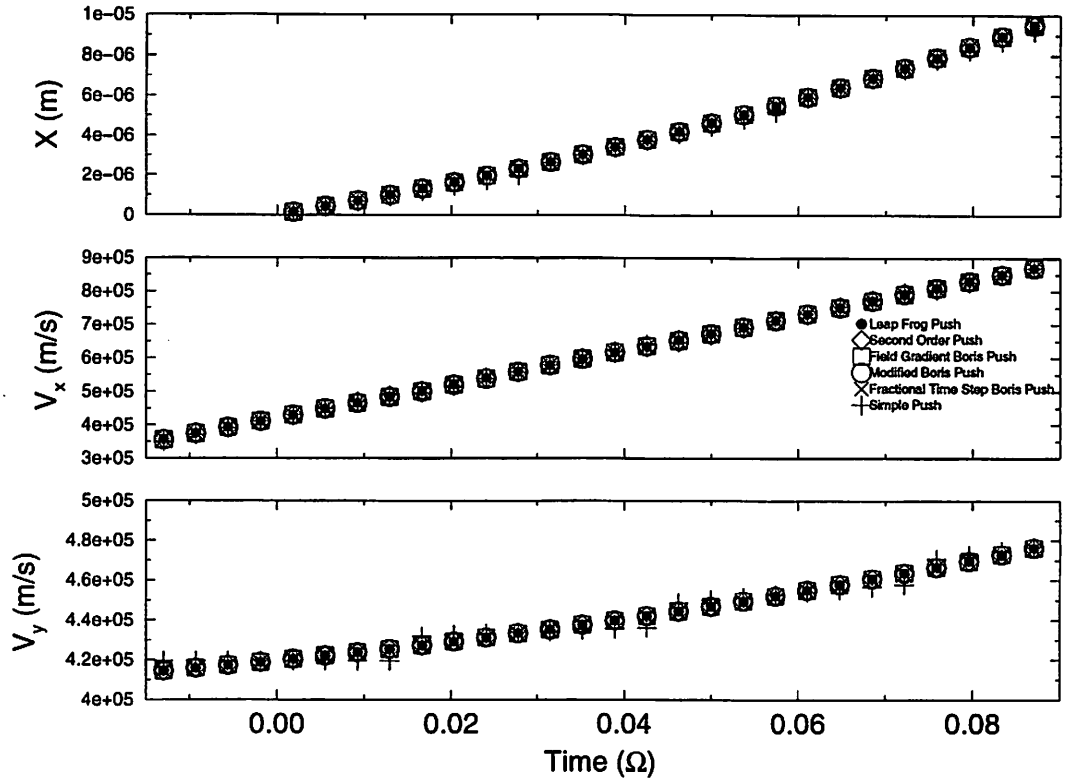

Figure 4.11: Comparison of position and velocity components for injection schemes with analytic results for Case 3.

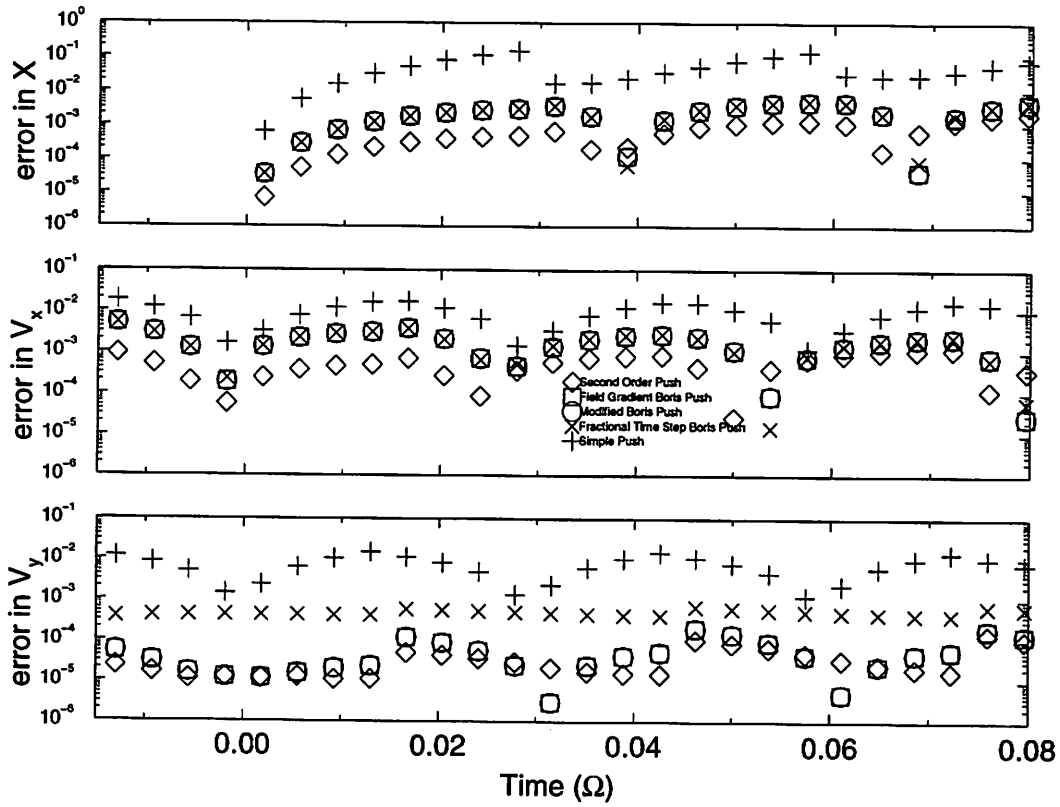

Figure 4.12: The fractional error in the injected particle's position and velocity with injection methods discussed in the text for Case 3.

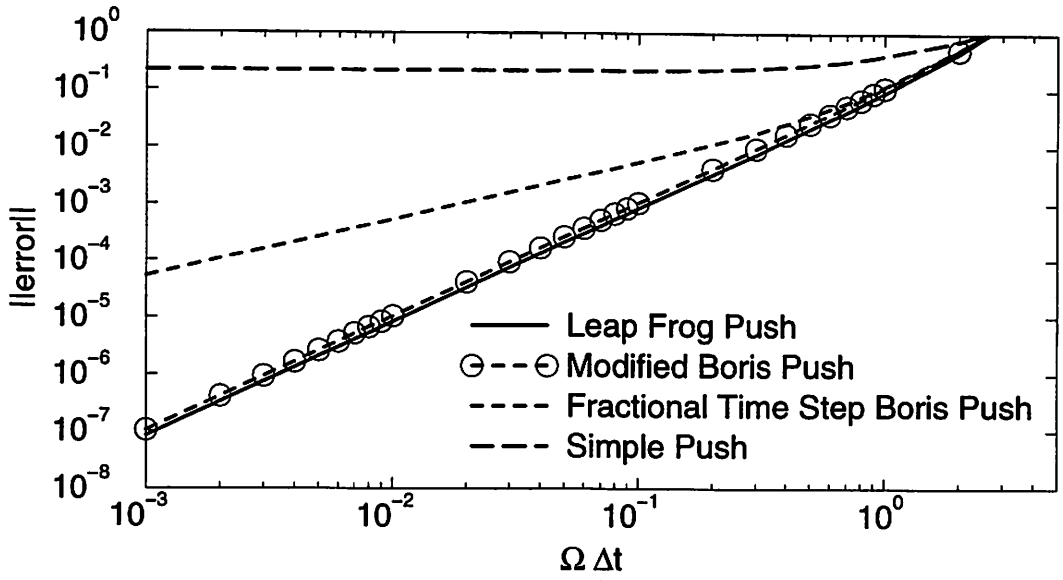

Figure 4.13: The error, $\|\mathcal{E}\|_2$, in the injection method averaged over the injection time during a time step with injection methods discussed in the text for Case 1.

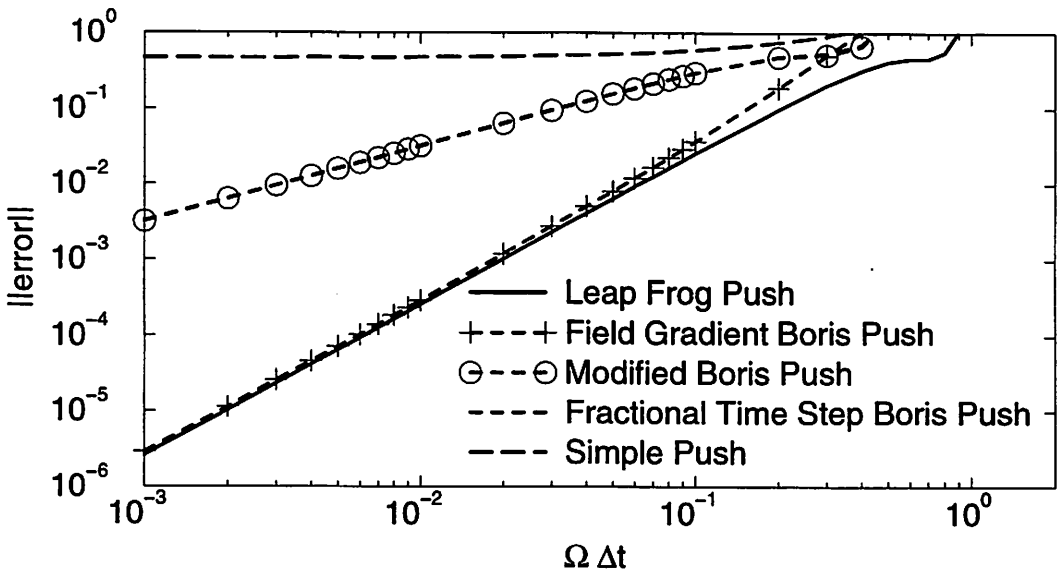

Figure 4.14: The error, $\|\mathcal{E}\|_2$, in the injection method averaged over the injection time during a time step with injection methods discussed in the text for Case 2.

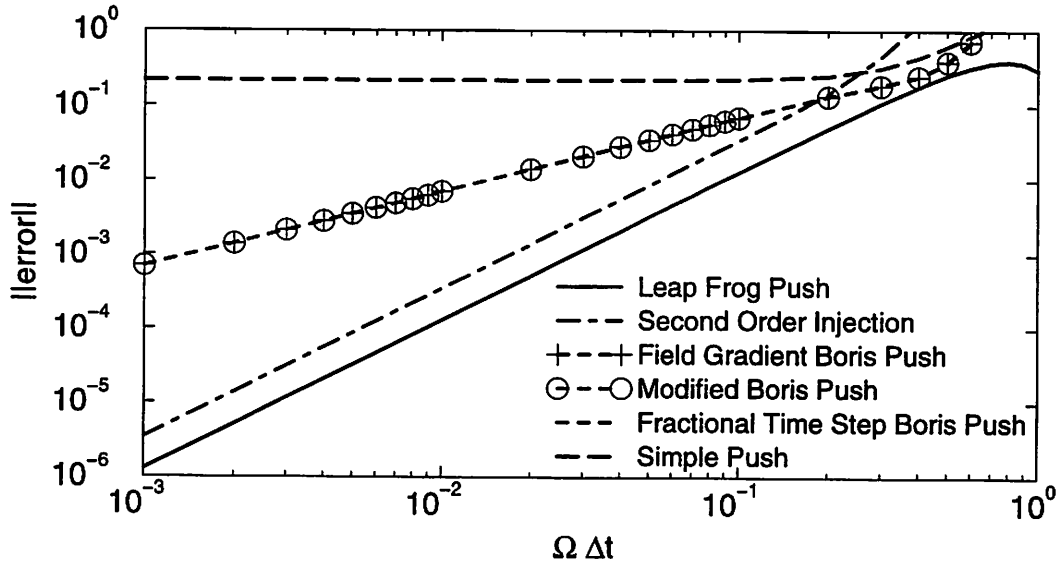

Figure 4.15: The error, $\|\mathcal{E}\|_2$, in the injection method averaged over the injection time during a time step with injection methods discussed in the text for Case 3.

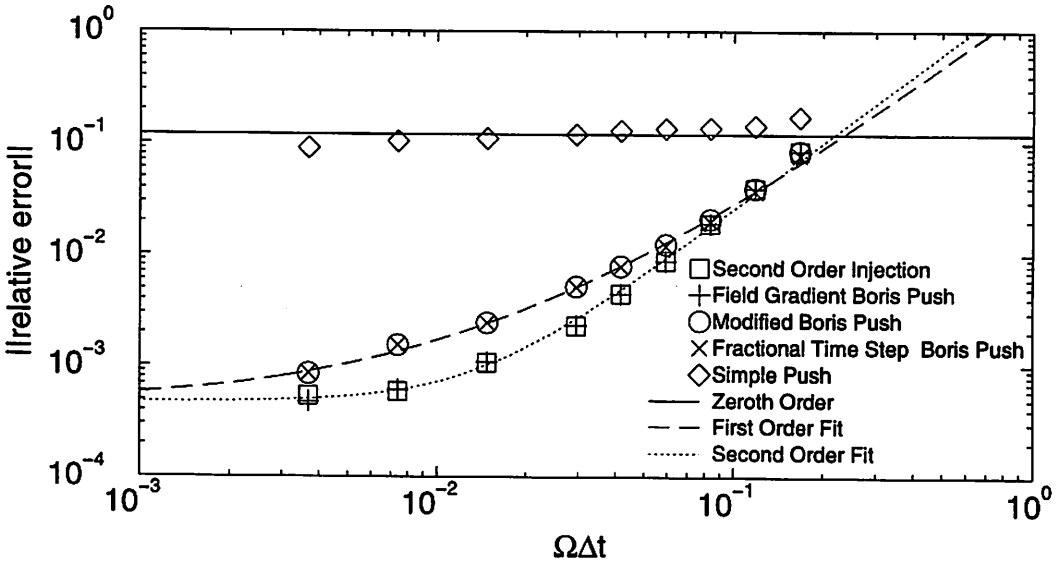

Figure 4.16: The the L_2 norm of the relative error ($\|n_{PIC}/n_i - 1\|_2$), in the diode for injection method given in the text for the self-consistent case.

Chapter 5

Nonlinear Hybrid Boltzmann-PIC Acceleration Algorithm

Submitted to Physics of Plasmas

5.1 Introduction

A hybrid electrostatic PIC algorithm is developed to investigate ion acoustic waves and other long time-scale, low frequency phenomenon, as well as to refine acceleration schemes which decrease the computer time needed for a simulation to reach steady state. The ions are treated as finite–sized particles, as in standard PIC codes[46]. There are two models for the electrons. First, the electrons are modeled with a Boltzmann relation, in which the electrons are inertia-less and come to equilibrium with the ions at each time step. This is different than previous work in this area that did not allow the Boltzmann electrons to evolve in time with the ions[68, 69, 70, 71, 72, 73, 74]. The second model uses the Boltzmann relation for the low energy, less collisional electrons; and kinetic PIC electrons for the high energy, more collisional electrons.

Many different Boltzmann–PIC hybrid schemes have been proposed [68, 69, 70, 71, 72, 73, 74, 75, 76, 77, 78, 79, 80]. Some of these are full electromagnetic (Maxwell's curl equations) [76] or Darwin (magneto-inductive)[75, 77, 78, 79, 80]. There have also been electrostatic models [68, 69, 70, 71, 72, 73, 74] similar to the one presented here; however, those schemes have assumed that the plasma is either globally charge-neutral [71], or that the Boltzmann flux matches the ion flux [70] (note: this is different than the globally charge-neutral case because the simulation could have been started with a net charge), or that the flux of Boltzmann electrons from the boundary is zero [68, 69], or the density of the Boltzmann electrons is fixed (along with the potential) at a spatial point in the simulation [72, 73, 74].

Our method is constructed to be suitable for bounded systems in which the density is dynamic and ambipolar diffusion is important, i.e., the plasma might develop a net

positive charge slowing the loss of electrons. The dynamics of the Boltzmann electron density are governed by enforcing charge and energy conservation. Also, to the author's knowledge, this is the first time ionization has been used with Boltzmann electrons in a PIC-Boltzmann hybrid code. The collisions are implemented using a modified MCC package based on work by Vahedi and Surendra[81]. (Note that Coulomb collisions were modeled between the Boltzmann electrons and ions by M. E. Jones et. al.,[75].)

The structure of this paper is as follows. First the assumptions of using a Maxwell-Boltzmann distribution are reviewed by re-deriving the Boltzmann relation. Second, we discuss the truncation of the tail of a Maxwell-Boltzmann distribution. The conclusion of this section is that the change in charge between a Maxwell-Boltzmann distribution with a tail and without a tail is minimal. The result that this charge can be neglected due to the removal of electrons from the tail of the distribution by the wall was also obtained in complementary way by Emmert et. al., [144]. Third, we introduce the algorithm for convergence of the Poisson equation with PIC charge species (e.g. multiple ion species and high energy PIC electrons) and one electron species with a Maxwell-Boltzmann distribution. The convergence of Poisson's equation depends on the conservation of charge of the Maxwell-Boltzmann distribution species. Fourth, using the energy conservation equation the temperature is determined for the Maxwell-Boltzmann distribution, which will be iteratively solved with Poisson's equation. Fifth, we discuss the transfer of PIC electrons to the Maxwell-Boltzmann distribution. The transfer of Maxwell-Boltzmann electrons to PIC electrons is not attempted and would be a refinement to this method. Lastly, two examples are given. The first example, utilizing photo-ionization, has ions that are PIC and electrons that have a Maxwell-Boltzmann distribution (no PIC electrons). The second example, a DC discharge, has PIC ions and electrons with the conversion process mentioned previously as the source of the Maxwell-Boltzmann distribution.

5.2 Model

In this paper, we use MKS units throughout, except for the temperature, which is measured in eV.

5.2.1 Classical Boltzmann Relation

The Boltzmann relation can be derived from the unmagnetized fluid equations [2, 145]; starting with momentum conservation:

$$mn(\frac{\partial \mathbf{u}}{\partial t} + (\mathbf{u} \cdot \nabla)\mathbf{u}) = qen\mathbf{E} - \nabla \cdot \mathbf{\Pi} + f_c, \tag{5.1}$$

where q is the charge of the Boltzmann species ($q = -1$ for electrons), e is the absolute value of the charge of an electron, $\mathbf{E}$ is the electric field vector, $\mathbf{u}$ is the mean velocity, and n is the density. The time rate of momentum transfer per unit volume due to collision with other species is represented by f_c.

To arrive at the Boltzmann relation the following assumptions are made. The pressure tensor, Π is taken to be isotropic, so that:

$$\nabla \cdot \Pi = e\nabla p. \tag{5.2}$$

We have chosen the isothermal relation for the thermodynamic equation of state; $p = nT$, where T is the uniform, isotropic temperature measured in eV. This relation is appropriate for slow-time variations where the temperature is allowed to reach equilibrium. The equation of state could be replaced with the more general relation $p = Cn\gamma$, where C is a constant.

The convective derivative has two terms: the first term, $\frac{\partial \mathbf{u}}{\partial t}$, represents an acceleration due to an explicitly time-varying velocity, $\mathbf{u}$; because we are looking for equilibrium solutions, there is no explicit variation in time, $\frac{\partial \mathbf{u}}{\partial t} = 0$. The second 'inertial' term, $(\mathbf{u}\cdot\nabla)\mathbf{u}$, represents an acceleration due to a spatially varying velocity. The second term can be neglected as long as the thermal energy is much larger that the drift energy and will be neglected upon linearizing the equation. Setting $m = 0$ produces the same mathematical result; however, this leads to the misconception that the electrons are massless, but what is actually neglected is electron momentum, $\mathbf{p} = m\mathbf{u}$. The thermal energy of the electrons is finite. In this model, it is assumed that the change of momentum due to the collision term f_c is small.

Using $\mathbf{E} = -\nabla\phi$ with Eqs. 5.1 and 5.2 and the equation of state $p = nT$ we obtain:

$$0 = \nabla(q\phi + T\ln(n)). \tag{5.3}$$

The solution to Eq. 5.3 is

$$n(\mathbf{x}) = n_0 e^{-\frac{q\phi(\mathbf{x})}{T}}, \tag{5.4}$$

where n_0 is the density where $\phi = 0$. Next, the electron distribution is taken to be in thermal equilibrium and is therefore Maxwellian[2, 145, 146]:

$$f(\mathbf{x},\mathbf{v}) = n(\mathbf{x})\frac{1}{4\pi}\sqrt{\frac{2}{\pi}}\left(\frac{m}{eT}\right)^{\frac{3}{2}} e^{-\frac{\frac{1}{2}m\mathbf{v}^2}{eT}}. \tag{5.5}$$

Eq. 5.5 is the Maxwell-Boltzmann distribution for three velocity components (three dimensional velocity space). The Maxwell-Boltzmann distribution is also the solution to the time-independent Vlasov equation.

Maxwell–Boltzmann electrons do not come to a true thermal equilibrium in a system where the potential at the boundaries of the system is finite. This is because the tail of the Boltzmann distribution continues out to arbitrarily large energy. We can use this model if we assume that the electrons come into equilibrium only with the plasma and not with the walls. The ramifications of cutting off the distribution at an arbitrary velocity is discussed in the next section.

5.2.2 Truncated Maxwell–Boltzmann Electrons

The higher-energy electrons are removed from the system when the electrons are collected by the walls of the system; the lower-energy electrons are confined by the sheaths. The tail of the distribution is repopulated by the scattering of the electrons.

In order to have a steady–state solution, there must be processes, either classical collisions or turbulence, that cause electrons to up-scatter in energy, so they can be lost from the system. Some sort of 'collisional' formalism for the electrons could be used; however, it is not clear how that could be implemented short of full PIC or numerically solving the Boltzmann equation some other way. A possible alternative is the approximation based on the Fokker-Planck equation (Krall and Trivelpiece, pp 295-300 [147], Nicholson, pp 66-67 and Appendix B [148]) which only accounts for two-body collisions. One would expect that it would take several scattering lengths to fill out the tail of the distribution. However, there is experimental evidence that the repopulation of the tail occurs in a distance much less than several mean free paths. The rapid repopulation of the tail is known as the Langmuir paradox[149, 150], and has yet to be resolved.

In this section we derive the the equivalent Boltzmann relation, Eq. 5.4, for three different truncations of the tail of a Maxwell-Boltzmann distribution. The conclusion for all truncated distribution methods is that the space charge of the tail is negligible if the truncation energy is greater than about about three times the temperature. In the examples shown at the end of this article, the truncation energy is greater than three times the temperature and we over-count the charge in the tail in the electron distribution. The full Maxwell-Boltzmann distribution is faster to solve numerically than the truncated distributions; therefore, we will us the full distribution whenever possible. The energy of the tail of the electron population is important and we take this into account when calculating the collisions.

First, the relationship between the electron density and potential for symmetric upper cutoff of the Maxwell-Boltzmann distribution for three-dimensional velocity space is derived. This model should be applied when the the scattering length is long compared to the system or when kinetic electrons are being modeled for the tail. Second, a truncated model is formulated where only the electron tail returning from the wall is truncated (one velocity component). This model is appropriate to use in the sheath region. The truncated tail would be repopulated within the length of the system, since the scattering length is shorter than the system. Third, a 1d truncated model is formulated where only the electrons in the tail resolved by the simulation are truncated. For example, if x is the coordinate being simulated then v_x is the velocity that is truncated. This 1d model would be appropriate when the mean free path is much larger than the size of the system being simulated.

Isotropic Upper Velocity Cutoffs for Maxwell-Boltzmann Distributions

This model is applicable for a system where the scattering length is larger than the size of the system. This is also assuming that the angle of the velocities becomes isotropic faster than the up-scattering of the electrons in energy. The truncated model only makes physical sense in a bounded system where the potential in the plasma $q\phi(\mathbf{x})$ is less than the wall potential, $q\phi_w$; therefore $q(\phi(\mathbf{x}) - \phi_w) < 0$. The electron distribution is a truncated Maxwellian distribution; in other words, $f(\mathbf{x}, v)$ (v is the magnitude of $\mathbf{v}$) must vanish for

$$\frac{1}{2}mv^2 > -qe\left(\phi(\mathbf{x}) - \phi_w\right). \tag{5.6}$$

This implies that the distribution is isotropic. The diagram of the distribution function, Fig. 5.1, for this distribution has an upper cutoff for the magnitude of the velocity. The total energy of the cutoff is constant, therefore the kinetic energy of the cutoff is a function of position. For a non-constant wall potential the maximum of the wall voltages is chosen for ϕ_w, thus there is only one cutoff for a simulation. This could be modified if the wall is emitting particles either though secondaries or thermionic emission. For this distribution the cutoff speed is defined to be

$$v_c(\mathbf{x}) = \sqrt{-\frac{2qe}{m}(\phi(\mathbf{x}) - \phi_w)}, \tag{5.7}$$

therefore the speed when $\phi(\mathbf{x}) = 0$ is

$$v_0 = \sqrt{\frac{2qe}{m}\phi_w}. \tag{5.8}$$

This leads to an electron density for the isotropic cutoff:

$$n_{iso}(\mathbf{x}) = n_0 e^{-\frac{q\phi(\mathbf{x})}{T}} \frac{\int_0^{v_c} v^2 e^{-\frac{\frac{1}{2}mv^2}{eT}} dv}{\int_0^{v_0} v^2 e^{-\frac{\frac{1}{2}mv^2}{eT}} dv}. \tag{5.9}$$

With $\psi = -\frac{q(\phi(\mathbf{x})-\phi_w)}{T}$, this simplifies to:

$$n_{iso}(\mathbf{x}) = n_0 e^{-\frac{q\phi(\mathbf{x})}{T}} \frac{2\sqrt{\psi}e^{-\psi} - \sqrt{\pi}erf(\sqrt{\psi})}{2\sqrt{\frac{q\phi_w}{T}} - \sqrt{\pi}erf(\sqrt{\frac{q\phi_w}{T}})}. \tag{5.10}$$

To examine difference the between the truncated and full Maxwell-Boltzmann model we will use a common approximation for the undriven sheath potential drop from Lieberman and Lichtenberg [2], $\phi_s = -\frac{T_e}{2}\ln(\frac{M}{2\pi m})$ and presheath drop, $\phi_p = -\frac{T_e}{2}$. The potential difference between the bulk and wall is $\phi_w = \phi_p + \phi_s$. Using a mass ratio for atomic hydrogen, $M/m = 1837$, the fractional difference in the density between the isotropic cutoff density and the full Maxwell-Boltzmann density at the presheath-bulk interface is less than

1.4 percent. Atomic hydrogen is a worst case example; as the mass ratio becomes larger the sheath potential drop will be larger in magnitude and the cutoff higher. Therefore, the relationship between density and potential for the cutoff Maxwellian will approach the full Maxwellian. The fractional difference in the density grows in the sheath, becoming infinite at the wall, because the truncated distribution density is zero at the boundary. For a comparison of density versus potential (Eq. 5.10) for this sheath potential model see Fig. 5.4, which also has the other models used in this paper. The difference between the potential and position is not analyzed directly, but is small because the comparison of density and potential is small.

Asymmetric Upper Velocity Cutoffs for Maxwell-Boltzmann Distributions

For this distribution, the velocity component of electrons moving away from the wall (the wall is taken to be on the right of the simulation region, so the velocity component truncated is along x) is truncated, i.e., f(**x**,**v**) must vanish for:

$$v_x(\mathbf{x}) < -\sqrt{-\frac{2qe}{m}(\phi(\mathbf{x}) - \phi_w)}. \tag{5.11}$$

In the diagram of the distribution function, Fig. 5.2, this distribution function would have a lower (left) cutoff for the velocity along x. This would lead to an electron density:

$$n_a(\mathbf{x}) = n_0 e^{-\frac{q\phi(\mathbf{x})}{T}} \frac{1 - \frac{1}{2}erfc(\sqrt{\psi})}{1 - \frac{1}{2}erfc(\sqrt{\frac{q\phi_w)}{T}})}. \tag{5.12}$$

In the bulk, the full Boltzmann relation is used. The edge of the plasma is taken to be at $\phi_p = -\frac{T_e}{2}$. In other words, Eq. 5.12 is used for $\phi > -\frac{T_e}{2}$ and Eq. 5.4 is used for $\phi \leq -\frac{T_e}{2}$. At the edge of the bulk the transition from the asymmetric model to the full distribution, the jump in density is 0.68 percent (this is much smaller than the perturbations caused by the 'noise' of the ions). At the wall ($\phi = \phi_w$) the fractional difference in density between the models is 50 percent. For a comparison of density versus potential for the wall potential model see Fig. 5.4. Emmert et. al., [144] have also analyzed this truncation model and have concluded that the change in charge due to the tail of the distribution is unimportant to the structure of an undriven sheath. There is even less difference between this truncation model and the full Maxwell-Boltzmann distribution than with the isotropic truncation model.

Symmetric Single Velocity Upper Cutoffs for Maxwell-Boltzmann Distributions

This model is applicable for a 1d system where the scattering length is larger than the size of the system. Both the electrons moving towards the wall and away from the wall are a truncated Maxwell-Boltzmann distribution. The electrons moving towards the wall have been truncated by the wall on the other side of the system. The distribution function must vanish for:

$$|v_x(\mathbf{x})| > \sqrt{-\frac{2qe}{m}(\phi(\mathbf{x}) - \phi_w)}. \tag{5.13}$$

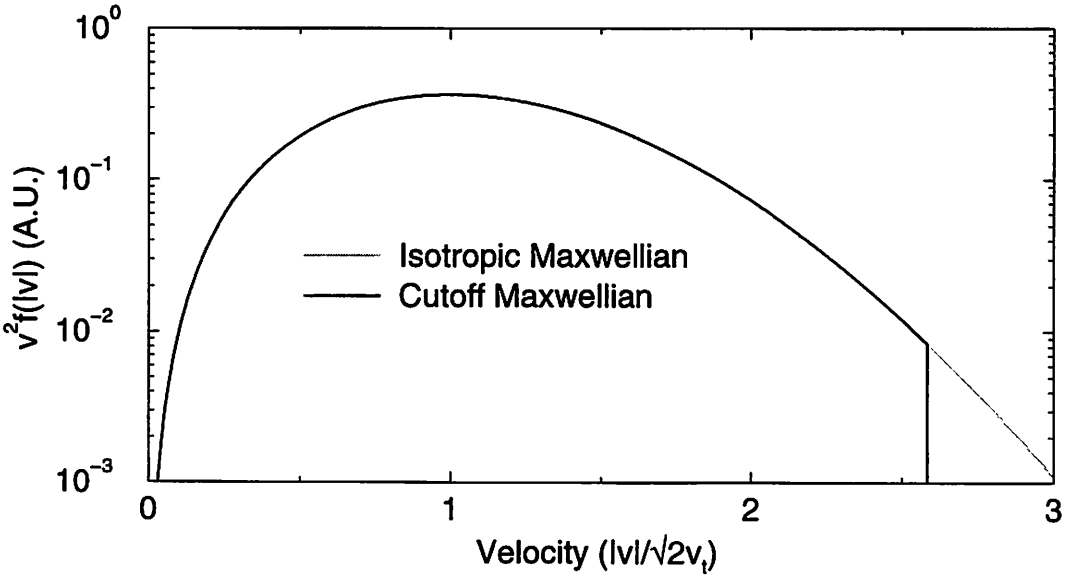

Figure 5.1: This shows a full Maxwellian distribution and Maxwellian with an isotropic cutoff tail. The magnitude of the velocity is cutoff at $v = 1.83v_t$ which is the truncation velocity for sheath drop for atomic hydrogen mass ratio for the sheath model described in the text.

In the diagram of the distribution function, Fig. 5.3, this distribution function would have a lower (left) cutoff and an upper (right) cutoff for the velocity in the x-direction. This distribution leads to an electron density:

$$n_{1ds}(\mathbf{x}) = n_0 e^{-\frac{q\phi(\mathbf{x})}{T}} \frac{erf(\sqrt{\psi})}{erf(\sqrt{\frac{q\phi_w}{T}})}. \tag{5.14}$$

This model is somewhat inconsistent because the directions transverse to the x-direction are still considered to be in thermal equilibrium with a full tail. A comparison of the density versus potential for the parameters used earlier is shown in Fig. 5.4.

5.3 Poisson Equation with Charge Conservation Applied

Independent of the equation used to relate the potential to the density, Eq. 5.4, 5.10, 5.12, or 5.14, Poisson's equation can be cast in the following form:

$$\nabla^2\phi = -\frac{\rho(\mathbf{x})}{\epsilon_0} = -\frac{e}{\epsilon_0}(n_{PIC}(\mathbf{x}) + q\, n_{e0} F(\phi(\mathbf{x}))), \tag{5.15}$$

n_{e0} is a constant of integration (the electron density at $\phi = 0$), q is the charge of the Boltzmann species ($q = -1$ for electrons), e is the absolute value of the charge of an electron, $n_{PIC}(\mathbf{x})$ is the number density of the PIC species, and $\rho(\mathbf{x})$ is the total charge

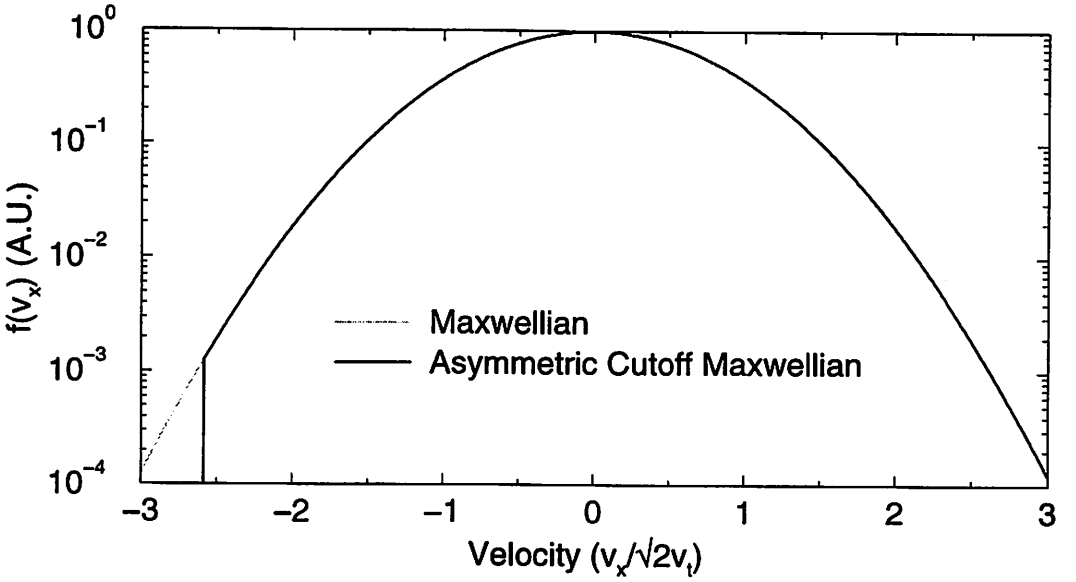

Figure 5.2: This shows a full Maxwellian distribution and Maxwellian with a 1d (x-direction) asymmetric cutoff tail. The velocity cutoff is a $v_x = -1.83v_t$ which is the truncation velocity for sheath drop for atomic hydrogen mass ratio for the sheath model described in the text.

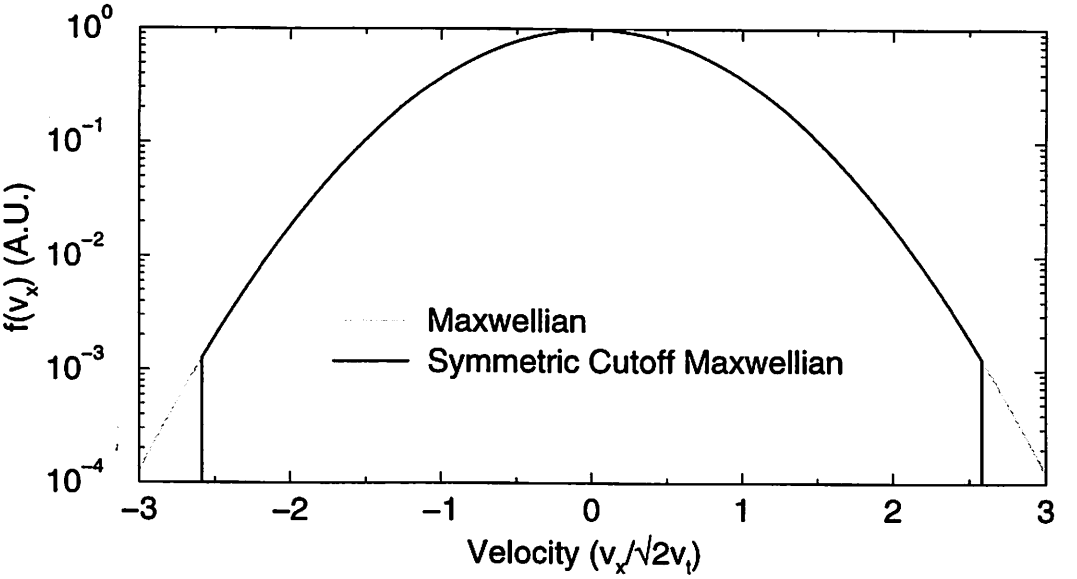

Figure 5.3: This shows a full Maxwellian distribution and Maxwellian with a 1d (x-direction) symmetric cutoff tail. The velocity cutoff is a $v_x = \pm 1.83v_t$ which is the truncation velocity for sheath drop for atomic hydrogen mass ratio for the sheath model described in the text.

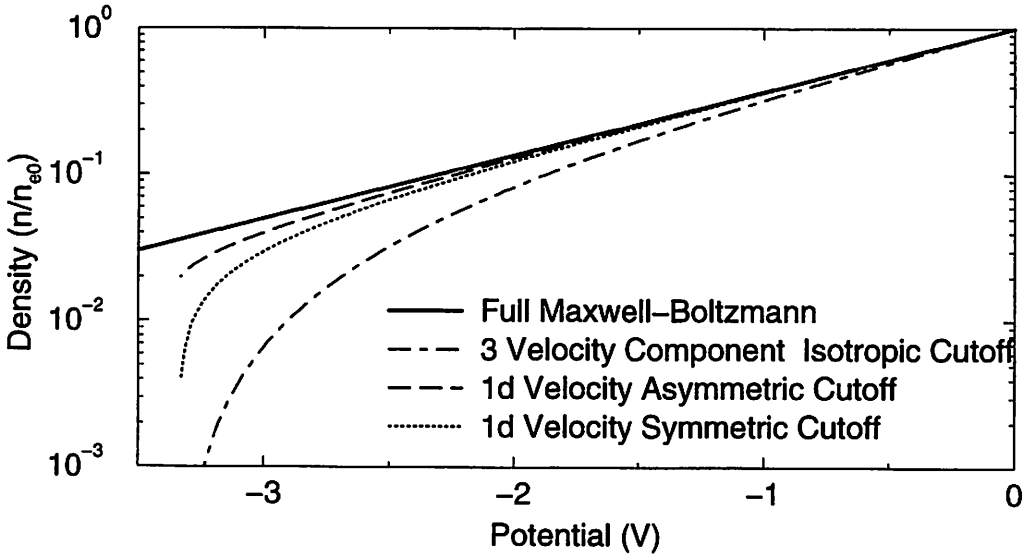

Figure 5.4: The density versus the potential for the Boltzmann relation and the three cutoff Maxwell-Boltzmann distributions described in the text for a cutoff of $\phi_w \sim 3.34T_e$, the sheath drop for atomic hydrogen mass ratio.

density (PIC plus Boltzmann species). $F(\phi(\mathbf{x}))$ is obtained from Eq. 5.4, 5.10, 5.12, or 5.14 and is summarized here:

$$F(\phi(\mathbf{x})) = e^{-\frac{q\phi(\mathbf{x})}{T}} \begin{cases} 1, & \text{full distribution}, \\ \left(\frac{2\sqrt{\psi}e^{-\psi}-\sqrt{\pi}erf(\sqrt{\psi})}{2\sqrt{\frac{q\phi_w}{T}}-\sqrt{\pi}erf(\sqrt{\frac{q\phi_w}{T}})}\right), & \text{isotropic cutoff distribution}, \\ \left(\frac{1-\frac{1}{2}erfc(\sqrt{\psi})}{1-\frac{1}{2}erfc(\sqrt{\frac{q\phi_w}{T}})}\right), & \text{asymmetric cutoff distribution}, \\ \left(\frac{erf(\sqrt{\psi})}{erf(\sqrt{\frac{q\phi_w}{T}})}\right), & \text{1d symmetric distribution}, \end{cases} \tag{5.16}$$

where $\psi = -\frac{q(\phi(\mathbf{x})-\phi_w)}{T}$. In this paper the nomenclature is for a single electron temperature but the theory may be expanded to include an arbitrary number of electron temperatures or another species, such as a negative ion species for an electro–negative gas discharge (Lieberman and Lichtenberg page 318 [2]). The time savings of modeling a negative ion species is not large because of the similarities of positive and negative ion masses.

Proper choice of n_{e0} determines whether this method is going to converge and converge to the correct solution. To calculate n_{e0}, conservation of charge of the Maxwell-Boltzmann species is used. This changes n_{e0} from a constant of integration to a property of the boundary condition, by keeping track of the flow at the boundaries and the creation of the ion-electron pairs through ionization. Starting with the continuity equation for the

Boltzmann electrons:

$$\frac{\partial n}{\partial t} + \nabla \cdot (n\mathbf{u}) = g - l, \tag{5.17}$$

where g and l are the ionization and recombination rates per unit volume respectively. Integrating the continuity equation, Eq. 5.17, over the simulation region results in:

$$\frac{dN_B}{dt} + \int_{\mathbf{S}} n\mathbf{u} \cdot d\mathbf{S} = G - L. \tag{5.18}$$

G and L are volumetric ionization and recombination rate of the Boltzmann electrons respectively. The surface, S, bounds the simulation. The total number of Boltzmann electrons is:

$$N_B = \int_V n_{e0} F(\phi(\mathbf{x}))d\mathbf{x} = n_{e0} \int_V F(\phi(\mathbf{x}))d\mathbf{x}, \tag{5.19}$$

where $d\mathbf{x}$ is the volume element and V is the total volume of the simulation. Recombination is often negligible and will not be considered here. G is taken to be

$$G = \int_V \nu_i n_e(\mathbf{x})d\mathbf{x} = n_g \int_V \int_{\mathbf{v}} \sigma_i(v) v f(\mathbf{x}, \mathbf{v}) d\mathbf{v} d\mathbf{x}, \tag{5.20}$$

where $\mathbf{v}$ is the electron velocity, $d\mathbf{v}$ is a volume element of velocity space, ν_i is the ionization frequency, and $\sigma_i(v)$ is the ionization cross section.

For the full Maxwellian distribution the volumetric ionization is

$$G = N_B n_g (\tfrac{m}{\pi T})^{\frac{3}{2}} \textstyle\int_0^\infty \sigma_i(v) v\, e^{-\frac{mv^2}{2T}} 4\pi v^2 dv. \tag{5.21}$$

The spatial integral of volumetric ionization for the cutoff distributions cannot be done in general because the limits of integration of the velocity depend on position. However, once the potential, $\phi(\mathbf{x})$, is known then the integral can be done numerically. The integral, written as explicitly as possible, is

$$G = n_g n_{e0} \int_V \int_{\mathbf{v}} \sigma_i(v) v F(\phi(\mathbf{x})) \frac{1}{4\pi} \sqrt{\frac{2}{\pi}} \left(\frac{m}{eT}\right)^{\frac{3}{2}} e^{-\frac{\frac{1}{2}m\mathbf{v}^2}{eT}} d\mathbf{v} d\mathbf{x}, \tag{5.22}$$

where the correct limit of the distribution function should be used for each distribution. In general the ionization cross section will have a minimum energy threshold, thus the velocity integral will have an effective lower bound.

The Boltzmann electron flux to a wall is:

$$\Gamma_{\text{wall}} = -n(x_{\text{wall}}) \int \mathbf{v} \cdot \hat{n} f(\mathbf{v}) d^3\mathbf{v}, \tag{5.23}$$

where $\hat{n}$ is the outward unit normal vector of the simulation boundary; therefore, a negative flux is moving out of the system. For the four distributions discussed previously, the particle

flux is:

$$\Gamma_{wall} = -\sqrt{\frac{2eT}{\pi m}} n_{e0} e^{-q\phi(\mathbf{x})/T} \begin{cases} \frac{1}{2}, & \text{full distribution}, \\ \frac{e^{\frac{q\phi_w}{T}} - (1+\psi)) e^{\frac{q\phi(\mathbf{x})}{T}}}{-4\sqrt{\frac{q\phi_w}{T}} + 2\sqrt{\pi} e^{\frac{q\phi_w}{T}} erf(\sqrt{\frac{q\phi_w}{T}})}, & \text{isotropic cutoff distribution}, \\ \frac{1}{\sqrt{\pi}\left(1+erf(\sqrt{\frac{q\phi_w}{T}})\right)}, & \text{asymmetric cutoff distribution}, \\ \frac{1-e^{-\psi}}{2\sqrt{\pi} erf(\sqrt{\frac{q\phi_w}{T}})}, & \text{1d symmetric distribution}. \end{cases} \tag{5.24}$$

For the isotropic and 1d symmetric cutoff distribution the flux is zero when $\phi(\mathbf{x}) \leq \phi_w$; this is noted because when high energy PIC electrons are used for the tail of the distribution, the cutoff potential is different than the wall potential. If $\phi_w > \phi_{plasma}$, where ϕ_{plasma} is the plasma potential, then the plasma potential is used for ϕ_w. This boundary condition follows from the continuity equation, if $\phi_w > \phi_{plasma}$ the Boltzmann electron flux at the wall would be greater than the Boltzmann electron flux in the plasma where $\phi = \phi_{plasma}$. This is the same boundary condition used in fluid codes, such as INDUCT94 [151]. A current, J, can also be specified through any boundary, due to primary or secondaries emission of Boltzmann electrons. The average net flux, $\bar{\Gamma}_{\text{wall}}$, out of the system is defined as $A\bar{\Gamma}_{\text{wall}} = \int_S (\Gamma_{\text{wall}} + J/eq) dS$, with A the area of the surface, S, enclosing the simulation. The change in the number of Boltzmann electrons during a time step can be written as:

$$\Delta N_B = \left(\bar{\Gamma}_{\text{wall}} A + G\right) \Delta t. \tag{5.25}$$

The number of Boltzmann electrons is updated by $N_B(t + \Delta t) = N_B(t) + \Delta N_B$; this is a first-order advance in time for the number of Boltzmann electrons. Since the simulations are approaching equilibrium, the temperature, the current J, and wall potential are approaching constant values in time; for constant temperature and wall potential this advance is exact. A similar first-order update for the energy is used in Section 5.4 and a second-order iterative advance is given in Appendix E. The initial number of Boltzmann electrons, N_B, is chosen so that the simulation starts charge-neutral, $N_B = \int_V n_{PIC}(\mathbf{x}) d\mathbf{x}$.

The iterative method used to solve Eq. 5.15 with the constraint, Eq. 5.19, is based on Newton(-Raphson) iteration. Rewriting Poisson's equation (Eq. 5.15) with a nonlinear Boltzmann species:

$$\delta(\phi(\mathbf{x})) = \nabla^2 \phi(\mathbf{x}) + \frac{e}{\epsilon_0} \left(n_{PIC}(\mathbf{x}) + q\, n_{e0} F(\phi(\mathbf{x}))\right), \tag{5.26}$$

where the iteration will continue until

$$\frac{\|\delta(\phi(\mathbf{x}))\|_{L_2}}{\|\text{boundary condition} + \rho/\epsilon_0\|_{L_2}} \leq \epsilon_{error}. \tag{5.27}$$

The tolerance, ϵ_{error}, used is 10^{-4} and $\|\text{boundary conditions} + \rho/\epsilon_0\|_{L_2}$ is the L_2 norm of the charge (including the Boltzmann species charge) and the boundary conditions, the

known quantities in the equation. In other words, we normalize by the L_2 norm of b when Poisson's equation is discretized in the form $Ax = b$. Let $\phi^i(\mathbf{x})$ be the approximate solution to Eq. 5.26 at the i^{th} iteration. Let $\Delta\phi(\mathbf{x}) = \phi^{i+1}(\mathbf{x}) - \phi^i(\mathbf{x})$ be the change (assumed small) during the iteration. We expand the equation about the present solution:

$$\delta(\phi^{i+1}(\mathbf{x})) = \delta(\phi^i(\mathbf{x}) + \Delta\phi(\mathbf{x})) = \delta(\phi^i(\mathbf{x})) + \frac{\partial\delta(\phi^i(\mathbf{x}))}{\partial\phi^i(\mathbf{x})}\Delta\phi(\mathbf{x})) + h.o.t. \tag{5.28}$$

Ignoring terms higher order than $(\Delta\phi(\mathbf{x}))^2$ in this equation and setting $\delta(\phi^{i+1}(\mathbf{x})) = 0$, this equation can be rewritten as:

$$\frac{\partial\delta(\phi^i(\mathbf{x}))}{\partial\phi^i(\mathbf{x})}\phi^{i+1}(\mathbf{x}) = -\delta(\phi^i(\mathbf{x})) + \frac{\partial\delta(\phi^i(\mathbf{x}))}{\partial\phi^i(\mathbf{x})}\phi^i(\mathbf{x})). \tag{5.29}$$

Hockney and Eastwood[48] on page 173 show that this scheme (Eq. 5.29) converges quadratically (same as for standard Newton's method); however, Newton's method does not always converge. For certain initial values the iterative scheme does not necessarily convergence to a solution. See, for example, Ref. [152] page 367 or for a more mathematical treatment see Chapter three of Delaney [153]. Differentiating Eq. 5.26 with respect to $\phi(\mathbf{x})$:

$$\frac{\partial\delta(\phi(\mathbf{x}))}{\partial\phi(\mathbf{x}))} = \nabla^2 + \frac{e\,q\,n_{e0}}{\epsilon_0}\frac{\partial F(\phi(\mathbf{x}))}{\partial\phi(\mathbf{x})}. \tag{5.30}$$

Substituting Eq. 5.30 into Eq. 5.29:

$$\begin{gathered}\left(\nabla^2 + \frac{e\,q\,n_{e0}}{\epsilon_0}\frac{\partial F(\phi^i(\mathbf{x}))}{\partial\phi^i(\mathbf{x})}\right)\phi^{i+1}(\mathbf{x}) = \\ -\frac{e}{\epsilon_0}\left(n_{PIC}(x) + q\,n_{e0}\left(F(\phi^i(\mathbf{x})) - \frac{\partial F(\phi^i(\mathbf{x}))}{\partial\phi^i(\mathbf{x})}\phi^i(\mathbf{x})\right)\right).\end{gathered} \tag{5.31}$$

This iterative scheme for the full Maxwellian Boltzmann relation, Eq. 5.4, is

$$\left(\nabla^2 - \frac{e\,q^2}{\epsilon_0 T}\,n_{e0}e^{-q\phi^i/T}\right)\phi^{i+1}(\mathbf{x}) = -\frac{e}{\epsilon_0}\left(n_{PIC}(x) + q\,n_{e0}\left(1 + \frac{q}{T}\phi^i(\mathbf{x})\right)e^{-q\phi^i(\mathbf{x})/T}\right). \tag{5.32}$$

To simplify the iterative scheme with the truncated Maxwell-Boltzmann electron distributions, we define: $\psi^i = -q(\phi^i(\mathbf{x}) - \phi_w)/T$. The isotropic cutoff Boltzmann relation, Eq. 5.10, substituted into Eq. 5.31 is

$$\begin{gathered}\left(\nabla^2 - n_{e0}\frac{e\,q^2}{\epsilon_0 T}\frac{\sqrt{\pi}e^{\psi^i}erf(\sqrt{\psi^i})}{2\sqrt{q\phi_w/T} - \sqrt{\pi}e^{q\phi_w/T}erf(\sqrt{q\phi_w/T})}\right)\phi^{i+1}(\mathbf{x}) = \\ -\frac{e}{\epsilon_0}\left(n_{PIC}(x) + q\,n_{e0}\left(\frac{2\sqrt{\psi^i}e^{q\phi^i(\mathbf{x})/T} - \sqrt{\pi}(1+\frac{q}{T}\phi^i(\mathbf{x}))e^{\phi_w}erf(\psi^i)}{2\sqrt{q\phi_w/T} - \sqrt{\pi}e^{q\phi_w/T}erf(\sqrt{q\phi_w/T})}\right)e^{-q\phi^i(\mathbf{x})/T}\right).\end{gathered} \tag{5.33}$$

To simplify the the iteration equation for the last two cutoff distributions, we define $a = 1 + erf(\sqrt{\psi^i})$ and $b = exp(-q\phi_w/T)/(\sqrt{\pi\psi^i})$. The 1d asymmetric cutoff Boltzmann relation, Eq. 5.12, substituted into Eq. 5.31 is

$$\begin{gathered}\left(\nabla^2 - n_{e0}\frac{e\,q^2}{\epsilon_0 T}\frac{b + ae^{-q\phi^i(\mathbf{x})/T}}{1 + erf(\sqrt{q\phi_w/T})}\right)\phi^{i+1}(\mathbf{x}) = \\ -\frac{e}{\epsilon_0}\left(n_{PIC}(x) + q\,n_{e0}\left(\frac{a(1+\frac{q}{T}\phi^i(\mathbf{x}))e^{-q\phi^i(\mathbf{x})/T} + b\frac{q}{T}\phi^i(\mathbf{x})}{1 + erf(\sqrt{q\phi_w/T})}\right)\right).\end{gathered} \tag{5.34}$$

The 1d symmetric cutoff Boltzmann relation, Eq. 5.14, substituted into Eq. 5.31 is

$$\left(\nabla^2 - n_{e0}\frac{eq^2}{\epsilon_0 T}\frac{b+erf(\sqrt{\psi^i})e^{-q\phi^i(x)/T}}{erf(\sqrt{q\phi_w/T})}\right)\phi^{i+1}(\mathbf{x}) = -\frac{e}{\epsilon_0}\left(n_{PIC}(x) + q\,n_{e0}\left(\frac{erf(\sqrt{\psi^i})\left(1+\frac{q}{T}\phi^i(\mathbf{x})\right)e^{-q\phi^i(x)/T}+b\frac{q}{T}\phi^i(\mathbf{x})}{erf(\sqrt{q\phi_w/T})}\right)\right). \tag{5.35}$$

The Laplacian operator, ∇^2, is discretized by a second-order centered-difference. For example, in one dimension (1d):

$$\nabla^2\phi(x_j) = \frac{\phi_{j-1} - 2\phi_j + \phi_{j+1}}{(\Delta x)^2}. \tag{5.36}$$

The second term on the left hand side of Eqs. 5.32, 5.33, 5.34, and 5.35 only affects the center term in the finite difference: ϕ_j in 1d. Note that the second term on the left hand side of Eqs. 5.32, 5.33, 5.34, and 5.35 is always negative; this assures that the matrix will converge because it is diagonally dominant [154]. An external circuit has been added that is solved simultaneously with the internal fields in 1d [49] and in 2d [143]. In 2d the problem cannot be decomposed into a Poisson and Laplace equation, as is commonly done for numerical efficiency, because the field solve is nonlinear. This scheme has been successfully implemented using a tridiagonal solve [152] in 1d (XPDP1 [49]) and using DADI [155] and a multigrid method [156] in 2d (XOOPIC [157]). When using DADI there is a $\phi_{(j,k)}$ coefficient for each direction. We have taken the obvious approach and changed both coefficients equally. The global convergence of the iteration scheme has not been proven; however, as mentioned before, this scheme converges quadratically if the initial guess is in the basin of convergence. This scheme converges for all models used so far. These models include Neumann and Dirichlet boundaries on the outer edge of the simulation region and Dirichlet structures inside the simulation region.

5.4 Determining the Temperature of the Boltzmann Species

So far we have taken the temperature of the Boltzmann species to be fixed. Now we will use energy conservation to determine the temperature. The energy conservation equation for the Boltzmann electrons is:

$$\frac{\partial}{\partial t}\left(\frac{3}{2}p\right) + \nabla\cdot\frac{3}{2}(p\mathbf{u}) + p\nabla\cdot\mathbf{u} + \nabla\cdot\mathbf{q} = \frac{\partial}{\partial t}\left(\frac{3}{2}p\right)|_c, \tag{5.37}$$

where $\frac{3}{2}p$ is the energy density (J/m^3), $\frac{3}{2}p\mathbf{u}$ is the macroscopic energy flux (W/m^2) representing the flow of the internal energy density at the fluid velocity $\mathbf{u}$, $p\nabla\cdot\mathbf{u}$ (W/m^3) gives the heating or cooling of the fluid due to compression or expansion of its volume, $\mathbf{q}$ is the heat flow vector (W/m^2) which gives the microscopic energy flux, and the collisional term includes all collisional processes that change the energy density. These include ionization, excitation, and elastic scattering. The equation is closed by setting $\nabla\cdot\mathbf{q} = 0$ or by letting

$\mathbf{q} = -\kappa_T \nabla T$, where κ_T is the thermal conductivity and T is uniform ($\nabla T = 0$). Integrating over space, letting $p = nT$, and defining the total energy to be $E_t = \frac{3}{2} N_B T = 3/2 \int_V p d\mathbf{x}$, the energy equation is

$$\frac{dE_t}{dt} + \frac{5}{2} T \int_{\mathbf{S}} n\mathbf{u} \cdot d\mathbf{S} = \left.\frac{dE}{dt}\right|_c . \tag{5.38}$$

The integral is the flux found previously and $dE/dt|_c$ for the full Maxwell-Boltzmann distribution and uniform neutral background density is

$$\left.\frac{dE}{dt}\right|_c = N_B n_g \left(\frac{m}{\pi T}\right)^{\frac{3}{2}} \int_0^\infty \left(\mathcal{E}_i \sigma_i(v) + \mathcal{E}_e \sigma_e(v) + \mathcal{E}_s \sigma_s(v)\right) v e^{-\frac{mv^2}{2T}} 4\pi v^2 dv. \tag{5.39}$$

$\mathcal{E}_i$, $\mathcal{E}_e$ and $\mathcal{E}_s$ are the energy loss per collision and $\sigma_i(v)$, $\sigma_e(v)$ and $\sigma_s(v)$ are the collision cross sections for ionization, excitation, and elastic scattering respectively. For the truncated Maxwell-Boltzmann distributions the position integral can not be done in general and must be done numerically once the potential, $\phi(\mathbf{x})$, is known because the limits of integration of velocity depend on $\phi(\mathbf{x})$. The integral that needs to be evaluated is

$$\left.\frac{dE}{dt}\right|_c = n_g n_{e0} \int_V \int_{\mathbf{v}} \left(\mathcal{E}_i \sigma_i(v) + \mathcal{E}_e \sigma_e(v) + \mathcal{E}_s \sigma_s(v)\right) v F(\phi(\mathbf{x})) \frac{1}{4\pi} \sqrt{\frac{2}{\pi}} \left(\frac{m}{eT}\right)^{\frac{3}{2}} e^{-\frac{\frac{1}{2}mv^2}{eT}} d\mathbf{v} d\mathbf{x}. \tag{5.40}$$

This integral is easier to evaluate for the cases of interest than in general because σ_e and σ_i are zero below a certain threshold energy which for many cases is above the retarding energy of the wall potential, $q\phi_w$. The change in the total energy of the system, E_t, during a time step is:

$$\Delta E_t = \Delta t \left(\left.\frac{dE}{dt}\right|_c - \frac{5}{2} T A \bar{\Gamma}_{\text{wall}} \right) - \Delta E_{PIC}. \tag{5.41}$$

ΔE_{PIC} is the energy of the PIC particles that are absorbed or emitted by the boundaries. There could also be a source of energy for the Boltzmann electrons caused by emission from the wall. The total energy of for next time step is then $E_t(t + \Delta t) = E_t(t) + \Delta E_t(t)$. The change in total energy, Eq. 5.41, and the change in the number of Boltzmann particles, Eq. 5.25, are both first-order in Δt. This has been adequate for the problems in this article which vary slowly in time. An untested second-order method is outlined in Appendix E. The total energy of the system is held constant during an iteration:

$$E_t - \sum_{PIC} \frac{1}{2} \frac{mv^2}{e} = \frac{3}{2} N_B T + \frac{1}{2e} \int_V \phi(\mathbf{x}) \rho(\mathbf{x}) d\mathbf{x}. \tag{5.42}$$

This relation is now a constraint on T, just as Eq. 5.19 is a constraint on n_{e0}. The second term on the left-hand-side is the kinetic energy of the PIC particles, which is calculated to second-order during the velocity advance [46] and is time-centered with the field energy. In many regimes, for example when there are only PIC ions, the kinetic energy of the PIC particles can be approximated as a constant.

5.5 PIC Electrons with Boltzmann Electrons

In many problems, the low energy electrons are nearly in thermal equilibrium, while the less numerous high energy electrons are not in thermal equilibrium. However, the high energy electrons are responsible for maintaining the plasma through ionization. Therefore, we propose a model where high energy electrons are modeled kinetically by PIC electrons, and low energy electrons are modeled by a truncated Maxwell-Boltzmann distribution. We use results from Section, 5.2.2, replacing the wall potential, ϕ_w, with the equivalent threshold energy, E_{th}, where $E_{th} = q\phi_w$. In Section 5.2.2 we showed that if ϕ_w is greater than three times the temperature then the difference in space charge between the truncated and full Maxwell-Boltzmann distribution is negligible. Therefore, we use the full Maxwell-Boltzmann distribution for calculating the space charge. However, the collisions are calculated with the truncated Maxwell-Boltzmann distribution because the excitation and ionization have thresholds that are above the truncation energy. Elastic scattering cross-sections are generally a decreasing function of energy, $\sigma \propto 1/\sqrt{E}$ where E is the collision energy in the center of mass (Lieberman and Lichtenberg, page 62 [2]) so it may not be necessary to evaluate the energy loss integral for a truncated Maxwellian directly, but to use Eq. 5.39 with only elastic scattering. For the example background gas, atomic hydrogen, the difference between elastic scattering with the cutoff used, 11.0 eV, and the full Maxwellian was negligible.

When the total energy of a PIC electron (kinetic energy plus the largest drop in potential available to that electron) drops below a fixed threshold energy, normally a little lower than the lowest inelastic energy threshold, the PIC electron is converted to a Boltzmann electron; the energy and charge of the PIC electron is added to the Boltzmann electron species energy and charge. The converted electron immediately relaxes to a Maxwell-Boltzmann distribution with its energy contribution taken into account in the temperature of the Boltzmann species.

The threshold needs to be a little lower in energy than the lowest inelastic reaction because the non-time-centered velocities are used to calculated the energy. The time-centered velocities could be used; however, since we have done the conversion of PIC electrons in the MCC subroutine, the time-centered velocities are not available. The time-centering affect the calculation of the total energy more than the calculation the of kinetic energy because the total energy calculation depends on the potential and position of the particle. The particle's position and velocity are known half a time step apart. The MCC algorithm needs the kinetic energy but it could be at any time during the time step so there is not an error in using the non-time-centered velocities. One could test the removal of the particle during the move and have a more accurate energy calculation for the conversion of PIC to Boltzmann electrons. An accurate calculation of the energy is not really necessary as long as it is below the excitation and ionization threshold. An electron that is converted, because the non-time-centered energy is less than the actual energy, that still has enough energy to have an excitation or ionization; that collision would be neglected. If PIC elec-

trons are slightly below the energy loss threshold the simulation will run slower because there are more PIC electrons than there really need to be, but the physics of the simulation are intact. Using the non-time-centered velocities under-calculates the total energy when the particle in moving into a region of higher potential energy. See Appendix F for an estimate of the error.

The conversion of Boltzmann electrons to PIC electrons is not done in this paper because it was unnecessary for the problems simulated here. The energy flow was from high energy electrons undergoing energy loss collisions and then being collected by the wall. The conversion of a Boltzmann electrons to a PIC electrons could be approximated by the Fokker-Plank equation (Krall and Trivelpiece pp 295-300 [147], Nicholson pp 66-67 and Appendix B [148]). This would base the transfer of Boltzmann electrons to PIC electrons on velocity diffusion through binary collisions. The validity of this approximation have been tested in simulation by Matsuda and Okuda [137].

5.6 Comparison with Full PIC Simulations

With these approximations, we have obtained remarkable agreement with full PIC simulations for a plasma that is maintained by photo-ionization and a DC discharge. A rough estimation of the time savings can be obtained by calculating the increase of the time step. If the full PIC simulation time step was limited by $\omega_p \Delta t$, where ω_p is the electron plasma frequency and Δt is the time step, then the speed-up obtained is of the order of $2\sqrt{m_i/m_e}$; the 2 is from assuming quasi-neutrality (approximately equal number of ions and electrons). If the time step is limited by collision frequency then the speed-up could be larger. This speed-up is degraded by the increased time it takes due to the field solve. In a 1d simulation the full PIC field solve takes around 5 percent of the simulation time. For the nonlinear Boltzmann field solve the time is increased by about a factor of 2. In 2d the field solve takes about 10 percent of the simulation time and again the Boltzmann field solve increased the time by about a factor of 2. Another factor hindering the speed-up is the use of MCC for the high energy PIC electrons, which vary greatly from problem to problem. For these two examples the computation time used for the PIC electrons is negligible. For each problem the speed-up is given in Tables 5.1 and 5.2.

5.6.1 Photo-Ionized Maintained Plasma

For the volume photo-ionization maintained plasma, the system is bounded by grounded walls; electrons and ions are absorbed when they strike the wall. To maintain the plasma, ion-electron pairs are generated uniformly across the system at a constant rate approximating photo-ionization by UV light. In this simulation there are no PIC electrons; the total electron energy remaining after a neutral has been ionized is below the threshold for excitation and ionization energy of hydrogen. The full Maxwell-Boltzmann distribution was used for the electrons. The ion kinetic energy was not used in the energy balance equation,

Eq. 5.42, to find the temperature. The ion kinetic energy was assumed to be constant. The initial condition for this computer experiment was with the simulation region empty. The simulation was run until it reached steady state. The parameters are summarized in Table 5.1. The electron mass is used for calculating the flux and the energy balance. A fictitious mass ration for hydrogen was used to speed-up the full PIC simulation, the ions were not sub-cycled. Time-averaged spatial profiles of density, velocity, potential, electric field, and temperature are shown comparing the Boltzmann electron model to finite mass PIC electrons in Figs. 5.5, 5.6, 5.7, 5.8, and 5.9. The agreement between the Boltzmann and PIC simulations is quite remarkable. The electron density in the full PIC model, Fig. 5.5, is slightly larger throughout most of the discharge that the hybrid model. The full PIC model potential, Fig. 5.6, is also slightly larger than the Boltzmann model potential.

		full PIC	Boltzmann
Physical Parameters	$\frac{\text{Mass of Ion}}{\text{Mass of Electron}}$	225	
	Background gas Pressure	3 mTorr	
	Ionization rate	$2.16 \times 10^{16}\ s^{-1}$	
	Kinetic Energy of created electrons	4.51 eV	
	Length	0.12 m	
	Cross Section	Hydrogen	
Plasma Characteristic at Steady State	Center Electron Temperature	1.48 eV	1.51 eV
	Center Ion Temperature	0.012 eV	0.038 eV
	Center Density	6×10^{13} m^{-3}	5.6×10^{13} m^{-3}
	mean free path	.16m	
	Debye length	1.17×10^{-3}m	1.22×10^{-3}m
	Length/λ_D	103	99
	Electron Plasma Frequency	69.7 MHz	∞
	Ion Plasma Frequency	4.6 MHz	4.5 MHz
Numerical Parameters	Number of grids in x	256	128
	Δ t	1×10^{-10} sec	15×10^{-10} sec
Speed-up	30 times		

Table 5.1: Parameters for the full PIC and Boltzmann model photo-ionized sustained system

5.6.2 DC Discharge

For the current-driven DC discharge example, the parameters are summarized in Table 5.2. Again, the electron mass is used for the flux and the energy balance. In the full PIC simulation the ions were sub-cycled by a factor of 10. The left-hand wall of the DC discharge is a secondary electron emitter with a probability of 0.2 of an electron being emitted every time a ion is collected by the surface. The secondary electrons are started out as PIC particles; as they lose energy they are converted to Boltzmann electrons. The spatial profiles in Figs. 5.10, 5.11, 5.12, 5.13, and 5.14 for a DC discharge show favorable

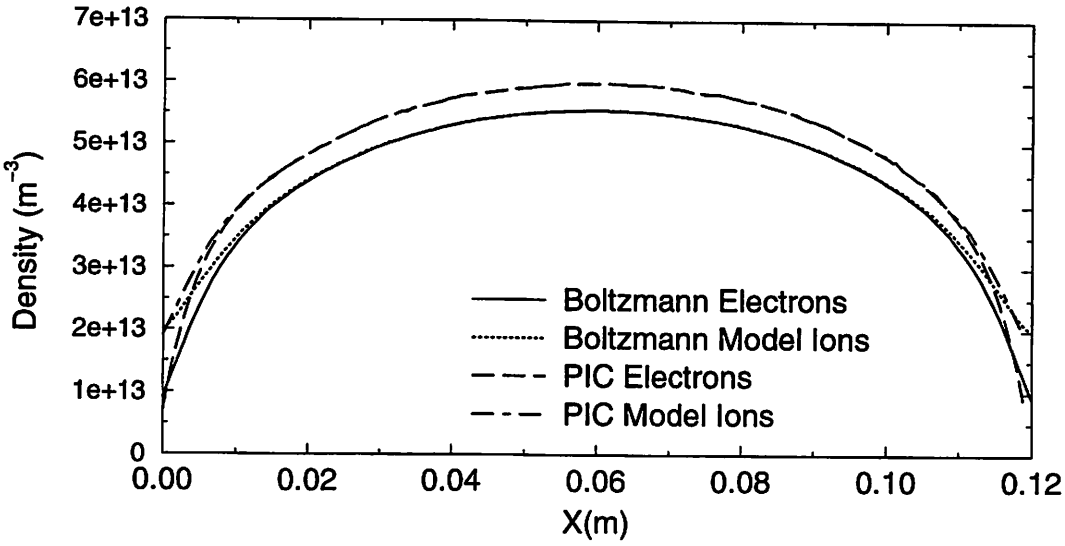

Figure 5.5: The time-averaged density from the photo-ionized sustained system comparing the full PIC simulation and Boltzmann electron model simulation.

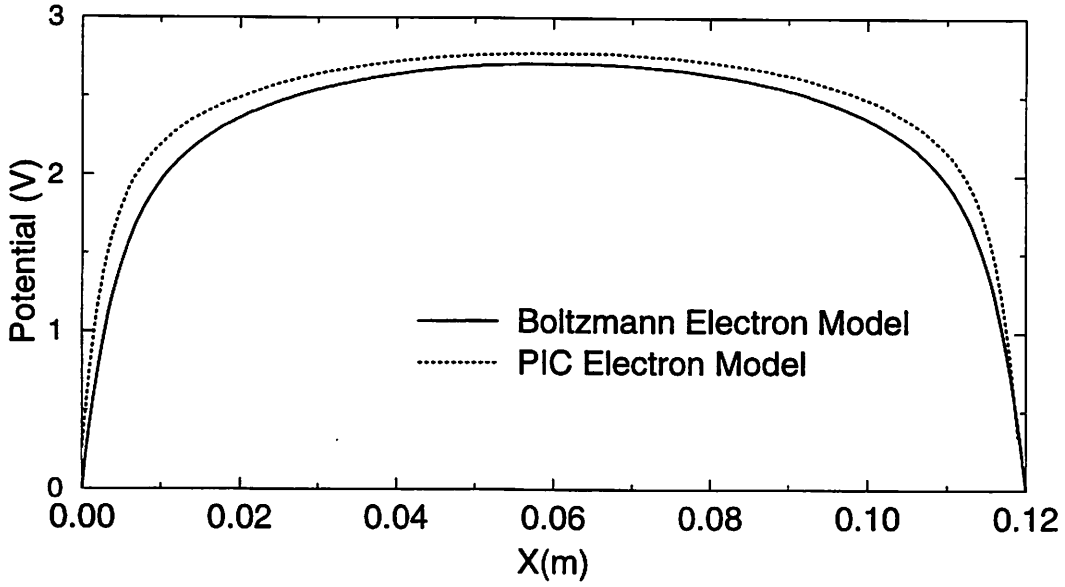

Figure 5.6: The time-averaged potential from the photo-ionized sustained system comparing the full PIC simulation and Boltzmann electron model simulation.

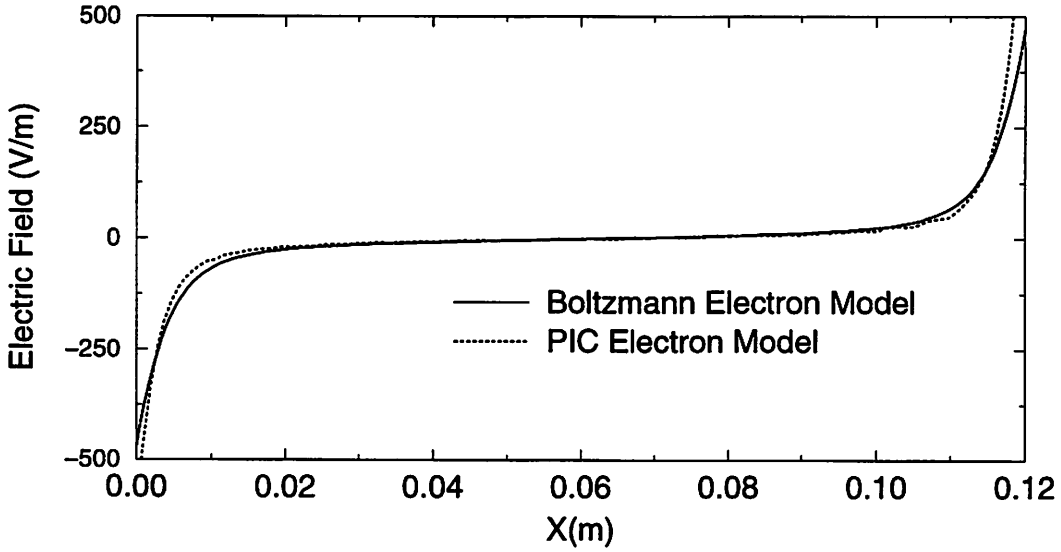

Figure 5.7: The time-averaged electric field from the photo-ionized sustained system comparing the full PIC simulation and Boltzmann electron model simulation.

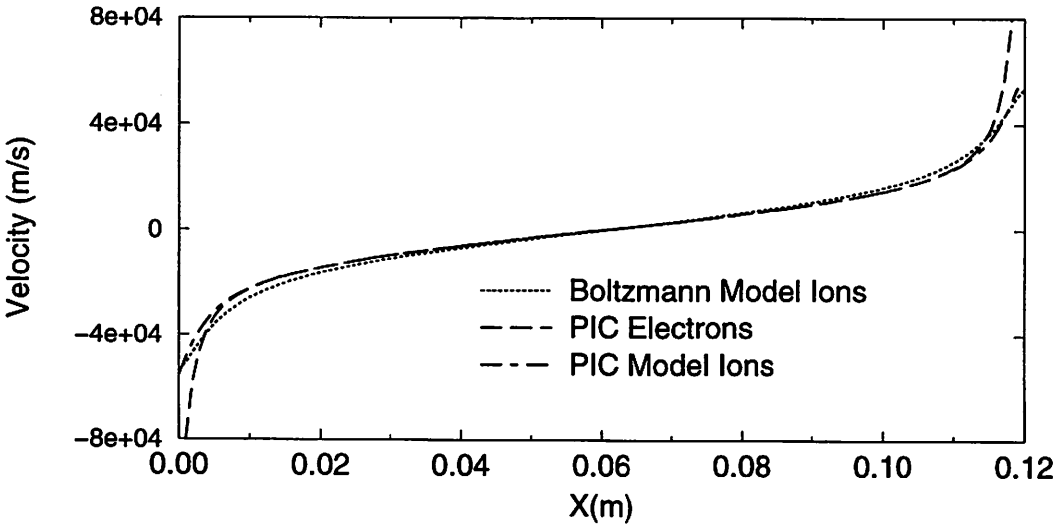

Figure 5.8: The time-averaged mean velocity from the photo-ionized sustained system comparing the full PIC simulation and Boltzmann electron model simulation (the Boltzmann electrons have zero mean velocity and are not shown).

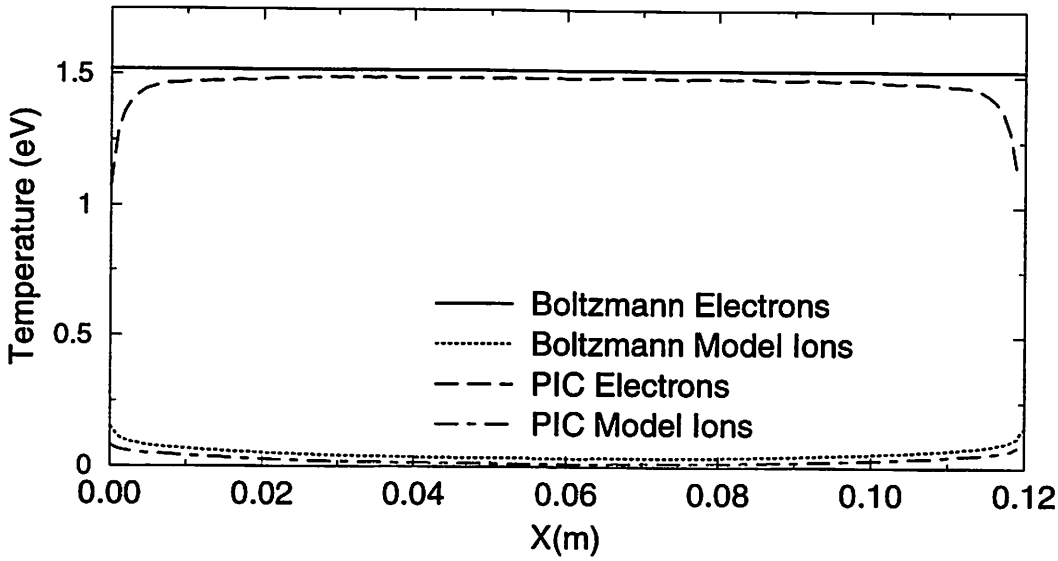

Figure 5.9: The time-averaged temperature from the photo-ionized sustained system comparing the PIC simulation and Boltzmann electron model simulation.

agreement for density, velocity, potential, electric field, and temperature. The agreement between the hybrid and full PIC simulations for the DC discharge example is not as close as in the photo-ionization case, possibly due to the spatial variation of the electron temperature (Fig. 5.14) of the full PIC simulation. The Boltzmann electron temperature is within the bounds of spatially varying PIC temperature but is also higher than the average of the PIC temperature.

5.7 Conclusions

By approximating most of the electrons with a Maxwell-Boltzmann distribution, we have obtained remarkable agreement with full PIC simulations obtaining over an order of magnitude increase in speed. The key to convergence of the nonlinear Poisson equation is to use conservation of charge for the Boltzmann species. We have used energy conservation to obtain the temperature of the Boltzmann species. In Section 5.6.1, a photo-ionized plasma is used to test the hybrid algorithm without high energy PIC electrons. Full PIC simulation agrees with the Boltzmann electron model simulation. The hybrid simulation runs 30 times faster that the full PIC simulation. In Section 5.6.2, a current-driven DC discharge is simulated. The Boltzmann electron model has a high energy kinetic electron tail added; the ionization and excitation are modeled by these electrons. Again the hybrid model agrees well with the full PIC simulation. The hybrid simulation runs 90 times faster than the full PIC simulations.

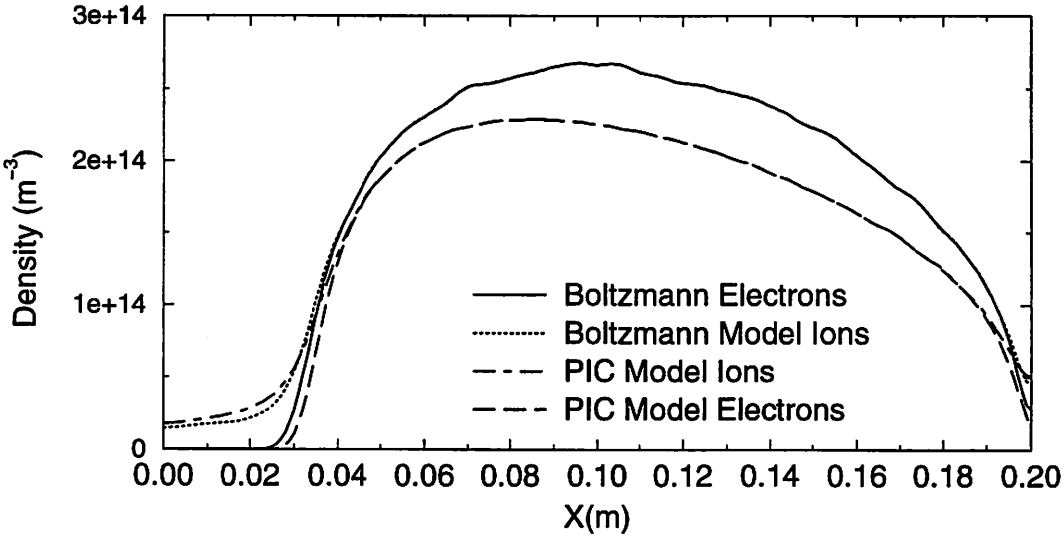

Figure 5.10: The time-averaged density from the current-driven DC discharge comparing the full PIC simulation and Boltzmann electron model simulation.

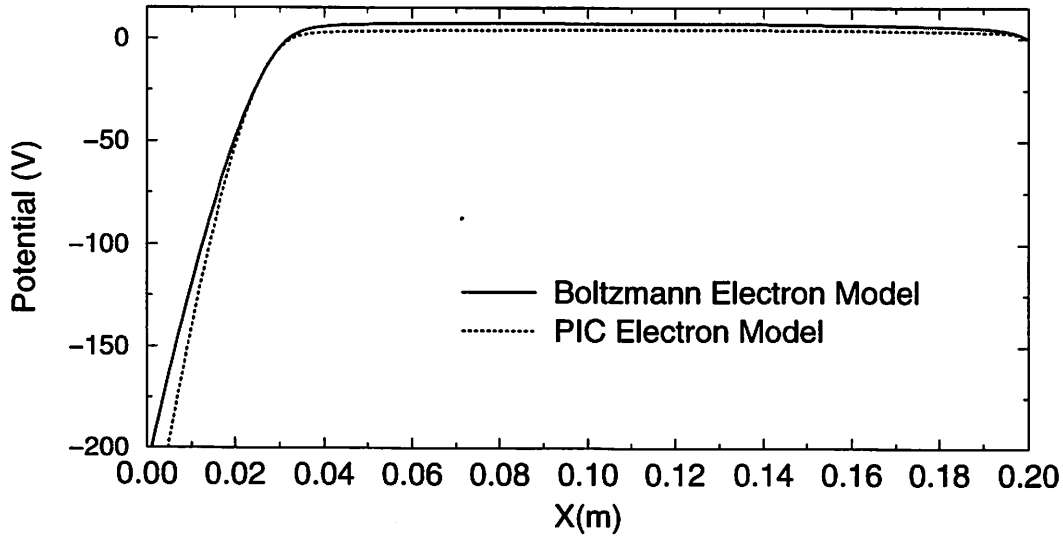

Figure 5.11: The time-averaged potential from the current-driven DC discharge comparing the full PIC simulation and Boltzmann electron model simulation.

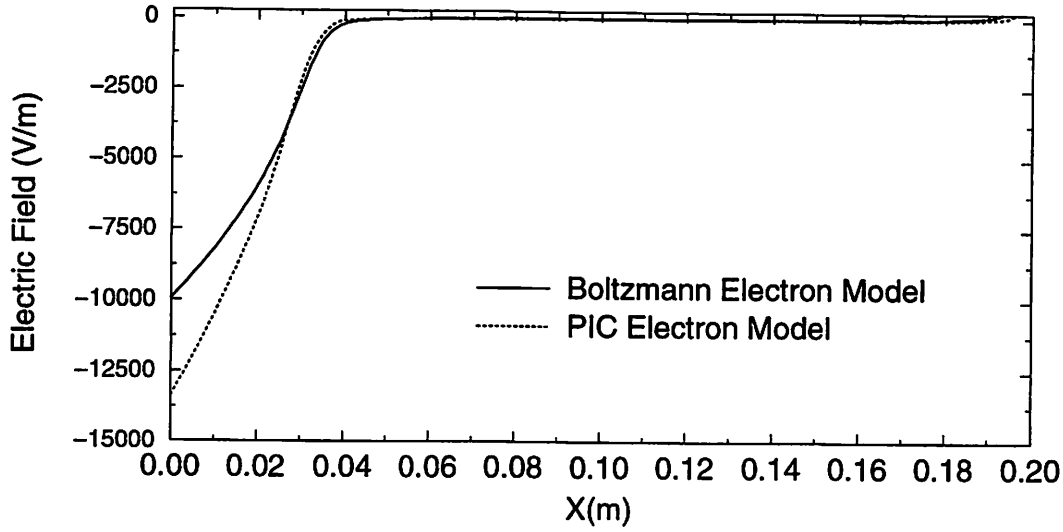

Figure 5.12: The time-averaged electric field from the current-driven DC discharge comparing the full PIC simulation and Boltzmann electron model simulation.

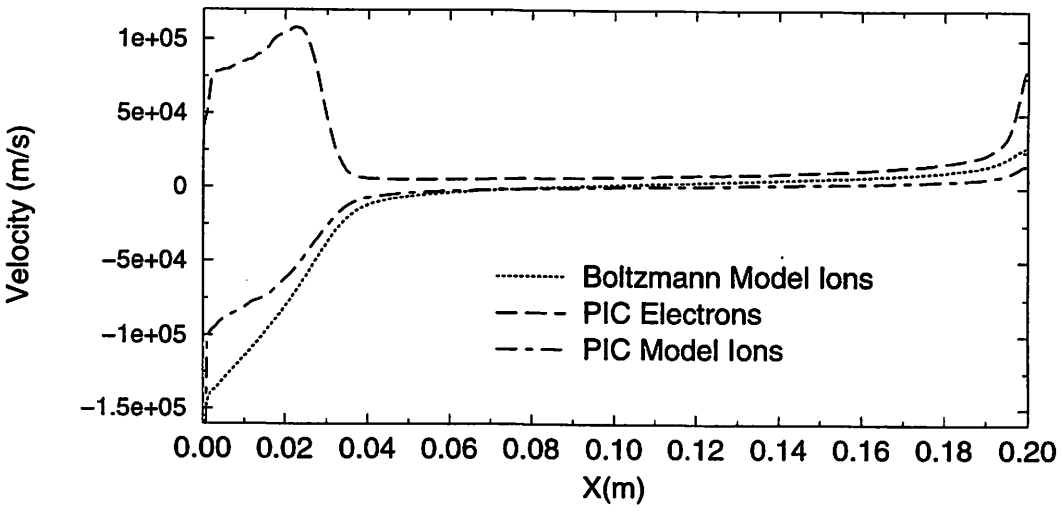

Figure 5.13: The time-averaged mean velocity from the current-driven DC discharge comparing the full PIC simulation and Boltzmann electron model simulation (the Boltzmann electrons have zero mean velocity and are not shown).

		PIC	Boltzmann
Physical Parameters	$\frac{\text{Mass of Ion}}{\text{Mass of Electron}}$	1837	
	Background gas Pressure	50 mTorr	
	Current	−0.001A	
	Length	0.2m	
	Cross Section	Hydrogen	
Plasma Characteristic at Steady State	Center Electron Temperature	2.15 eV	2.8 eV
	Center Ion Temperature	0.026 eV	0.026 eV
	Peak Density	2.28×10^{14} m^{-3}	2.66×10^{14} m^{-3}
	Debye length	7.2×10^{-4}m	7.6×10^{-4}m
	Length/λ_D	280	263
	Electron Plasma Frequency	136 MHz	∞
	Ion Plasma Frequency	3.2 MHz	3.4 MHz
Numerical Parameters	Number of grids in x	200	
	Δ t	5×10^{-11} sec	42×10^{-10} sec
Speed-up	90 times		

Table 5.2: Parameters for the full PIC and Boltzmann model simulation of the current-driven DC discharge

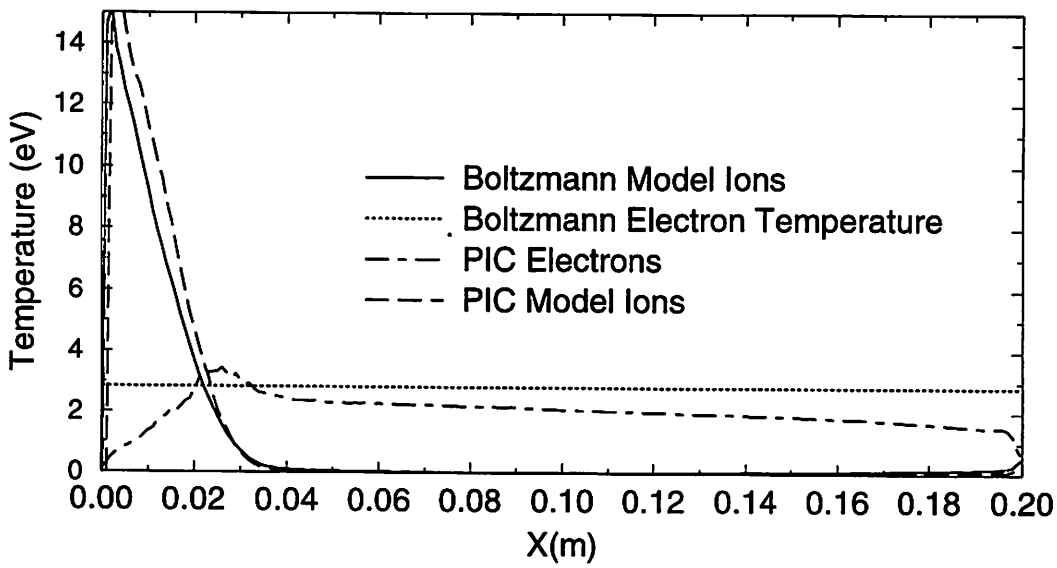

Figure 5.14: The time-averaged temperature from the current-driven DC discharge comparing the PIC simulation and Boltzmann electron model simulation.

Chapter 6

Conclusions and Future Research

6.0.1 Conclusions

We have shown theoretically and through self-consistent PIC simulation that series resonance oscillations are the dominant oscillation in insulated ($B > B_H$) 1d crossed-field diodes. This resonance is the cutoff of the 2d eigenmodes of the diocotron mode and/or magnetron mode. The virtual cathode oscillations are shown to drive the series resonance as well as noise in the Brillouin hub. The time-averaged state obtained in PIC simulation is similar to ideal Brillouin flow. The series resonance is shown to be damped by Coulomb collision which depend on the the temperature of the electron hub. The hub temperature, which is much hotter than the cathode temperature, is shown to depend mostly on the initial velocity parallel to the cathode surface perpendicular to the imposed magnetic field.

Electron transport across a magnetically insulated diode has been described in terms of a ponderomotive-like force driving the electrons across the magnetic field. This theorized mechanism predicts a transport of electrons linear in time across the magnetic field. The theory is in good qualitative agreement with the results of self-consistent 2d PIC simulation. While it is beyond the scope of the theory, the slow transport of electrons across the diode is punctuated by current spikes due to rapid loss of electrons to the anode. The current spikes have also been experimentally measured in crossed-field devices and noted in literature. Qualitative agreement between the PIC simulations reported on in this study and the experimental observations reported in literature is noted; however, a detailed comparison to experiment is beyond the scope of this thesis.

Giving attention to detail, the authors have found methods that are second-order accurate for the inversion of distributions and injections of particles. The inversion process is limited to Maxwellian distributions and fluxes, both full distributions and arbitrary cutoff at a lower and upper velocity. The second-order injection method starts for an arbitrary position and velocity at the same time and results in a position and velocity half a time step apart, With an error consistent with the standard leap-frog integrator.

A number of common cases demonstrate sensitivity to low-order injection schemes. We have shown that using a higher order method is far more effective in obtaining a more

accurate result that decreasing the time step with a lower order method. Use of these methods does not significantly increase the run time of the simulation, unless the number of particles injected is comparable to the total number of particles in the simulation.

By approximating most of the electrons with a Maxwell-Boltzmann distribution, we have obtained remarkable agreement with full PIC simulations obtaining over an order of magnitude increase in speed. The key to convergence of the nonlinear Poisson equation is to use conservation of charge for the Boltzmann species. We have used energy conservation to obtain the temperature of the Boltzmann species. In Section 5.6.1, a photo-ionized plasma is used to test the hybrid algorithm without high energy PIC electrons. Full PIC simulation agrees with the Boltzmann electron model simulation. The hybrid simulation runs 30 times faster that the full PIC simulation. In Section 5.6.2, a current-driven DC discharge is simulated. The Boltzmann electron model has a high energy kinetic electron tail added; the ionization and excitation are modeled by these electrons. Again the hybrid model agrees well with the full PIC simulation. The hybrid simulation runs 90 times faster than the full PIC simulations.

6.0.2 Suggestions for Future Research

In the area of crossed-field devices much of this work can be repeated with the addition of a secondary emitting model for both the cathode and anode surface. The secondary model would need to include the energy and angle of the incoming electron into the yield and distribution of the emitted secondary electron; for example, the one developed by Vaughan [158]. Secondary emitting cathodes are more common in CFD's than thermionic emitting cathodes. Thermionic cathodes are used in this thesis because they are simpler to treat theoretically. Secondary emitting cathodes would add to the inherent nonlinearity of the crossed-field devices because oscillations in the hub could constructively or destructively add currents to the oscillations through the creation of secondaries.

In the 2d crossed-field diode, a secondary emitting cathode could have interesting effects because we have observed that the electrons returning to the cathode are not uniform along the cathode (along y) at any given time and this non-uniformity moves along the cathode as the spokes move in the diode. Also the electron transmitted to the anode arrive with a grazing angle which may emit multiple secondaries.

The 2d crossed-field theory and simulation could also be extend by using an electromagnetic field solve to see whether there are any high frequency electromagnetic waves which couple to the electrostatic waves observed here. The theory and simulation of the transition from electrostatic waves to electromagnetic waves could be investigated, like the work done by K. Bowers for unmagnetized plasmas[159]. This theory and simulation could be extended to the relativistic regime where the self-magnetic field of the electron flow in the hub plays a role. The electromagnetic theory and simulation of the electron hub interacting with an anode circuit with a secondary emission model for the surfaces would contain all the physics of fully operational (microwave producing) crossed-field device.

The Boltzmann electron hybrid algorithm could be extended to new configurations, for example, higher density and higher neutral pressures devices where PIC becomes more computationally expensive. Possible applications could be fluorescent lamps (close to a dc discharge) or the glow regime of a plasma display panel (PDP).

This algorithm could also be used for slowly varying steady states, for example where the frequency of voltage source is low compared to the plasma frequency. This might be the case for simulating the DC bias voltage formation and ion distribution arriving at an RF voltage driven electrode in a discharge. Electrodes are generally biased negatively because more electrode surface is grounded than is driven [2]. Biasing of electrodes with this method are currently used by the semiconductor manufacturing industry to accelerate ions into the surface with the goal of obtaining a specific (for the process) energy and angle ion distribution. The ion distribution as well as the uniformity of the ion distribution across a wafer is of interest to plasma processing because the ion distribution arriving at the wafer target is crucial in determining the etch rate.

Appendix A

Pseudo-random and Sub-random Sequences

The method of choosing the random number R in the cumulative distribution function can affect the results of a simulation. A random sequence should uniformly fill in the domain at a rate of $1/\sqrt{N}$ where N is the number of points. Many physical processes will fill out a distribution function at this rate. In natural processes, N may be much larger than can be used in a simulation because of the limitations in memory and speed of the computer.

There are other ways to choose R in order to fill in the domain more quickly. If the number of particles to be used is known in advance, the R's can be distributed uniformly. There are also sub-random sequences in which the relative error decreases at least as fast as $1/N$. Obviously, if the simulation results depend upon the physical fluctuation scaling law of $1/\sqrt{N}$, this difference will affect the results. An ideal quiet start would maintain the same scaling law but reduce the proportionality constant. The scaling laws of many quiet start methods are not published; in the few published cases the scaling deviates from $1/\sqrt{N}$. Using sub-random sequences is a variation of a quiet start. Pseudo-random numbers can be replaced with a sub-random or uniform number sequence, if numerical noise suppression is desired.

Bratley and Fox [160] provide a review of (and references for) some of the more notable examples of sub-random sequences, including bit-reversed, Fibonacci, and Sobol. One note of caution about using ordered sub-random sequences is that successive numbers fill in gaps left previously in the sequences. A consequence of the sequence being ordered is that the inversion must start at the beginning. For example, numbers 1 through N will fill in the space uniformly but numbers N/2 through N will not. There are also consequences to the spectral content of the fluctuations. Pseudo-random sequences approach a uniform spectrum in Fourier space as N increases, but sub-random sequences will have a finite number of Fourier components. The choice of sequence is a fine tuning knob that the reader may adjust for the application.

Appendix B

Numerical Root Finding for Inverting Cumulative Distribution Functions

To invert the cumulative distribution function one needs to use a method to find roots of an equation numerically. The technique described here is straightforward to implement; after the initial setup there are few calculations. At initialization, a velocity array is generated using Eq. 4.7, 4.34, or 4.35. To reduce the numerical complexity and expense the velocity array has equal probability between each element, $1/bin$, with N=bin+1 elements in the array. Marsaglia and Narasimhan [161] have found uniform probability to be an efficient choice. The ith element in the velocity array is given by $v_i = F^{-1}(i/bin)$, with $v_0 = v_{cl}$ and $v_N = v_{cu}$.

Since all cumulative distributions are monotonically increasing, by adding a small velocity, δv, to the last velocity, $F(v)$ may become larger than $(i+1)/bin$. If $F(v)$ overshoots, δv is reduced by a factor of 2 and $F(v)$ is recalculated. By repeating this step, the array can quickly be filled to any accuracy needed. This method, bisection, is slower to converge than Newton's method or the secant method. The bisection method converges linearly (defining the order of convergence to be p), p=1, with a rate of $\frac{1}{2}$, while the Newton's method converges quadratically, p=2, and the secant method converges with a rate of $p = (1+\sqrt{5})/2$ [162]. Convergence is defined as:

$$\frac{v_{n+1} - v_i}{(v_n - v_i)^p} = \frac{\partial_{vv}(F(v) - i/bin)}{\partial_v(F(v) - i/bin)}\bigg|_{v=v_i} = -\frac{F''(v_i)}{2F'(v_i)} \tag{B.1}$$

where v_i is the correct answer, v_n is the previous guess, and v_{n+1} is the current guess. The advantages of the bisection method are that convergence is guaranteed, and the error bound of the root is δv, the step used at that point. Because numerical solution to obtain the velocity array is only required at initialization, guaranteed convergence and control of accuracy outweigh the improved convergence rates of the other methods.

Appendix C

Effects of discretizing distribution and fluxes

One of the consequences of inverting the distribution function with a finite number of points is that the Maxwellian has an effective upper cutoff. The maximum size of the array is determined by the desired resolution of the tail of the distribution. For example, if v_{max} is the largest velocity that can be chosen, the probability that a particle lies beyond v_{max} is $\int_{v_{max}}^{\infty} f(v)dv$ (or $\int_{v_{max}}^{\infty} vf(v)dv$ for a flux) . Increasing the number of bins used beyond where the probability of a single bin is less than the probability beyond v_{max} is ineffective because the fraction neglected is much larger that the error made due to the numerical method. The velocity index is constructed by choosing a pseudo-random number and multiplying by the number of bins. The velocity is computed by a linear interpolation between the array values indicated by the index.[1]

To calculate the number of bins needed, several different measures of the error have been used to quantify the error. The "local moment error" of the nth velocity moment is the error in each bin, which can be written as:

$$\text{LME} = \int_{v}^{v+\Delta v} v^n (f_{bin} - f_{anal}) dv, \tag{C.1}$$

where f_{bin} is the normalized distribution formed by the linear interpolation of the array and f_{anal} is the desired normalized distribution, Δv is the width of the bin and n is the velocity moment. The difference in moments integrated over the entire distribution is :

$$\text{moment error} = \sum_{bin} \int_{v}^{v+\Delta v} v^n (f_{bin} - f_{anal}) dv = \int_{v_{cl}}^{v_{cu}} v^n (f_{bin} - f_{anal}) dv. \tag{C.2}$$

The L_2 norm of the difference of the moments in one bin will also be used for a measure of

[1] Consider calculating a new pseudo-random number for interpolation because high bits in many random number algorithms are more "random" than low bits. In other words, use R_1 to choose the bin and then R_2 to interpolate between bins.

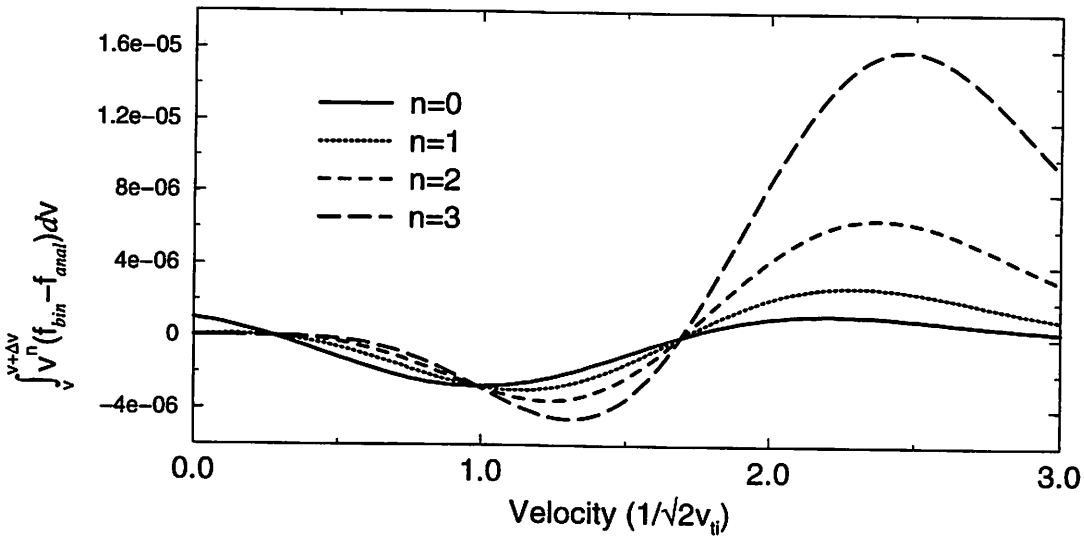

Figure C.1: The "local moment error" in each bin with 100 bins, for a Maxwellian flux with $v_0 = 1$ and $v_c = 3$ (normalized by $\sqrt{2}v_{ti}$).

the error which will be called the "local squared moment error":

$$\text{LSME} = \sqrt{\int_v^{v+\Delta v} v^{2n}(f_{bin} - f_{anal})^2 dv}. \tag{C.3}$$

The tolerance, T, is defined as the L_2 norm over the entire distribution:

$$\text{T} = \sqrt{\sum_{bin} \int_v^{v+\Delta v} v^{2n}(f_{bin} - f_{anal})^2 dv} = \sqrt{\int_{v_{cl}}^{v_{cu}} v^{2n}(f_{bin} - f_{anal})^2 dv}. \tag{C.4}$$

These measures of merit can be calculated numerically. An examples Maxwellian flux with $v_0 = 1$ and $v_c = 3$ are shown in Figs. C.1-C.4. The LME shows the integrated error in each bin, which mostly cancels out. In contrast the LSME does not have errors that cancel. The error in the moments of the distribution is plotted as a function of the number of bins used in Fig. C.3. This can be compared to the tolerance as shown in Fig. C.4. The error in the moments and the tolerance decrease as (number of bins)$^{-2}$, since the numerical inversion, both the tabulation and the interpolation, is second order accurate. Hence for a Maxwellian distribution, for which the tail does not need to be resolved, a modest number of grids can give adequate accuracy. An easily analyzed expression for accuracy has not been found but minimal requirements are not difficult to meet. For a Maxwellian flux the corresponding graphs to Figs. C.3 and C.4 would have the same slope; however, the error is slightly larger for the same moment and number of bins. A few hundred points with interpolation should handle any Maxwellian-like (continuous with finite first and second derivatives) distribution.

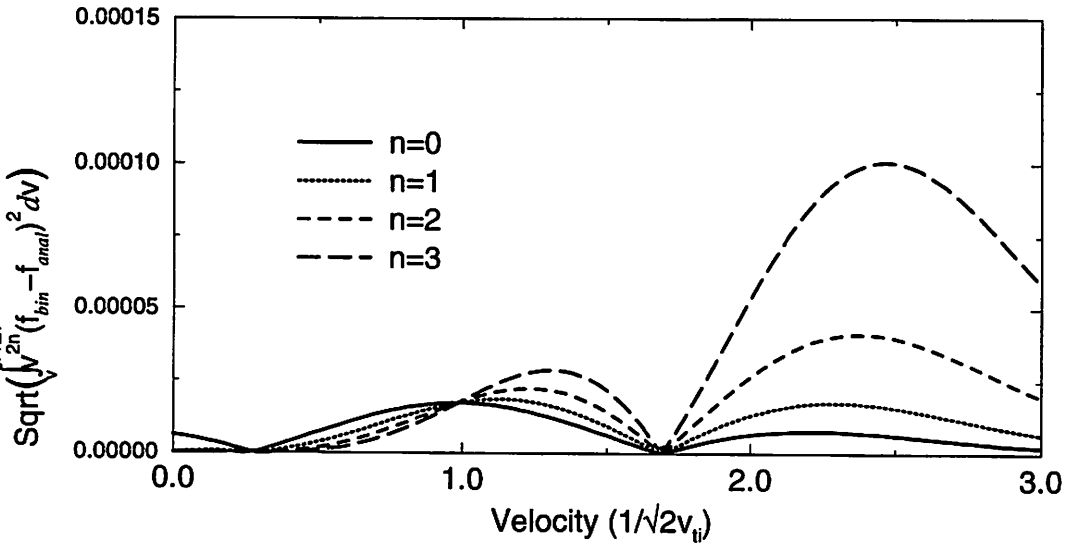

Figure C.2: The "local squared moment error" in each bin with 100 bins, for a Maxwellian flux with $v_0 = 1$ and $v_c = 3$ (normalized by $\sqrt{2}v_{ti}$).

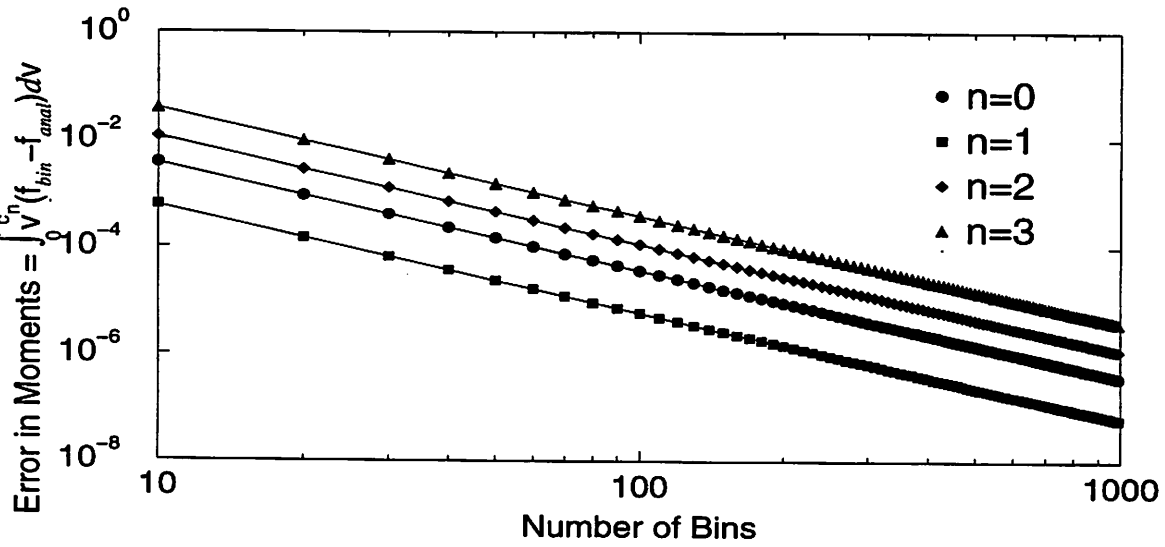

Figure C.3: The absolute error in the zeroth, first, second, third, and fourth moments as a function of the number of bins for a Maxwellian flux with, $v_0 = 1$ and $v_c = 3$ (normalized by $\sqrt{2}v_{ti}$).

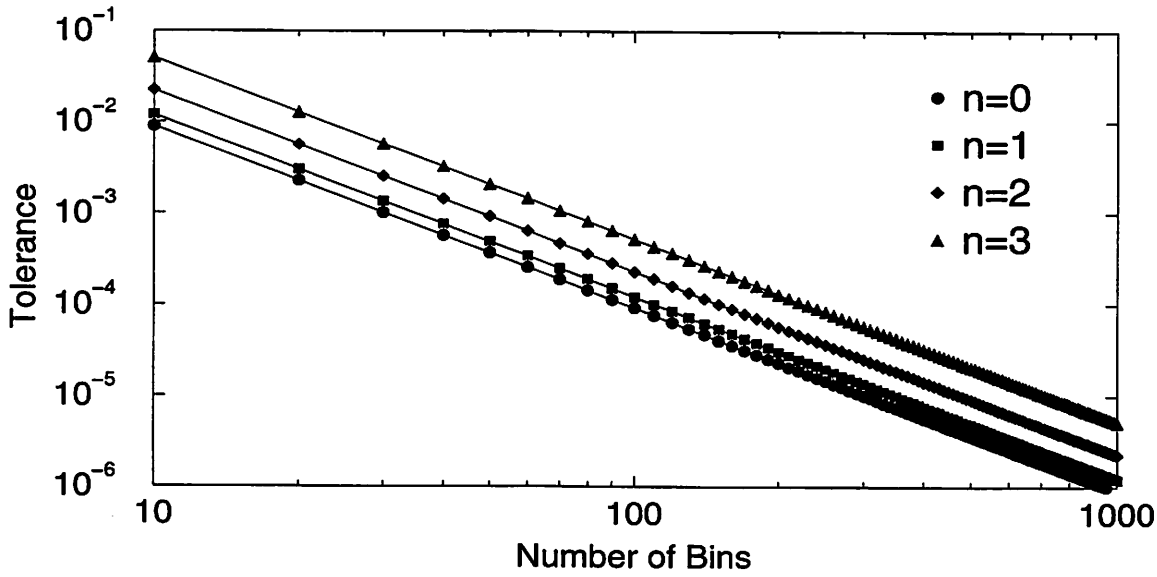

Figure C.4: The tolerance as a function of the number of bins for a Maxwellian flux with, $v_0 = 1$ and $v_c = 3$ (normalized by $\sqrt{2}v_{ti}$).

Appendix D

Truncation Error Constants

This appendix list the constants for the truncation error for the methods and cases in the body of the article, for definitions of g's see Table 4.3.

Case 1:

$$\begin{aligned} g_{11} &= (\sqrt{3+13v_{x0}^2+11v_{y0}+13v_{y0}^2})/(2n_1\sqrt{15}), \\ g_{21} &= \tfrac{1}{24}\sqrt{\tfrac{23}{14}}, \\ g_{31} &= \tfrac{1}{288n_1\sqrt{35}}\sqrt{31713+1631v_{x0}^2+12042v_{y0}+1631v_{y0}^2}, \\ g_{61} &= 1/(12n_1), \text{ and} \\ n_1 &= \sqrt{v_{x0}^2+(1+v_{y0}^2)^2}. \end{aligned} \tag{D.1}$$

Case 2:

$$\begin{aligned} g_{12} &= \sqrt{3+13v_{x0}^2+11v_{y0}+13v_{y0}^2}/(2\sqrt{15}n_2), \\ g_{22} &= \sqrt{115+8\epsilon(104\epsilon-73)v_{x0}+115(1+v_{y0})^2}/(24\sqrt{70}n_2), \\ g_{32} &= \sqrt{\tfrac{13}{70}}\tfrac{|\epsilon v_{x0}|}{3n_2}, \\ g_{42} &= (5\epsilon^2(38929v_{x0}^2+48528(1+v_{y0})^2)+9(31713+1631v_{x0}^2+v_{y0}(12042+1631v_{y0})) \\ &\quad -6\epsilon(14689v_{x0}-6(1+v_{y0})(13518+1877v_{y0})))^{1/2}/(864\sqrt{35}n_2), \\ g_{62} &= \sqrt{\epsilon^2v_{x0}^2+(1+\epsilon(1+v_{y0}))^2}/(12n_2), \text{ and} \\ n_2 &= \sqrt{v_{x0}^2+(1+v_{y0}^2)^2}. \end{aligned} \tag{D.2}$$

Case 3:

$$
\begin{aligned}
g_{13} &= \sqrt{6+3\tilde{E}^2+26v_{x0}^2+22v_{y0}+26v_{y0}}/(2n_3\sqrt{30}),\\
g_{23} &= \sqrt{((230+16\epsilon(104\epsilon-73))v_{x0}^2+230(1+v_{y0})^2+\tilde{E}^2(115+1984\omega_0^2))}/(48n_3\sqrt{35}),\\
g_{33} &= \sqrt{26\epsilon^2v_{x0}^2+31\tilde{E}^2\omega_0^2}/(6n_3\sqrt{35}),\\
g_{43} &= \sqrt{\tfrac{31}{35}}\tfrac{|\tilde{E}\omega_0|}{6},\\
g_{53} &= (10\epsilon^2(14264\tilde{E}^2+38929v_{x0}^2+48528(1+v_{y0})^2)\\
&\quad +18(31713+1631v_{x0}^2+v_{y0}(12042+1631v_{y0}))\\
&\quad +\tilde{E}^2(285417-633751\omega_0^2+1288224\omega_0^4)\\
&\quad -12\epsilon(14689v_{x0}^2-6(1+v_{y0})(13518+1877v_{y0})\\
&\quad +18\tilde{E}^2(4382\omega_0^2-2253)))^{1/2}/(864n\sqrt{70}),\\
g_{63} &= (2+\epsilon^2(\tilde{E}^2+2(v_{x0}^2+(1+v_{y0})^2))\\
&\quad +2\epsilon(2+\tilde{E}^2+2v_{y0}-\tilde{E}^2\omega_0^2)+\tilde{E}^2(1-\omega_0^2+\omega_0^4))^{1/2}/(12n\sqrt{2}),\ \text{and}\\
n_3 &= \sqrt{\tfrac{\tilde{E}^2}{2}+v_{x0}^2+(1+v_{y0}^2)^2}.
\end{aligned}
\tag{D.3}
$$

Appendix E

Iterative Method to Obtain the Second-Order Accurate Flux

The advance of the number of Boltzmann species, Eq. 5.25, and the energy advance, Eq. 5.41, is first-order in time. When the system is changing slowly in time, this error will be small; at steady state there is no truncation error. A rapidly changing system violates the physical assumption of this model, namely that the electrons are in thermal equilibrium. We make Eqs. 5.25 and 5.41 second-order by estimating the flux and temperature at the intermediate time step $n + 1/2$ and iterating to convergence. At this point in the update, we know n values and are calculating $n + 1$ values. The flux at the half time step is approximated as

$$\bar{\Gamma}_{\text{wall}}^{n+1/2} = \frac{\bar{\Gamma}_{\text{wall}}^{n} + \bar{\Gamma}_{\text{wall}}^{n+1}}{2} = \frac{\bar{\Gamma}_{\text{wall}}^{n} + \bar{\Gamma}_{\text{wall}}^{*}}{2}, \tag{E.1}$$

where $\bar{\Gamma}_{\text{wall}}^{*}$ is the current estimate for $\bar{\Gamma}_{\text{wall}}^{n+1}$. We will rewrite Eq. 5.24 in the general form $\Gamma_{\text{wall}} = -n_{e0} H(\phi(\mathbf{x}), T)$. $H(\phi(\mathbf{x}), T)$ is defined to be for the four distributions discussed previously as

$$H(\phi(\mathbf{x}), T) = \sqrt{\frac{2eT}{\pi m}} e^{-q\phi(\mathbf{x})/T} \begin{cases} \frac{1}{2}, & \text{full distribution ,} \\ \frac{e^{\frac{q\phi_w}{T}} - (1+\psi) e^{\frac{q\phi(\mathbf{x})}{T}}}{-4\sqrt{\frac{q\phi_w}{T}} + 2\sqrt{\pi} e^{\frac{q\phi_w}{T}} erf(\sqrt{\frac{q\phi_w}{T}})}, & \text{isotropic cutoff distribution ,} \\ \frac{1}{\sqrt{\pi}\left(1 + erf(\sqrt{\frac{q\phi_w}{T}})\right)}, & \text{asymmetric cutoff distribution ,} \\ \frac{1 - e^{-\psi}}{2\sqrt{\pi} erf(\sqrt{\frac{q\phi_w}{T}})}, & \text{1d symmetric distribution.} \end{cases} \tag{E.2}$$

Therefore the current estimate for the flux is $A\bar{\Gamma}_{\text{wall}}^{*} = \int_S (\Gamma_{\text{wall}}^{*} + J/eq) dS = A(J/eq - n_{e0} \bar{H}(\phi^*(\mathbf{x}), T^*))$. With the definition of N_B, Eq. 5.19, the time advance of N_B can be written as;

$$N_B^{n+1} = \frac{N_B^n + \left(\frac{\bar{\Gamma}_{\text{wall}}^n}{2} A + G\right) \Delta t}{1 + A \frac{\Delta t}{2} \frac{\bar{H}(\phi^*(\mathbf{x}), T^*)}{\int_V F(\phi^*(\mathbf{x})) d\mathbf{x}}}, \tag{E.3}$$

where the starred quantities represent the current converged approximate solution to Poisson equation for the $n+1$ time step. The second-order Boltzmann flux advance would go outside the Newton iteration loop solving Poisson's equation but inside the loop for finding the temperature.

The time advance of the energy, Eq. 5.41, can be made second-order by using the average of the temperature and flux during a time step, again iterating until the unknown temperature has converged. The time advance of the energy is

$$\Delta E_t = E_t^{n+1} - E_t^n = \Delta t \left(\left. \frac{dE}{dt} \right|_c - \frac{5}{4}(T^n + T^*) A \bar{\Gamma}_{\text{wall}}^{n+1/2} \right) - \Delta E_{PIC} \tag{E.4}$$

To obtain T^*, Eq. E.4 needs to be solved simultaneously with the energy equation, Eq. 5.42; however, the temperature and the potential energy are coupled nonlinearly through the Boltzmann relation. To obtain an updated value for the energy, the potential energy will be held fixed and the temperature used to calculate the thermal energy of the Boltzmann species will be solved for in Eq. 5.42 and substituted into Eq. E.4 to obtain

$$E_t^{n+1} = \frac{N_B E_t^n + \Delta t \left(\left. \frac{dE}{dt} \right|_c - \frac{5}{4}(N_B T^n - e \sum_{PIC} \frac{1}{2} m v^2 + \int_V \phi(\mathbf{x}) \rho(\mathbf{x}) d\mathbf{x}) A \bar{\Gamma}_{\text{wall}}^{n+1/2} \right) - \Delta E_{PIC}}{N_B + \frac{5}{2} A \Delta t \bar{\Gamma}_{\text{wall}}^{n+1/2}}. \tag{E.5}$$

Eq. E.5 is iterated to convergence outside an inner iteration loop for the flux, Eq. E.3, so that both the number and the energy of the Boltzmann species are advanced in time with a second-order method. In steady state the second-order energy and number advances are equivalent to the first-order method used in the text.

Appendix F

Error in Calculating the Total Energy of a Particle Using Non-Time-Centered Velocities

The total energy of a particle calculated with non-time-centered velocities is lower (higher) than the time-centered calculation when the particle is moving into a region of increasing (decreasing) potential energy. Under-estimating the total energy when converting PIC particles to the Boltzmann species is detrimental to this scheme because a PIC particle can undergo an energy-loss collision while the Boltzmann electrons do not.

The error in energy in using the non-time-centered velocity and position is

$$\Delta E = \frac{1}{2}m\mathbf{v}_{n+1/2}^2 + q\phi(\mathbf{x}_n) - \left(\frac{1}{2}m\mathbf{v}_{n+1/2}^2 + q\phi(\mathbf{x}_{n+1/2})\right) = q\mathbf{E}_n \cdot \mathbf{v}^* \Delta t, \tag{F.1}$$

where $\mathbf{v}^*$ is the approximate velocity at time step $n + 1/4$. This can be estimated in terms of global physical and numerical parameters. The electric field is estimated to be the temperature divided by the Debye length, λ_D, and the velocity is taken to be the thermal velocity, v_t. With these estimates the energy error is

$$\Delta E \sim T\frac{v_t \Delta t}{4\lambda_D} = T\frac{\omega_p \Delta t}{4}. \tag{F.2}$$

Generally the cell size is on the order of a Debye length (this is conservative, the cell size may be larger than the Debye length); therefore $\Delta E \sim T/4$. Making the energy threshold for conversion of PIC electrons to Boltzmann electrons $T/4$ below the lowest inelastic threshold assures that the electrons will not be converted before it really drops below the inelastic threshold.

Bibliography

[1] O. Buneman, R. H. Levy, and L. M. Linson. Stability of crossed-field electron beams. *Journal of Applied Physics*, 37(8):3203–3222, July 1966.

[2] M. A. Lieberman and A. J. Lichtenberg. *Principles of Plasma Discharges and Materials Processing.* Wiley, New York, 1994.

[3] R. H. Cohen and D. D. Ryutov. Plasma sheath in a tilted magnetic field: closing of the diamagnetic currents; effect on plasma convection. *Physics of Plasmas*, 2(1):2011–19, June 1995.

[4] B. R. Beck, J. Fajans, and J. H. Malmberg. Temperature and anisotropic-temperature relaxation measurements in cold, pure-electron plasmas. *Physics of Plasmas*, 3(4):1250–1258, April 1996.

[5] X.-P Huang, F. Anderegg, E. M. Hollmann, C. F. Driscoll, and T. M. O'Neil. Steady-state confinement of non-neutral plasmas by rotating electric field. *Physical Review Letters*, 78(5):875–8, February 1997.

[6] G. B. Collins. *Microwave Magnetron.* McGraw-Hill, New York, NY, 1948.

[7] E. Okress, editor. *Crossed-Field Microwave Devices*, volume 1 and 2. Academic Press Inc, New York, 1961.

[8] J. E. Brittain. The magnetron and the beginnings of the microwave age. *Physics Today*, page 61, July 1985.

[9] T. J. Orzechowski and G. Bekefi. Microwave emission from pulsed, relativistic e-beam diodes. i. the smooth bore magnetron. *Physics of Fluids*, 22(5):978–85, may 1979.

[10] A. Palevsky and G. Bekefi. Microwave emission from pulsed, relativistic e-beam diodes. II. the multiresonator magnetron. *Physics of Fluids*, 22(5):986–96, May 1979.

[11] J. Benford and J. Swegle. *High-Power Microwaves.* Artech House, 1992.

[12] W. C. Brown. Description and operating characteristics of the platinotron, a new microwave tube device. *IRE Proc.*, 1957.

[13] J. A. Bradshaw. *Crossed-Field Microwave Devices.* Academic Press, New York, NY, 1962.

[14] W. C. Brown. The history of the reentrant beam crossed-field amplifier with emphasis on noise comparison witht he magnetron. In D. P. Chernin and Y. Y. Lau, editors, *Proceedings of the First International Workshop on Crossed-Field Device*, page 9, Ann Arbor, MI, August 1995.

[15] M. C. Clark, B. M. Marder, and L. D. Bacon. Magnetically insulated transmission line oscillator. *Appl. Phys. Lett*, 52(1):78–80, 1988.

[16] B. M. Marder. Simulated behavior of the magnetically insulated oscillator. *Journal of Applied Physics*, 65(3):1338–1349, 1989.

[17] R. W. Lemke, S. E. Calico, and M. C. Clark. Investigation of a load-limited, magnetically insulated transmission line oscillator (MILO). *IEEE transactions on Plasma Science*, 25(2):364–374, April 1997.

[18] S. E. Calico, F. J. Agee, M. C. Clark, R. W. Lemke, and M. C. Scott. Rep-rate operation of a magnetically insulated line oscillator (MILO). In D. P. Chernin and Y. Y. Lau, editors, *Proceedings of the First International Workshop on Crossed-Field Device*, page 147, Ann Arbor, MI, August 1995.

[19] R. W. Lemke. Linear stability of relativistic space-charge flow in a magnetically insulated transmission line oscillator. *Journal of Applied Physics*, 66(3):1089–94, Aug 1989.

[20] V. L. Granatstein and I. Alexeff, editors. *High Power Microwaves.* Artech House, Norwood, MA, 1987.

[21] R. W. Lemke and M. C. Clark. Theory and simulation of high-power microwave generation in a magnetically insulated transmission line oscillator. *Journal of Applied Physics*, 62(8):3436–40, Oct 1987.

[22] T. Van Duzer. Transformation of fluctuation along accelerating cross-field beams. *IRE Trans. Electron Devices*, page 78, 1961.

[23] T. Van Duzer. High frequency behavior of the crossed-field potential minimum. *IRE Trans. Electron Devices*, page 331, 1961.

[24] T. Van Duzer. Noise-figure calculations for crossed-field forward-wave amplifier. *IRE Trans. Electron Devices*, page 370, 1963.

[25] M. A. Pollack. Noise transport in crossed-field diode. ERL Report 60, University of California, Berkeley, CA, 1962.

[26] C. K. Birdsall and W. B. Bridges. *Electron Dynamics of Diode Regions.* Academic Press, New York, 1966.

[27] R. Y. C. Ho and T. Van Duzer. Approximate formulas for crossed-field potential-minimum parameters. *IEEE Trans. Electron Devices*, (2), Feb 1968.

[28] P. J. Chrisenson. *Equilibrium, stability, and turbulence in cycloidal electron flows in crossed electric and magnetic fields.* PhD thesis, University of Michigan, Ann Arbor, MI, 1996.

[29] J. C. Slater. *Microwave Electronics.* Van Nostrand, New York, NY, 1950.

[30] S. P. Yu, G. P. Kooyer, and O. Buneman. Time-dependent computer analysis of electron-wave interaction in crossed fields. *Journal of Applied Physics*, 36:2550, 1965.

[31] P. A. Lindsay. General steady-state theory of linear magnetrons. *J. Electron. Control*, 8:177–206, 1960.

[32] P. A. Lindsay. Electron 'temperature' in crossed fields. *J. Electron. Control*, 14:273, 1963.

[33] P. A. Lindsay. General steady-state theory of linear magnetrons II. *J. Electron. Control*, 17:67–79, 1964.

[34] P. A. Lindsay and R. S. Goodell. Velocity and potential distribution in a linear, smooth anode magnetron (magnetic diode) - II. *Journal of Applied Physics*, (36):411, 1965.

[35] R. W. Gould. Space charge effects in beam-type magnetrons. *Journal of Applied Physics*, 28:599, 1957.

[36] R. L. Kyhl and H. F. Webster. Breakup of hollow cylindrical electron beams. *IRE Trans. on Electron Devices*, 1956.

[37] K. Mouthaan and C. Susskind. Statistical theory of electron transport in the smooth-bore magnetron. *Journal of Applied Physics*, 37(7):2598–2606, 1966.

[38] S. Riyopoulos. Guiding-centre orbits for particles in cross-field devices. *Journal of Plasma Physics*, 46(3):473–85, Dec 1991.

[39] S. Riyopoulos. Guiding center theory and simulations of the crossed-field amplifier. *Physics of Fluids B*, 3(12):3505–16, Dec 1991.

[40] S. A. Riyopoulos, D. P. Chernin, and A. T. Drobot. Guiding center fluid model of the crossed-field amplifier. *IEEE Trans. on Electron Devices*, 39(6):1529–42, June 1992.

[41] S. A. Riyopoulos. Feedback-induced noise in crossed field devices. *IEEE Transactions on Plasma Science*, 20(3):360–369, June 1992.

[42] A. Palevsky, G. Bekefi, and A. Drobot. Numerical simulations of oscillating magnetrons. *Journal of Applied Physics*, 52(8):4938–41, Aug 1981.

[43] G. E. Gombrowski. Simulation of magnetrons and crossed-field amplifiers. *IEEE Trans. on Electron Devices*, 35(11):2060–7, Nov 1988.

[44] D. Chernin, A. Drobot, G. Hilfer, M. Kress, and S. Riyopoulos. Computer studies of noise generation in crossed-field amplifiers. *International Electron Devices Meeting*, pages 593–6, 1991.

[45] H. L. McDowell. CFA computer modeling using a moving wavelenghth codde. In D. P. Chernin and Y. Y. Lau, editors, *Proceedings of the First International Workshop on Crossed-Field Device*, page 217, Ann Arbor, MI, August 1995.

[46] C. K. Birdsall and A. B. Langdon. *Plasma Physics via Computer Simulation.* Adam Hilger, New York, 1991.

[47] J. P. Verboncoeur, A. B. Langdon, and N. T. Gladd. An object-oriented electromanetic pic code. *Computer Physics Communicatios*, 87(1-2):199–211, May 1995.

[48] R. W. Hockney and J. W. Eastwood. *Computer Simulation Using Particles.* McGraw-Hill, New York, 1981.

[49] J. P. Verboncoeur, M. V. Alves, V. Vahedi, and C. K. Birdsall. Simultaneous potential and circuit solution for 1d bounded plasma particle simulation codes. *Journal of Computational Physics*, 104(2):321–328, Feb 1993.

[50] A. W. Hull. The effect of a uniform magnetic field on the motion of electrons between coaxial cylinder. *Phys. Rev.*, 18(1):31–57, 1921.

[51] A. F. Harvey. *High Frequency Thermionic Tubes.* John Wiley & Sons, Inc., New York, 1943. pp 83-113.

[52] R. L. Jepsen and M. W. Muller. *J. Appl. Phys.*, 22:1196, 1951.

[53] C. W. Hartman. Technical Report 60-325, Electronics Reserch Laboratory, University of California, Berkeley, 1960.

[54] R. Q. Twiss. *J. Electronics*, 1955.

[55] L. Brillouin. A theorem of Larmor and its importance for electrons in magnetic fields. *Phys. Rev*, 67(7 and 8):260–266, April 1945.

[56] A. F. Harvey. *High frequency thermionic tubes.* Chapman & Hall, London, 1942. Chap. IVa.

[57] V. S. Voronin, Zozulya, T. Yu, and A. N. Lebedev. Self-consistent stationary state of a relativistic electron beam in a drift space. *Soviet Physics - Technical Physics*, 17(3):432–40, March 1972.

[58] A. Ron, A. A. Mondelli, and N. Rostoker. Equilibria for magnetic insulation. *IEEE Trans. Plasma Science*, PS-1(4):85–92, Dec 1973.

[59] R. V. Lovelace and E. Ott. Theory of magnetic insulation. *Physics of Fluids*, 17(6):1263–8, June 1974.

[60] R. C. Davidson. Quasilinear theory of the diocotron instability for nonrelativistic non-neutral electron flow in planar geometry. *Phys. Fluids*, 28(6):1937–1947, June 1985.

[61] D. J. Kaup and G. E. Thomas. Creation of a resonant diocotron mode. *Phys. Plasmas*, 3(3):771–780, March 1996.

[62] D. J. Kaup and G. E. Thomas. Stationary operationg density profiles in a crossed-field amplifier. *J. Plasma Physics*, 59(2):259–276, 1998.

[63] M. P. Desjarlais and R. N. Sudan. Electron diffusion and leakage currents in magnetically insulated diodes. *Physics of Fluids*, 30(5):1536–52, May 1987.

[64] K. Mouthaan. Diffusion of electrons in mutually perpendicular electric and magnetic fields. *Physics of Fluids*, 8(9):1715–1719, September 1965.

[65] E. D. Hoag. Technical Report 60-239, Electronics Reserch Laboratory, University of California, Berkeley, 1959.

[66] M. I. Kuznetsov and V. A. Berbasov. A diffusion theory of the magnetron diode. *Radio Engineering and Electronic Physics*, 17(4):628–633, April 1972.

[67] G. Hok. A statistical approach to the space-charge distribution in a cut-off magnetron. *J. Appl. Phys.*, 23:983–989, 1952.

[68] R. J. Mason. Computer simulation of ion–acoustic shocks. the diaphragm problem. *Physics of Fluids*, 14(9):1943–1958, September 1971.

[69] R. J. Mason. Computer simulation of ion–acoustic shocks. II. slug and piston problems. *Physics of Fluids*, 15(5):845–853, May 1972.

[70] H. Long and C. F. F. Karney. Hybrid simulation of the sheath. *APS/DPP*, 38(10), November 1993.

[71] H. X. Vu, J. M. Wallace, and B. Bezzerides. An adiabatic fluid electron Particle-in-Cell code for simulating ion–driven parametric instabilities. *Journal of Computational Physics*, 124(2):417–30, March 1996.

[72] J. H. Whealton, E. F. Jaeger, and J. C. Whitson. Optics of ion beams of arbitrary perveance extracted from a plasma. *Journal of Computational Physics*, 27:32–41, February 1977.

[73] V. A. Thomas, W. M. Nevins, and Y. J. Chen. Simulation of the ion-beam-driven drift instability in a magnetic trap. *Physics of Fluids*, 28(7):2235–47, July 1985.

[74] V. A. Thomas, W. M. Nevins, and Y. J. Chen. Simulation of the ion-beam-driven drift instability in a magnetic trap II. *Physics of Fluids*, 28(7):2248–57, July 1985.

[75] M. E. Jones, D. S. Lemons, R. J. Mason, V. A. Thomas, and D. Winske. A grid–based Coulomb collison model for PIC codes. *Journal of Computational Physics*, 123:169–181, 1995.

[76] J. U. Brackbill and D. W. Forslund. An implicit method for electromagnetic plasma simulation in two dimensions. *Journal of Computational Physics*, 46:271–308, 1982.

[77] J. A. Byers, B. I. Cohen, W. C. Condit, and J. D. Hanson. Hybrid simulations of quasineutral phenomena in magnetized plasma. *Journal of Computational Physics*, 27:363–496, 1978.

[78] A. G. Sgro and C. W. Nielson. Hybrid model studies of ion dynamics and magnetic field diffusion during pinch implosions. *Physics of Fluids*, 19(1):126–133, January 1976.

[79] D. W. Hewett and C. W. Nielson. A multidimensional quasineutral plasma simulation model. *Journal of Computational Physics*, 29:219–236, 1978.

[80] D. S. Harned. Quasineutral hybrid simulation of macroscopic plasma phenomena. *Journal of Computational Physics*, 47:452–462, 1982.

[81] V. Vahedi and M. Surendra. A Monte Carlo collision model for the Particle-in-Cell method: applications to argon and oxygen discharges. *Computer Physics Communications*, 87:179–198, 1995.

[82] R. C. Davidson. *Physics of Nonneutral Plasmas.* Addison-Wesley, Redwood City, CA, 1990.

[83] B. P. Cluggish, J. R. Danielson, and C. F. Driscoll. Resonant particle heating of an electron plasma by oscillating sheaths. *Physical Review Letters*, 81(2):353–356, July 13 1998.

[84] D. J. Cooperberg. Electron surface waves in a plasma slab with uniform ion density. *Physics of Plasmas*, 5(4):853–862, April 1998.

[85] E. G. Linder. Effect of high energy electron random motion on the shape of the magnetron cut-off curve. *J. Appl. Phys.*, 9:331, 1938.

[86] E. G. Linder. Excess high energy electrons and electron motion in high vacuum tubes. *Proc. Inst. Radio Engrs.*, 26:346, 1938.

[87] E. A. Ash. *Electron interaction.* PhD thesis, London University, 1952.

[88] Y. Yasuoka. On the space charge affected by the magnetic field. *Journal of the Physical Society of Japan*, 10(12):1102–1109, Dec 1955.

[89] D. J. Cooperberg. *Modeling and Simulation of High Frequency Surface Waves in Bounded Plasmas.* PhD thesis, University of California, Berkeley, 1998.

[90] D. J. Cooperberg. Electron surface waves in an nonuniform plasma slab. *Physics of Plasmas*, 5(4):862–872, April 1998.

[91] D. J. Cooperberg and C. K. Birdsall. Series resonance sustained plasma in a metal bound plasma slab. *Plasma Sources Sci. Technol.*, 7(2):96–113, 1998.

[92] D. J. Cooperberg and C. K. Birdsall. Surface wave sustained plasmas in a metal bound plasma slab. *Plasma Sources Sci. Technol.*, 7(1):41–53, Feb 1998.

[93] M. Gaigneaux and P. E. Vandenplas. Temperature (Tonks-Dattner) resonances theoretically revisited: New temperature and density diagnostics. *Phys. Fluids*, 29(5):1472, 1986.

[94] L. Tonks. The high frequency behavior of a plasma. *Physical Review*, 37:1458, 1931.

[95] L. Tonks. Plasma-electron resonances, plasma resonance and plasma shape. *Physical Review*, 38:1219, 1931.

[96] N. Herlofson. *Arkiv Fysik*, 3:247, 1951.

[97] J. A. Swegle and D. S. Douglass. Electron hole oscillations below the plasma frequency in a planar gap. *IEEE Transaction of Plasma Science*, PS-14(1):67–9, February 1986.

[98] P. E. Vandenplas. *Electron waves and resonances in bounded plasmas.* Interscience Publishers, New York, 1968.

[99] J. C. Nickel, J. V. Parker, and R. W. Gould. Resonance oscillations in a hot nonuniform plasma. *Physical Review Letters*, 11(5):183, September 1963.

[100] J. V. Parker, J. C. Nickel, and R. W. Gould. Resonance oscillations in a hot nonuniform plasma. *Phys. Fluids*, 7:1489, 1964.

[101] P. Weissglass. Resonance oscillations in a hot nonuniform plasma. *Physical Review Letters*, 10(6):206, 1963.

[102] A. W. Trivelpiece and R. W. Gould. Space charge waves in cylindrical plasma columns. *J. Appl. Phys.*, 30:1784, 1959.

[103] P. J. Christenson and Y. Y. Lau. Transition to turbulence in a crossed-field gap. *Phys. Plasma*, 1(12):3725–7, December 1994.

[104] P. J. Christenson and Y. Y. Lau. One-dimensional modulational instability in a crossed-field gap. *Physical Review Letters*, 76(18):3324–3327, April 1996.

[105] P. J. Christenson, D. P. Chernin, A. L. Garner, and Y. Y. Lau. Resistive destabilization of cycloidal electron flow and universality of (near-) Brillouin flow in a crossed-field gap. *Phys. Plasmas*, 3(12):4455–4462, December 1996.

[106] A. L. Garner, Y. Y. Lau, and D. P. Chernin. Collapse of cycloidal electron flows induced by misalignments in a magnetically insulated diode. *Phys. Plasmas*, 5(6):2447–2453, June 1998.

[107] K. L. Cartwright, J. P. Verboncoeur, and C. K. Birdsall. Injection and Loading of Maxwellian Distributions in Particle Simulations. Technical report, University of California-Electronics Research Laboratory, Berkeley, CA, April 1999.

[108] J. R. Whinnery. High-frequency effects of the potential minimum on noise. *IRE Transactions on Electron Devices*, 7(4):218–230, October 1960.

[109] D. A. Ratkowsky. *Nonlinear Regression Modeling, A Unified Practical Approach.* Marcel Dekker, New York, 1983.

[110] D. H. E. Dubin and T. M. O'Neil. Two-dimensional bounce-averaged collisional particle transport in a single species non-neutral plasma. *Physics of Plasmas*, 5(5):1305–14, May 1998.

[111] C. C. MacFarlane and H. G. Hay. Wave propagation in a slipping stream of electrons; small-amplitude theory. *Proc. Phys. Soc. (London)*, 63B:409, 1950.

[112] R .H. Levy. Diocotron instability in cylindrical plasma. *Phys. Fluids*, 8:1288, 1965.

[113] D. Chernin and Y. Y. Lau. Stability of laminar electron layers. *Phys. Fluids*, 27(9):2319–2331, Sept 1984.

[114] J. Swegle and E. Ott. Linear waves and instabilities on magnetically insulated gaps. *Phys. Fluids*, 23(10):1821–1835, Oct 1981.

[115] J. Swegle. Stability of relativistic laminar flow equilibria for electrons drifting in crossed fields. *Phys. Fluids*, 26(6):1670–1677, June 1983.

[116] Y. Maron. Local electron flow to the andoe in a magneticaly insulated diode. *Physics of Fluids*, 27(1):285–90, Jan 1984.

[117] K. L. Cartwright, P. J. Christenson, J. P. Verboncoeur, and C. K. Birdsall. Dominant characteristics of one-dimensional magnetically insulated crossed field electron flow with space-charge limited emission. *Physics of Fluids*, 1999. submitted.

[118] V. P. Gopinath, J. P. Verboncoeur, and C. K. Birdsall. Simulation of transmitted current in a cylindrical cross-field diode. In *Proc. 22nd IEEE Int. Conf. Plasma Sci.*, Madison, WI, Jun 1995.

[119] K. L. Cartwright, J. P. Verboncoeur, V. P. Gopinath, and C. K. Birdsall. Transverse asymmetry in a crossed–field diode. In *Proceedings of the First International Workshop on Crossed–Field Devices*, Ann Arbor, MI, August 1995.

[120] V. P. Gopinath, J. P. Verboncoeur, and C. K. Birdsall. Similarity of stability characteristics of planar and coaxial crossed-field diodes. *Phys. Plasma*, 3(7):2766–9, July 1996.

[121] J. P. Verboncoeur and C. K. Birdsall. Rapid current transition in a crossed-field diode. *Phys Plasma*, 3(3):712–713, July 1996.

[122] J. P. Verboncoeur, P. J. Christenson, and H. B. Smith. Simulation of noise in a traveling wave tube. In *Bulletin of the American Physical Society*, volume 44, page 254, Seattle, WA, November 1999. Division of Plasma Physics.

[123] K. L. Cartwright, P. J. Christenson, J. P. Verboncoeur, and C. K. Birdsall. Virtual cathode oscillations in space-charge limited electron flow. In *International Conference On Crossed Field Devices and Applications*, Boston, MA, June 17-19 1998.

[124] K. L. Cartwright, P. J. Christenson, J. P. Verboncoeur, and C. K. Birdsall. Effects of voltage fluctuations at the cathode on Brillouin flow. In *International Conference On Crossed Field Devices and Applications*, Boston, MA, June 17-19 1998.

[125] V. P. Gopinath, J. P. Verboncoeur, and C. K. Birdsall. Multipactor electron discharge physics using an improved secondary emission model. *Physics of Plasmas*, 5(5):1535–40, May 1998.

[126] Y. Y. Lau, P. J. Christenson, and D. Chernin. Limiting current in a crossed–field gap. *Phys. Fluids B*, 5(12):4486–9, December 1993.

[127] J. A. Byers and M. Grewal. Perpendicularly propagating plasma cyclotron instabilities simulated with a one-dimensional computer model. *Phys. Fluids*, 13:1819–1830, July 1970.

[128] J. Denavit and W. L. Kruer. How to get started in particle simulation. *Comments Plasma Phys Control Fusion*, 6:35–44, April 1980.

[129] R. L. Morse and C. W. Nielson. Numerical simulation of the Weibel instability in one and two dimensions. *Phys. Fluids*, 14:830–840, April 1971.

[130] S. J. Gitomer. Comments on numerical simulation of the Weibel instability in one and two dimensions. *Phys. Fluids*, 14:1591–1592, July 1971.

[131] J. Denavit. Numerical simulation of plasmas with periodic smoothing in phase space. *Journal of Computational Physics*, 9:75–98, February 1972.

[132] S. J. Gitomer and J. C. Adam. Multibeam instability in a Maxwellian simulation plasma. *Phys Fluids*, 19:719–722, May 1976.

[133] J. M. Dawson. Plasma oscillations of a large number of electron beams,. *Phys. Rev*, 118:381–389, April 1960.

[134] W. S. Lawson and P. C. Gray. Heat flow between species in one–dimensional particles plasma simulations. *Journal of Computational Physics*, 95(1):195–211, July 1991.

[135] W. S. Lawson. Artificial cooling due to quiet injection in bounded plasma particle simulations. *Journal of Computational Physics*, 77(2):330–339, August 1988.

[136] J. Denavit. Discrete particle effects in whistler simulation. *Journal of Computational Physics*, 15:449–475, August 1974.

[137] Y. Matsuda and H. Okuda. Collisions in multi-dimensional plasma simulations. *Phys. Fluids*, 18:1740–1747, December 1975.

[138] J. M. Hammersley and D. C. Handscomb. *Monte Carlo Methods.* Methuen, London, 1964.

[139] J. H. Smith. *Introduction to Special Relativity.* Stipes Publishing Company, Champaign, IL, 1965.

[140] W. S. Lawson. Particle simulation of bounded 1d plasma systems. *Journal of Computational Physics*, 80(2):253–76, Feb 1989.

[141] L. A. Schwager and C. K. Birdsall. Collector and source sheaths of a finite ion temperature plasma. *Physics of Fluids B (Plasma Physics)*, 2(5):1057–68, May 1990.

[142] V. Vahedi, C. K. Birdsall, M. A. Lieberman, G. DiPeso, and T. D. Rognlien. Verification of frequency scaling laws for capacitive radio-frequency discharges using two-dimensional simulations. *Physics of Fluids B (Plasma Physics)*, 5(7,2):2719–29, Nov 1993.

[143] V. Vahedi and G. DiPeso. Simultaneous potential and circuit solution for two-dimensional bounded plasma simulation codes. *Journal of Computational Physics*, 131(1):149–163, Feb 1997.

[144] G. A. Emmert, R. M. Wieland, A. T. Mense, and J. N. Davidson. Electric sheath and presheath in a collisionless, finite ion temperature plasma. *Phys. Fluids*, 23(4):803–812, April 1980.

[145] F. F. Chen. *Introduction to Plasma Physics and Controlled Fusion.* Plenum Press, New York, 1984.

[146] H. E. Holt and R. E. Hakell. *Plamsa Dynamics.* Macmillan, New York, 1965.

[147] N. A. Krall and A. W. Trivelpiece. *Principles of Plasma Physics.* San Francisco Press, Inc, Box 6800, San Francisco, CA 94101-6800, 1986.

[148] D. R. Nicholson. *Introduction to Plasma Theory.* Krieger Publishing Company, 1992.

[149] I. Langmuir. Scattering of electrons in ionized gases. *Phys. Rev.*, 26:585–613, 1925.

[150] D. Gabor, E. .A. Ash, and D. Dracott. Langmuir's paradox. *Nature*, 176(4489):916–919, November 1955.

[151] P. A. Vitello, R. A. Stewart, D. B. Graves, E. F. Jaeger, and L. A. Berry. *INDUCT94: A Two-Dimensional Fluid Model of High Denstiy Inductively Coupled Plasma Sources.* Lawrence Livermore National Laboratory and Department of Chemical Engineering, UCB and Oak Ridge National Laboratory, 1995. UCRL-MA120465.

[152] W. H. Press, B. P. Flannery, S. A. Teukolsky, and W. T. Vetterling. *Numerical Recipes in C: the Art of Scientific Computing.* Press Syndicate of the University of Cambridge, New York, 1988.

[153] R. L. Devaney. *An Introduction to Chaotic Dynamical Systems.* Addison-Wesley Publishing Company, Inc, 1989.

[154] J. W. Demmel. *Applied Numerical Linear Algebra.* SIAM, Philadelphia, 1997.

[155] D. W. Hewett, D. J. Larson, and S. K. Doss. Solution of simultaneous partial differential equations using dynamic ADI:solution of the streamlined darwin field equations. *Journal of Computational Physics*, 101:11–24, 1992.

[156] William L. Briggs. *A Multigrid Tutorial.* Society for Industrial and Applied Mathematics, Philadelphia, 1987.

[157] J. P. Verboncoeur, A. B. Langdon, and N. T. Gladd. An object-oriented electromagnetic PIC code. *Computer Physics Communications*, 87(1-2):199–211, May 1995.

[158] J. R. M. Vaughan. A new formula for secondary emission yield. *IEEE Trans. Electron Devices*, 36(9):1963–7, Sept 1989.

[159] K. J. Bowers. Electromagnetic electron surface waves in a non-uniform thermal plasma. Master's thesis, University of California, Berkeley, December 1998.

[160] P. Bratley and B. L. Fox. Implementing Sobol's quasirandom sequence generator. *ACM Transactions on Mathematical Software*, 14(1):88–100, March 1988.

[161] G. Marsaglia and B. Narasimhan. Simulating interpolation search. *Computers and Mathematics with Applications*, 26(8):31–42, Oct 1993.

[162] K .E. Atkinson. *An Introduction to Numerical Analysis.* Wiley, New York, 2 edition, 1988.